UNIVERSITÄT
LEIPZIG

REPORT
Halbleiterphysik
Semiconductor Physics
2021

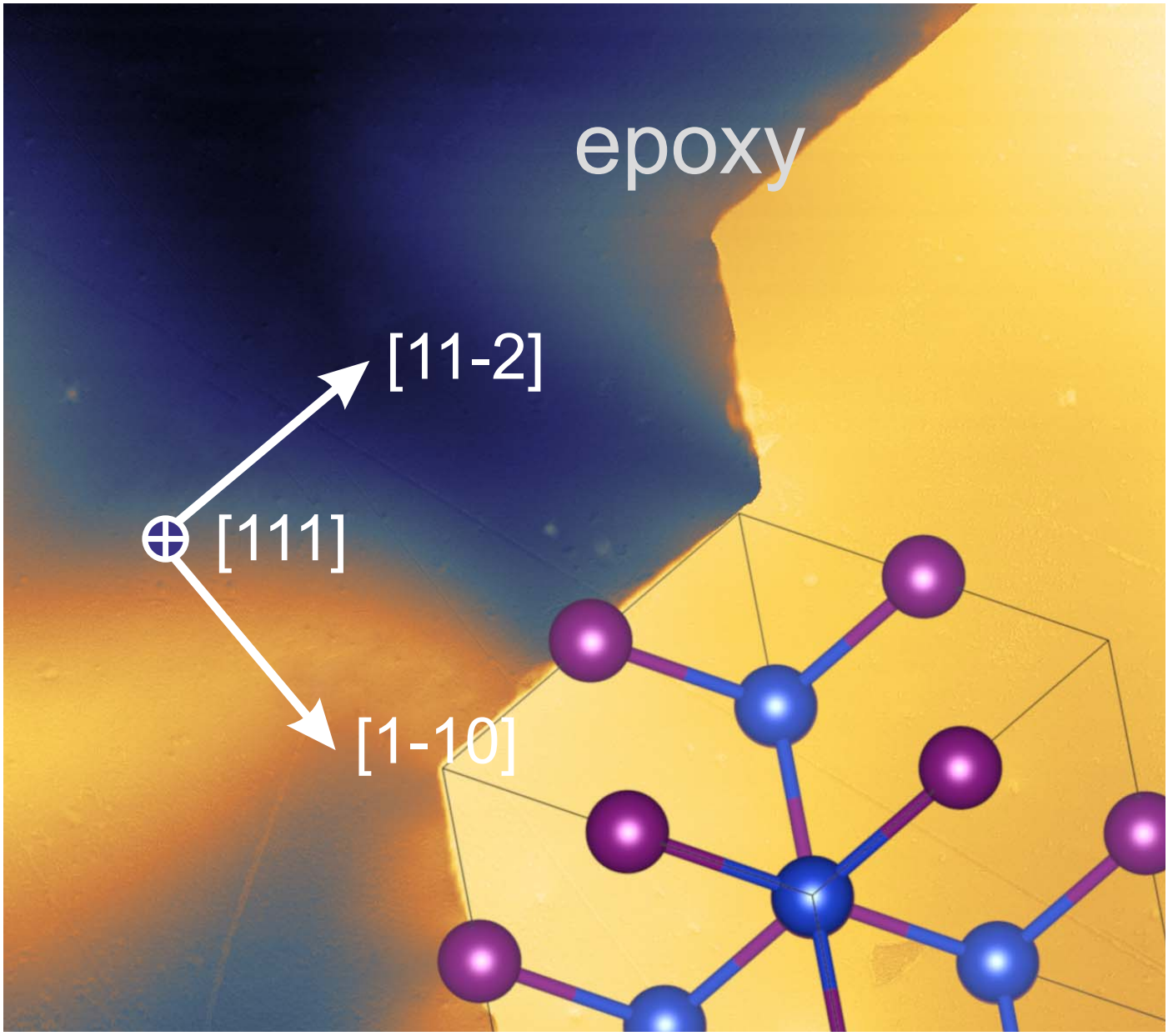

The Semiconductor Physics Group of Universität Leipzig, Report 2021
M. Grundmann (Ed.)

Technical Editor: Anja Heck

online available at
http://research.uni-leipzig.de/hlp/

Front cover
Laser scanning microscopy image in top view of the edge of a free standing 2 μm thick CuI film (on NaBr buffer on SrF_2) glued to glass with epoxy resin and a representation of the (111) out-of-plane oriented unit cell of copper iodide.

Back cover
Three-fold symmetry of Young's modulus of rhombohedral (corundum structure) α-Ga_2O_3 and some popular substrate cuts indicated by directions and labeled by the usual letters.

Abteilung Halbleiterphysik

Felix-Bloch-Institut für Festkörperphysik

Fakultät für
Physik und Geowissenschaften

Universität Leipzig

Semiconductor Physics Group

Felix Bloch Institute for Solid State Physics

Faculty of Physics and Earth Sciences

Universität Leipzig

Report 2021

Address

Semiconductor Physics Group

Linnéstraße 5
D-04103 Leipzig, Germany

Phone: +49 341 97-32650
Fax: +49 341 97-32668
WWW: http://research.uni-leipzig.de/hlp/
Mailing address: Postfach 230001, D-04081 Leipzig, Germany

Preface

Welcome to the Semiconductor Physics Group research report for the year 2021. Please browse through our results and hopefully something finds your interest. A narrow window in the pandemic allowed us to hold our meeting on "Halogen Semiconductors" in the framework of FOR 2857 in Dresden. Our Asian colleagues were patched in online at least but most participants could enjoy the benefits of a conference held in person with the associated city tour and dinner events.

Recently we had presented a general stress-strain theory for pseudomorphic layers for any crystal structure and any interface orientation. One of our predictions was that for rhombohedral (or trigonal) heterostructures epitaxy on a- and m-planes leads to different pseudomorphic strain; for hexagonal materials (e.g. wurtzite semiconductors) there is no difference for these two planes. For epitaxial thin films of α-$(Al,Ga)_2O_3$ on m-plane alumina the predicted occurrence of a shear strain up to almost 1% was quantitatively proven using X-ray diffraction, while for a-plane thin films no such shear strain is present.

Work within the DFG Research Unit FOR 2957 on copper iodide proceeded with great progress, allowing for single-phase CuI thin films from pulsed laser deposition

and lift-off and redeposition of such thin films (see cover image). Also, the detailed exciton-polariton properties of CuI were investigated on bulk crystals from the Leipzig chemistry department. In the meantime, the Research Unit has been extended for 2023-2025.

Using our new imaging ellipsometer purchased within the BMBF project UltraSPEC, waveguides with (Mg,Zn)O layers having a large lateral gradient of chemical composition could be investigated regarding their dielectric function. Device processing for our ultracompact spectrometer prototype is now possible using our new direct writing lithography.

Many exciting results jointly obtained with other colleagues and groups in Berlin have originated from the cooperation within the GraFOx ScienceCampus. We are indebted to all our funding agencies, in particular Deutsche Forschungsgemeinschaft (DFG) who also helped alleviating some of the pandemic related project delays.

Leipzig, *Marius Grundmann*
November 2022

Contents

I

Report of the Semiconductor Physics Group

1

Structure and Staff of the Semiconductor Physics Group

Prof. Dr. Marius Grundmann

Secretary

Anja Heck
Johanna Lendewig
Birgit Wendisch

Technical staff

Dipl.-Phys. Gabriele Benndorf
Monika Hahn
Dipl.-Ing. Holger Hochmuth
Axel Märcker
Dr. Daniel Splith
Dr. Lukas Trefflich

Academic staff

Dr. Max Kneiß
Prof. Dr. Michael Lorenz
Dr. Sijun Luo
PD Dr. Rainer Pickenhain (retired)
Dr. Anna Reinhardt
Prof. Dr. Bernd Rheinländer (retired)
Dr. Chris Sturm
Dr. Sophie Vogt
Dr. Holger von Wenckstern
Dr. Vitaly Zviagin

PhD candidates

Michael Bar, M.Sc.
Richard Busch, M.Sc. (Fraunhofer IMWS, Halle)
Christiane Dethloff, M.Sc.
Fangjuan Geng, M.Sc. (guest, CSC)
Anna Hassa, M.Sc.
Sebastian Henn, M.Sc.
Ron Hildebrandt, M.Sc.
Tanja Jawinski, M.Sc.
Arne Jörns, M.Sc.
Stefan Kammer, M.Sc. (First Sensor AG, Berlin)
Evgeny Krüger, M.Sc.
Oliver Lahr, M.Sc.
Andreas Müller, M.Sc.
Clemens Petersen, M.Sc.
Fabian Schöppach, M.Sc.
Philipp Storm, M.Sc.
Tillmann Stralka, M.Sc.
Laurenz Thyen
Antonia Welk, M.Sc.
Jingjing Yu, M.Sc. (guest, CSC)

Students

Jorrit Bredow
Sebastian Bürger
Zichao Cai
Felix-Florian Delatowski
Jonas Elz Philipp Firme
Riccarda Freund
Praveen Giri
Khanim Karimova
Bastian Klaus
Sandra Montag
Jasper Petschat (GLOBALFOUNDRIES, Dresden)
Caspar Pirker
Max Steudel
Anja Tiede
Christopher Walter
Lee Wen Wu
Max Zeman

2

Reports

2.1 Mechanical flexibility of amorphous zinc tin oxide based devices

O. Lahr, M. Steudel, H. von Wenckstern, M. Grundmann

Within the last decade, amorphous oxide semiconductors (AOSs) such as the now commonly deployed indium gallium zinc oxide (IGZO) became commercially available in, for instance, novel active-matrix thin-film transistor backplanes as part of next-generation flat-panel display technology [1]. The combination of the given low-temperature processability with its ionic bond configuration also makes AOS a suitable class of materials for applications in mechanically flexible electronics. Regarding a more sustainable approach to state-of-the-art IGZO based technology, amorphous zinc tin oxide (ZTO) has proven to be a promising indium-free and gallium-free alternative due to the possibility of large-scale fabrication at room temperature along with its high charge-carrier mobility of about $10\,\mathrm{cm^2V^{-1}s^{-1}}$. Previously demonstrated ZTO based transistors and integrated circuits exhibit outstanding properties when it comes to low-voltage operation combined with highly effective performance and cost-efficient fabrication procedures [2–4]. Since the vast majority of ZTO reports covers only devices investigated on rigid substrates, we present amorphous ZTO thin films as well as ZTO/PtO_x metal-semiconductor field-effect transistors (MESFETs) deposited on 50 μm thick polyimide substrates at room temperature.

Atomic-force microscopic force-distant spectroscopic measurements of ZTO in dependence on applied tensile strain in terms of bending around certain radii R, ranging from 5 mm down to 2 mm, provide insights into the elastic properties and durability of ZTO thin films [5]. The minimum bending-induced strain $\varepsilon = (z - z_{\mathrm{neutral}})R^{-1}$ has been calculated by estimating the location of the neutral plane z_{neutral} within the entire material stack of height z, where z_{neutral} takes into account the individual thicknesses of constituent layers as well as their respective approximate Young's moduli [6]. Exceeding a tensile strain of 0.83 % yields a plastic deformation of the ZTO surface, given by a distinct deviation of the mean slopes of the forces determined from the cantilever-surface interactions. Comparing the surface elasticity for $\varepsilon = 0\,\%$ after subjecting ZTO to a strain of 1.24 % with the initial measurements indicates an increased stiffness, probably attributed to residual strain and the ZTO thin film not being fully relaxed during the repeated measurement.

Associated electrical properties are investigated by Hall effect measurements in van der Pauw configuration to determine the impact of remaining residual strain on the resistivity ρ, free-carrier concentration n and charge-carrier mobility μ. $10 \times 10\,\mathrm{mm}^2$ ZTO thin films with $\rho = 2 \times 10^{-3}\ \omega\mathrm{m}$, $n = 4 \times 10^{18}\ \mathrm{cm}^{-3}$ and μ=7.2 $\mathrm{cm}^2\mathrm{V}^{-1}\mathrm{s}^{-1}$ have been subjected to bending-induced tensile as well as compressive strain up to ±2.5 %, corresponding to a radius of 1 mm. Overall, the obtained electrical properties remain unaffected by the applied strain up to ±1.24 %. Beyond 2 mm bending radius, a significant increase of the resistivity of at least 2 orders of magnitude is observable and corresponding Hall results are not clearly evaluable anymore due to alternating signs of the Hall coefficients, which is most likely associated with the ZTO thin film becoming inhomogeneous, indicated by a brittle and permanently damaged surface.

Further, ZTO/PtO_x based metal-semiconductor field-effect transistors (MESFETs) were fabricated on $10 \times 30\,\mathrm{mm}^2$ polyimide substrates using photolithography in order to investigate their performance durability under mechanical bending stress for radii ranging from 5 mm to 2 mm. During current-voltage measurements, the samples remained in a bent state for at least 10 min while tensile strain has been applied parallel to the channel. Respective transistor parameters derived from the transfer characteristics are given in Fig. 2.1. While the evaluated ensemble of MESFETs roughly maintained a reasonable current on/off ratio of 6 - 7 orders of magnitude and a subthreshold swing of about 350 mV/dec, a negative threshold voltage shift is observable, originating from an increased channel conductivity under tensile strain. After reflattening the sample, the investigated MESFETs are fully operational and the negative V_T is reversed. The samples show no visible cracks even after repeating the bending procedure for a 2 mm radius multiple times.

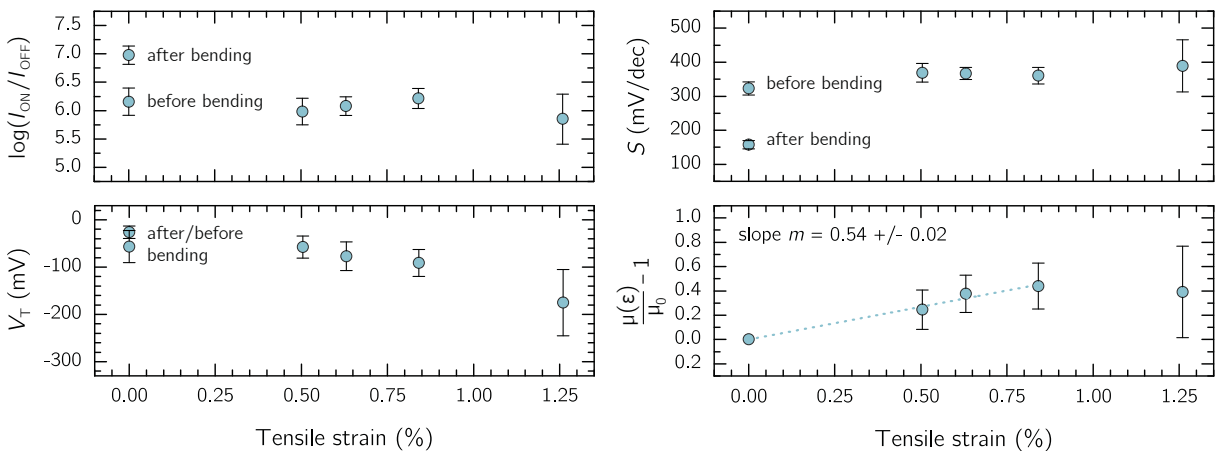

Figure 2.1: Strain-dependence of the obtained transistor parameters including the current on/off ratio, subthreshold swing, threshold voltage as well as the field-effect mobility of the investigated MESFETs for various bending radii ranging from 5 mm down to 2 mm

Associated strain-dependent normalized field-effect mobilities are calculated from the transfer characteristics using $\mu = g_{\max} L / (e n d W)$ with W and L being the gate width and length and $g_{\max}$, e and d denoting the maximum drain transconductance, the elementary charge and the channel thickness, respectively. As expected, the channel conductivity increases upon subjection the devices to higher tensile bending stress, resulting in an improved field-effect mobility from initially 4.2 $\mathrm{cm}^2\mathrm{V}^{-1}\mathrm{s}^{-1}$ ($\varepsilon = 0\,\%$) up to

7.5 $cm^2V^{-1}s^{-1}$ ($\varepsilon = 1.26\,\%$). The change of the charge-carrier mobility for moderate levels of mechanical strain can be described by $\mu(\varepsilon)\mu_0^{-1} = 1 + m\varepsilon$, where $\mu(\varepsilon)$ and μ_0 correspond to the mobility in bent and flat condition and m denotes an empirical proportionality constant [6]. In case of the presented MESFETs, m of ZTO was found to be approximately 0.53 ± 0.02 while for IGZO, values between + 1.4 and + 2.7 are reported in the literature, suggesting that the performance of ZTO based devices exhibit a less sensitive response to bending-induced strain of at least 0.84 %.

[1] H. Hosono, Nat. Electron. **1**, 7 (2003).
[2] S. Vogt, Appl. Phys. Lett. **113**, 13 (2018).
[3] P. Schlupp *et al.*, APL Mater. **8**, 6 (2020).
[4] O. Lahr *et al.*, APL Mater. **8**, 9 (2020).
[5] O. Lahr *et al.*, Front. Electron. **2**, 797308 (2021).
[6] P. Heremans *et al.*, Adv. Mater **28**, 22 (2016).

2.2 Analysis of Electrical Transport Properties of Amorphous Oxide Semiconductors by an Extended Percolation-Based Random Band-Edge Model

A. Welk, A. Reinhardt, O. Herrfurth, D. Splith, H. von Wenckstern, M. Grundmann

Amorphous oxide semiconductors (AOSs) as multi-cationic zinc tin oxide (a-ZTO) or multi-anionic zinc oxynitride (a-ZnON) with Hall mobilities up to 13 $cm^2V^{-1}s^{-1}$ [1] or 100 $cm^2V^{-1}s^{-1}$ [2, 3], respectively, have proven to be promising low-temperature deposition channel materials for metal-semiconductor field-effect [4, 5] and junction field-effect transistors [6, 7]. Further, the multinary compound ZnMgON has been deposited and characterized, showing suitable properties for TFT applications [8]. For the enhancement of device performance and thereby an optimal trade-off between electron mobility and charge carrier concentration, it is necessary to gain a profound understanding of the electrical transport mechanism. Even though the device research has made much progress during the last twenty years, the description of charge carrier transport in AOS is still under debate. Hopping transport mechanisms and trap-limited transport mechanisms have been thoroughly discussed for AOSs [9–11]. But since electron mobilities > 10 $cm^2V^{-1}s^{-1}$ are hardly achievable with these transport mechanisms [12], Kamiya and Nomura *et al.* [13] proposed a random barrier model, where charge carrier transport via delocalized states above the mobility edge is dominant. Following on from this, Nenashev *et al.* [14] developed a percolation-based random band-edge model, which takes spatial variations of the mobility edge position due to structural disorder into account.

In this work, published in Ref. [15], we examine the applicability of the random band-edge model formalism according to Nenashev *et al.* to a-ZnON, ZnMgON and a-ZTO and study the effect of cationic and anionic disorder on the mobility edge distribution. Therefore, we extend the percolation-based random band-edge model by considering not only the conductivity, but also the Hall-effect data. For this purpose we include the Hall-scattering factor in the model. This way we are able to determine the

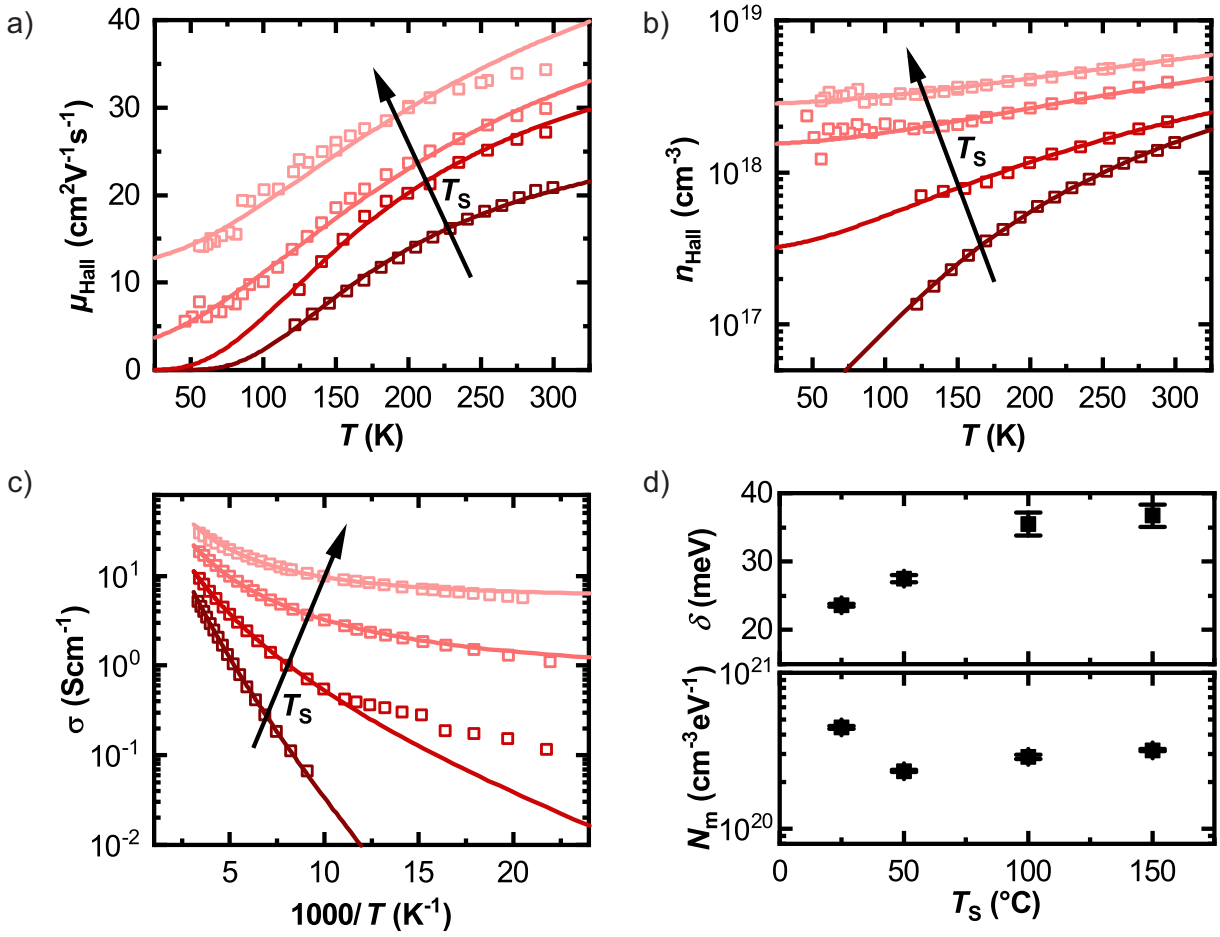

Figure 2.2: Results of modeling the temperature-dependent Hall mobility μ_{Hall} (a), Hall electron concentration n_{Hall} (b) and corresponding electrical conductivity σ according to the extended random band-edge model for a-ZnON thin films deposited at different substrate temperatures T_{S}: measured data (symbols) and fit results (solid lines). (d) Obtained band-disorder parameter δ and density of localized states at the band edge N_{m} in dependence on the substrate temperature T_{S} (published in Ref. [15])

Fermi level E_{F}, the intrinsic band-mobility μ_0, the disorder parameter δ and the density of localized tail states N_{m} being material parameters.

For a first verification of our extended model, the electrical properties of amorphous indium gallium zinc oxide (a-IGZO) thin films [16] as in the publication of Nenashev *et al.* are fitted. The mean results for $\overline{\delta} = 32$ meV are in accordance with the work of Nenashev *et al.* and the intrinsic band-mobility $\overline{\mu}_0 = 16\,\mathrm{cm^2V^{-1}s^{-1}}$ is in agreement with Fishchuk *et al.* [17] who considered the Hall-scattering factor as well. This shows the presented approach is capable to obtain reasonable material parameters.

Further, we use temperature dependent Hall-effect measurements on magnetron sputtered a-ZnON thin films with substrate temperature variation [2] and ZnMgON thin films with magnesium cation variation with concentrations between 2 at.% and 5 at.% for modeling. Besides this, we investigate PLD grown a-ZTO with an oxygen partial pressure variation between 0.003 mbar and 0.0038 mbar and a cation variation with Zn:Sn ratios of 1:2, 1:1 and 2:1. The modeled conductivity and Hall-effect data for a-ZnON are exemplarily shown in Fig. 2.2 (a)-(c) and the obtained material parameters

δ and N_m are presented in Fig. 2.2 (d).
The disorder parameter of a-ZnON increases with increasing growth temperature from 24 meV to 36 meV, which might be due to the formation of nanocrystalline phases at elevated temperatures [18, 19]. For ZnMgON thin films deposited at room temperature it is found that an increased Mg content leads to an increasing disorder parameter from 20 meV to 42 meV. This confirms quantitatively that the multi-cationic character of ZnMgON leads to stronger potential fluctuations at the mobility edge compared to multi-anionic a-ZnON. The intrinsic mobility of a-ZnON increases from 32 $cm^2V^{-1}s^{-1}$ to 60 $cm^2V^{-1}s^{-1}$ with increasing growth temperature. This means, even though the global disorder and potential fluctuations increase, the local disorder decreases since less defects are present at higher deposition temperatures. In comparison, for ZnMgON the intrinsic mobility decreases with increasing magnesium content from 27 $cm^2V^{-1}s^{-1}$ to 19 $cm^2V^{-1}s^{-1}$ due to additional scattering centers caused by crystalline magnesium oxide [8] in the amorphous matrix.

Furthermore, we showed that the inclusion of localized tail states is essential for modeling the oxinitrides. For a-ZnON we found for the density of localized tail states values in the order of $N_m \sim 10^{20}\,cm^{-3}eV^{-1}$ in agreement with Lee *et al.* [11], whereas for ZnMgON slightly higher values between $5.3 \times 10^{20}\,cm^{-3}eV^{-1}$ and $1.2 \times 10^{22}\,cm^{-3}eV^{-1}$ are determined. This difference can be explained with variations in anion composition. Since ZnMgON has a higher oxygen content than a-ZnON [8] the occurrence of additional defect states at the mobility edge is possible. In contrast to this, localized tail states can be neglected for the multi-cationic a-IGZO and a-ZTO.
For a-ZTO we found an increase in disorder with increasing tin content from 22 meV to 38 meV for Sn/(Sn + Zn) ≈ 70 at.%. This increase can be explained in accordance with the work of Siah *et al.* [20] who showed that structural disorder in a-ZTO thin films increases with increasing tin content. For the localized tail states at the mobility edge values between $(0.11 - 1.) \times 10^{20}\,cm^{-3}eV^{-1}$ are determined, which is in accordance with the work of Son *et al.* [21] and Li *et al.* [10]. Further, for a-ZTO an increasing oxygen partial pressure leads to decreasing disorder parameters from 58 meV to 27 meV. This observation can be assigned to the higher coordination number of tin atoms due to larger oxygen content and therefore smaller atomic distances. The localized tail state density decreases from $7 \times 10^{20}\,cm^{-3}eV^{-1}$ to $N_m < 1 \times 10^{19}\,cm^{-3}eV^{-1}$ with increasing oxygen partial pressure. This can be explained by a reduction of oxygen vacancies or other oxygen related defects and therefore less shallow and deep defect states [22].

In summary, we showed that the presented extended percolation-based random band-edge model is adequate for quantitative modeling of the experimentally determined temperature dependence of Hall mobility and carrier concentration of IGZO, a-ZnON, ZnMgON and a-ZTO and that the observed parameter trends in dependence on growth conditions can be interpreted with the current state of research. Therefore, the extended random band-edge model contributes to the description of charge carrier transport in AOSs materials and at the same time includes a method to quantify the potential fluctuations of the mobility edge, density of localized states and intrinsic mobility. Hence, this tool gives valuable insights in the material parameters of AOS that might be used for future experimental and theoretical work to optimize electrical properties of AOS for TFT applications.

[1] P. Schlupp *et al.*, MRS Proceedings **1633**, 101-104 (2014).

[2] A. Reinhardt *et al.*, physica status solidi (a) **213**, 1767-1773 (2016).
[3] Y. Ye *et al.*, J. Appl. Phys. **106**, 074512 (2009).
[4] S. Vogt *et al.*, Appl. Phys, Lett. **113**, 133501 (2018).
[5] A. Reinhardt *et al.*, Adv. Electron. Mater. **6**, 1901066 (2020).
[6] O. Lahr *et al.*, IEEE Trans Electron Devices **66**, 3376-3381 (2019).
[7] A. Reinhardt *et al.*, Adv. Electron. Mater. **7**, 2000883 (2021).
[8] A. Welk *et al.*, APL Mater. **9**, 021120 (2021).
[9] W. Germs *et al.*, Phys. Rev. B **86** (2012).
[10] J. Li *et al.*, Appl. Phys. Lett. **110**, 023504 (2017).
[11] S. Lee *et al.*, Scientific Reports **5** (2015).
[12] S.D. Baranovskii *et al.*, EPL (Europhysics Letters) **127**, 57004 (2019).
[13] T. Kamiya *et al.*, J. Display Technol. **5**, 462 (2009).
[14] A.V. Nenashev *et al.*, Phys. Rev. B **100** (2019).
[15] A. Welk and A. Reinhardt *et al.*, Phys. Rev. Applied **17**, 024007 (2022).
[16] A. Takagi *et al.*, Thin Solid Films **486** (2005).
[17] I.I. Fishchuk *et al.*, Phys. Rev. B **93** (2016).
[18] J. Park *et al.*, Scientific Reports **6** (2016).
[19] A. Reinhardt, Dissertation, UniversitÃ¤t Leipzig (2017).
[20] S.C. Siah *et al.*, Appl. Phys, Lett. **104**, 242113 (2014).
[21] Y. Son und R.L. Peterson, Semicond. Sci. Technol. **32**, 12LT02 (2017).
[22] M.J. Wahila *et al.*, APL Mater.**7**, 022509 (2019).

2.3 Extrinsic Doping of CuI Thin Films

P. Storm, M.S. Bar, S. Gierth*, S. Selle*, H. von Wenckstern, M. Grundmann, M. Lorenz

*Fraunhofer-Institut für Mikrostruktur von Werkstoffen und Systemen (IMWS), Halle

The growth of CuI by pulsed laser deposition within the semiconductor physics group in Leipzig has previously shown promising results to fabricate non-degenerate semiconducting thin films in conjunction with a suitable Al_2O_3 capping layer [1]. However, the requirement of an *in-situ* grown capping suggests an extrinsic influence on the defect chemistry of PLD CuI thin films and requires further investigations to obtain complete control over the electrical properties. Herein, the long-term behaviour of uncapped CuI or CuI capped with Al_2O_3 was investigated and optimized with extrinsic selenium doping of corresponding thin film layers.

Concerning the electrical properties, three regimes with very distinct behavior were identified as shown in Fig. 2.3(a). For uncapped CuI, the resistivity decreases immediately after growth and settles at the expected value for, usually degenerate, CuI. If an in situ Al_2O_3 capping, grown in an oxygen atmosphere, is deposited on top of the CuI, the electrical properties are much more stable and slowly change on a week- to month-scale toward lower resistivities. However, if the background gas during capping growth is switched from O_2 to N_2, the long-term behavior changes drastically. In this regime, the resistivity increases over up to 4 orders of magnitude on a hour- to day-scale and slowly decreases afterward. After multiple weeks, the resistivity starts to stabilize well above the value expected for degenerate CuI. We attribute this behavior to the oxygen

diffusion between CuI, Al_2O_3 capping, and the atmosphere, with oxygen acting as an acceptor in CuI. To further verify these assumptions, depth-resolved ToF-SIMS measurements were conducted as shown in Fig. 2.3(b). Traces of oxygen inside the CuI thin films were found. In particular, for the CuI, the oxygen and aluminum plasma constituents from the capping growth process exhibit very large decay lengths up to a 100 nm scale. $^{18}O_2$ isotope diffusion experiments verify this diffusion process as shown in Fig. 2.3(c). To further stabilize the electrical properties and no longer rely on diffusive oxygen to control the conductivity, selenium doping was pursued in the second part. The long-term behavior of CuI:Se was studied by time-dependent resistivity measurements as shown in Fig. 2.3(d) and revealed significantly more stable properties compared to undoped or intentionally oxygen-doped CuI for Al_2O_3 cappings grown in N_2 . As a promising oxygen barrier, Al_2O_3/SiN_yO_x superlattice cappings were investigated that prevent any notable resistivity decreases close to a month-scale and presumably even much longer. We explored the doping limits of intentional p-doping as demonstrated in Fig. 2.3(e) in a range between $p = 10^{15}$ cm^{-3} at x(Se) = 0.2 at.% to $p = 8 \times 10^{17}$ cm^{-3} at x(Se) = 1 at.%. Further increases in x(Se) result in decreasing carrier densities. Concerning the crystallinity of corresponding thin films, unidentified XRD reflections close to the γ-CuI reflection appeared and successively replaced the γ-CuI reflection if the selenium content was increased to x(Se) = 1 at.% as shown in Fig. 2.3(f), in agreement with the electrically determined doping limits.

In conclusion, the impact of Al_2O_3 cappings on the long-term behaviour of the electrical resistivity was investigated in the first part. The results show that the unintentional incorporation of oxygen into CuI is the main cause for the p-conductivity of PLD grown thin films. This was further confirmed by oxygen isotope experiments and ToF-SIMS depth profiling. A temporal stabilization of the electrical properties was obtained with selenium doping and the doping limits were determined. For the transition into the CuISe alloy system, phase separation was observed. For a more detailed descirption please refer to [2, 3]. The work was founded within the research unit FOR 2857 through projects P01 and P05.

[1] P. Storm *et al.*, APL Materials **8**, 091115 (2020)
[2] P. Storm *et al.*, APL Materials **9** 051101 (2021)
[3] P. Storm *et al.*, PSS (RRL) **15** (8), 2100214 (2021)

2.4 Single Crystalline CuI and Epitaxial Lift-Off enabled by Sodium Bromide Buffer Layers

P. Storm, K. Karimova, M.S. Bar, S. Selle*, H. von Wenckstern, M. Grundmann, M. Lorenz

*Fraunhofer-Institut für Mikrostruktur von Werkstoffen und Systemen (IMWS)

The occurence of rotational domains is a well known issue for copper iodide (CuI) that naturally occurs for growth on popular substrates like sapphire. However, this has detrimental effects on the thin film quality like increasing surface roughness or deteriorated transport characteristics due to grain boundary scattering. Utilizing pulsed laser deposition and the *in-situ* growth of sodium bromide (NaBr) template layers,

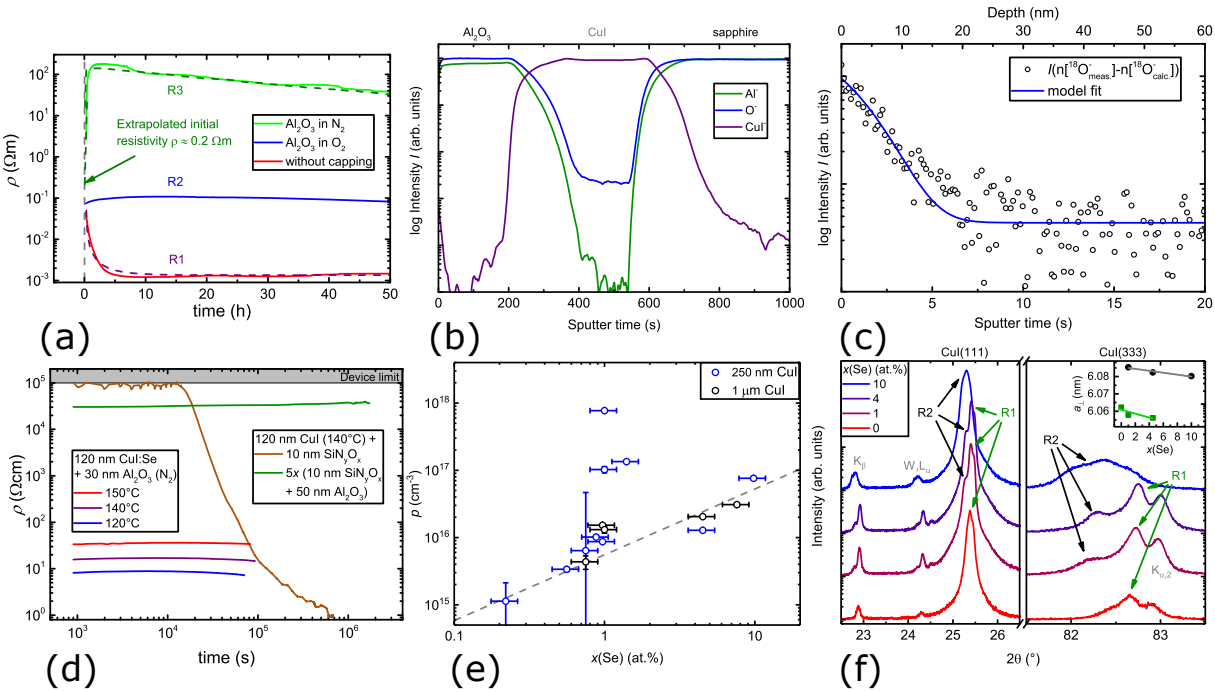

Figure 2.3: (a) Evolution of the electrical resistivity over time for 120 nm CuI thin films with an additional 30 nm Al_2O_3 thin film on top as indicated. The measurement was conducted at $T_m = 50°C$ in darkness at air. (b) Depth-resolved ToF-SIMS signal of Al^-, O^- and CuI^- of a 0.1 μm Al_2O_3 / 1 μm CuI sample on c-sapphire. (c) Depth-resolved ToF-SIMS $^{18}O_2$ diffusion profile after eight days of exposure to a $^{18}O_2$ atmosphere with the corresponding model fit. (d) Evolution of the electrical resistivity over time for 120 nm CuI:Se thin films capped with 30 nm Al_2O_3 in dependence on the indicated growth temperature T_I (blue to red) and long-term evolution of the electrical properties of CuI capped with a SiN_yO_x thin film (brown) or SiN_yO_x/Al_2O_3 superlattice (green). The resistivity measurements were conducted at $T_m = 50°C$. (e) Hole carrier density in dependence on the calculated selenium content of 250 nm (black) or 1 μm (blue) CuI:Se thin films capped with 30 nm Al_2O_3. (f) Magnified view on the CuI(111) and CuI(333) reflections with the two separate reflections designated by R1 and R2. Additional reflections caused by CuK_β, $CuK_{\alpha,2}$, and WL_α radiation are designated correspondingly. The inset shows the evolution of the calculated out-of-plane lattice constant $a_\perp$ in dependence of the selenium content x(Se) for a cubic symmetry for R1 (green) and R2 (black). All figures were adapted from [2, 3]

studies were performed on their potential on suppressing the formation of rotational domains of CuI on SrF_2(111) substrates. Corresponding samples were investigated concerning their epitaxial properties and further characterized regarding (volume) crystalline, morphological and electrical properties. Further, an epitaxial lift-off process was developed, utilizing the water-solubility of NaBr as an advantage and allowed for the creation of free-standing thin films.

XRD 2θ-ω scans of a 1 μm thick CuI film prior to separation and attached to glass or epoxy are presented in Fig. 2.4(a, top). For all investigated samples, the exclusive occurence of (nnn) reflections confirms growth in (111) out-of-plane orientation and similar to previous result of PLD grown CuI. As shown in the magnified view on the CuI(222) reflection, the $CuK_{\alpha1,\alpha,2}$ splitting is oberservable, indicating a high lattice coherency in out-of-plane direction. XRD ω-scans of these samples are also presented

in Fig. 2.4(a, bottom right). For CuI still attached to the SrF_2, lowest ω-FWHM values are obtained with $\Delta\omega = 0.5°$ and also very similar to PLD CuI on c-sapphire [1]. For free-standing thin films created with an epitaxial lift-off process, the corresponding FWHM values are not significantly increased. The single crystalline nature was verified by XRD ϕ-scan of the CuI(422) reflection of a free-standing CuI film attached to glas as shown in Fig. 2.4(a, bottom left). Only three reflections can be recognized with an angular spacing of 120°. The absence of any additional reflections and distinct cleavage along <110> as shown in Fig. 2.4(c) confirms the single crystalline growth of CuI on the NaBr buffer layer on the SrF_2 substrate. Atomic force microscopy scans of the CuI and former CuI/NaBr interface surface are shown in Fig. 2.4(e, bottom) and Fig. 2.4(e, top), respectively. The absence of rotational domains significantly reduces the surface roughness to ≈ 1 nm and step-and-terrace structures are observed for the former CuI/NaBr interface. For thin films with thickness exceeding 2 μm, rotational domains reappear and the crystalline quality of the thin film degrades. This is exemplary shown in Fig. 2.4(d) with the increasingly defected nature of the cleavage face above the critical thickness. However, to perform Hall-effect measurements, non-fractured thin films are required that were only obtained for CuI films with a thickness exceeding 10 μm due to increased mechanical stability. It was therefore not possible to obtain Hall-effect measurements for single crystalline films, but always in conjunction with domain epitaxial CuI. Similarly to uncapped CuI thin films grown by PLD, the electrical resistivity is not stable if exposed to the ambient atmosphere as shown in Fig. 2.4(b). Concerning the Hall-effect measurements, highest hole mobilities and lowest hole densities were obtained for the shortest atmospheric exposure times t_E at $\mu = (24 \pm 2)\,\mathrm{cm^2/Vs}$ and $p = (1.8 \pm 0.2) \times 10^{16}\,\mathrm{cm^{-3}}$. These values are also closest to the bulk properties with smallest impact of interface conduction and mobilities.

In conclusion, an approach to fabricate single-crystalline CuI thin films utilizing sodium bromide buffer layers was developed. Corresponding thin films possess significant improved surface morphologies and no significantly crystalline degradations were observed for the employed lift-off process. For a more detailed descirption please refer to [2, 3]. The work was founded within the research unit FOR 2857 through projects P01 and P05.

[1] P. Storm *et al.*, APL Materials **8**, 091115 (2020)
[2] P. Storm *et al.*, ACS Appl. Mater. Interfaces **14**, 12350 (2022)
[3] P. Storm *et al.*, J. Phys. Chem. C **10**, 4124 (2022)

2.5 Epitaxially grown In_2S_3 thin films on saphhire substrates

T. Jawinski, R. Clausing *, H. Kempa *, M. Grundmann, R. Scheer *, H. von Wenckstern

*Martin-Luther-Universität Halle-Wittenberg

Indium sulfide (In_2S_3) is a non-toxic III-VI *n*-type semiconductor compound and has been predicted to be a promising candidate for intermediate band solar cell (IBSC) application [1]. For an IBSC the efficiency can exceed the Shockley Queisser limit of

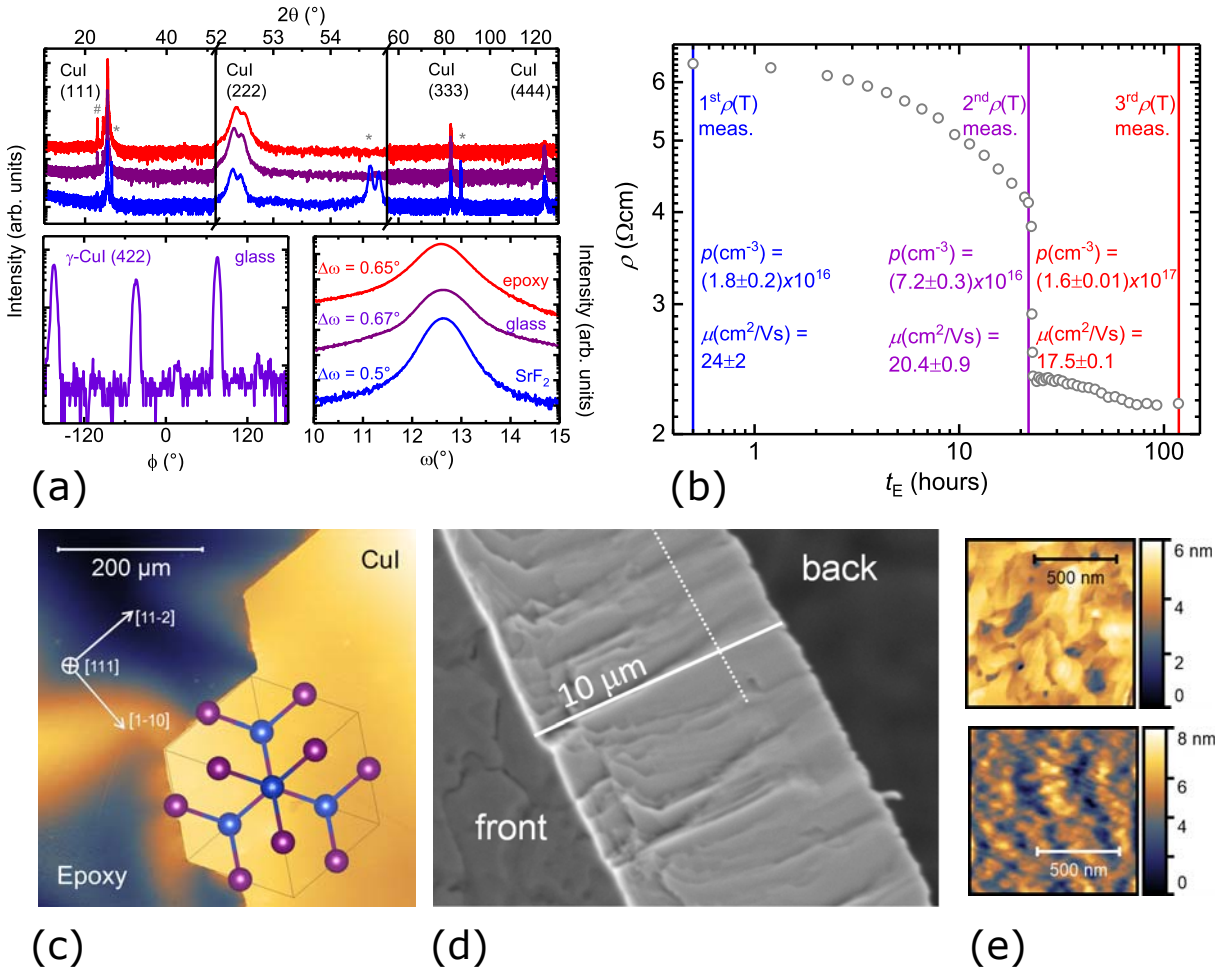

Figure 2.4: (a) XRD 2θ-ω- (top), ϕ- (bottom left) and ω-scans (bottom right) of as-grown CuI/NaBr/SrF_2 heterostructures (blue), CuI attached to glass (purple) or epoxy (red). The rhombus represents CuK_β- and the asterisk SrF_2 substrate reflections. (b) Time-dependent measurement of the electrical resistivity ρ during exposure to the atmosphere t_E of a 25 μm free-standing CuI film previously deposited on NaBr/SrF_2. The CuI was not capped by protection layers. (c) Laser scanning microscopy image in top view of the edge of a free standing 2 μm CuI film (CuI/NaBr/SrF_2) glued to glass with epoxy resin and a representation of the (111) out-of-plane oriented unit cell of copper iodide. (d) Secondary electron microscopy image of a free standing 10 μm CuI thin film of the side-view of a 110 cleavage face. The dotted line in (d) is a guide to the eye for the different defect regimes of the cleavage face. (e) AFM morphology scan of the surface of CuI attached to glass via epoxy (top) or directly on glass (bottom). All figures were adapted from [2, 3]

single junction solar cells by introducing an intermediate band (IB) between the valence and the conduction band of a photovoltaic material. Thus thermalization losses can be reduced. Furthermore sub-bandgap photons can be absorped by valence band to IB and IB to conduction band transitions [2]. In In_2S_3 the IB can be formed by hyper-doping with transition metals such as vanadium [1]. For sufficient doping concentrations an energy band with delocalized states forms and thus radiative recombination is suppressed [3]. *pin*-heterostructure devices using vanadium-doped In_2S_3 as absorber have been realized in [4]. Although they show high current rectification of up to 6 orders of

magnitude, they suffer from interface recombination.

We grew In_2S_3 thin films by physical co-evaporation of the elements. Using a cracker cell to evaporate sulphur allows us to vary the amount of offered sulphur and the fraction of reactive sulphur by varying the effusion cell and hot lip temperature, respectively. Furthermore we varied the substrate temperature. To optimize the structural properties of the thin films deposited on corning glass substrates, we varied these preparation conditions. We further deposited In_2S_3 thin films on sapphire substrates of different cuts to initiate epitaxial growth.

We investigated the surface morphology of the samples using secondary electron microscopy. The sample prepared on a glass substrate with lowest temperatures during growth exhibits a rough surface with randomly orientated irregularly shaped and partially elongated crystallites on the surface. Samples prepared at highest deposition temperatures show triangular-shaped crystallites and smoother surfaces. The largest triangular crystallites and the smoothest surfaces are found for In_2S_3 on a-sapphire substrates. The structural properties of the films were investigated using X-ray diffraction (XRD). We find a preferred (109) orientation for films deposited at lowest deposition temperatures, whereas films prepared at highest deposition temperatures exhibit a preferred (103) orientation. Films deposited on sapphire substrates exhibit a single (103) orientation. Furthermore epitaxial growth with 4 and 2 rotational domains was achieved for In_2S_3 thin films grown on a- and c-sapphire, respectively. For In_2S_3 grown on r-sapphire epitaxy can only be assumed due to low intensity. The film grown on m-sapphire does not show epitaxial growth. Absorption spectra were examplarily discussed for the sample on a-sapphire and reveal a low onset in absorption at about 1.75 eV, which can be attributed to a band gap of 2.1 eV. Furthermore, a strong increase in absorption was obseved at 2.5 eV, which can be attributed to a band-band transition at 2.7 eV. We measured the dark resistance of In_2S_3 over time after illumination with an LED light source. We find a strong persistent photoconductivity for all samples. This might be attributed to deep defects, that lead to the sub-bandgap absorption either. We prepared *pn*-structured solar cell devices by depositing *p*-type zinc-cobalt-oxide by pulsed laser deposition on *n*-type In_2S_3 thin films. Current-voltage measurements in the dark and under illumination reveal rectification of up to 4.4 orders of magnitude and photovoltaic effect, respectively.

[1] P. Palacios, I. Aguilera, K. Sanchez, J. C. Conesa, and P. Wahnan, Phys. Rev. Lett. **101**, 046403 (2008).
[2] A. Luque, and A. Martin, Phys. Rev. Lett. **78**, 5014 (1997).
[3] A. Luque, A. Martä, E. Antolyn, and C. Tablero, Physica B: Condensed Matter **382**, 320 (2006).
[4] T. Jawinski, L. A. Wägele, R. Scheer, M. Grundmann, and H. von Wenckstern, Phys. Status Solidi A **215**, 1700827 (2018).

2.6 Strain States and Relaxation of α-$(Al_xGa_{1-x})_2O_3$ Thin Films on Prismatic Planes of α-Al_2O_3

M. Kneiß, D. Splith, H. von Wenckstern, M. Lorenz, T. Schultz, N. Koch, M. Grundmann

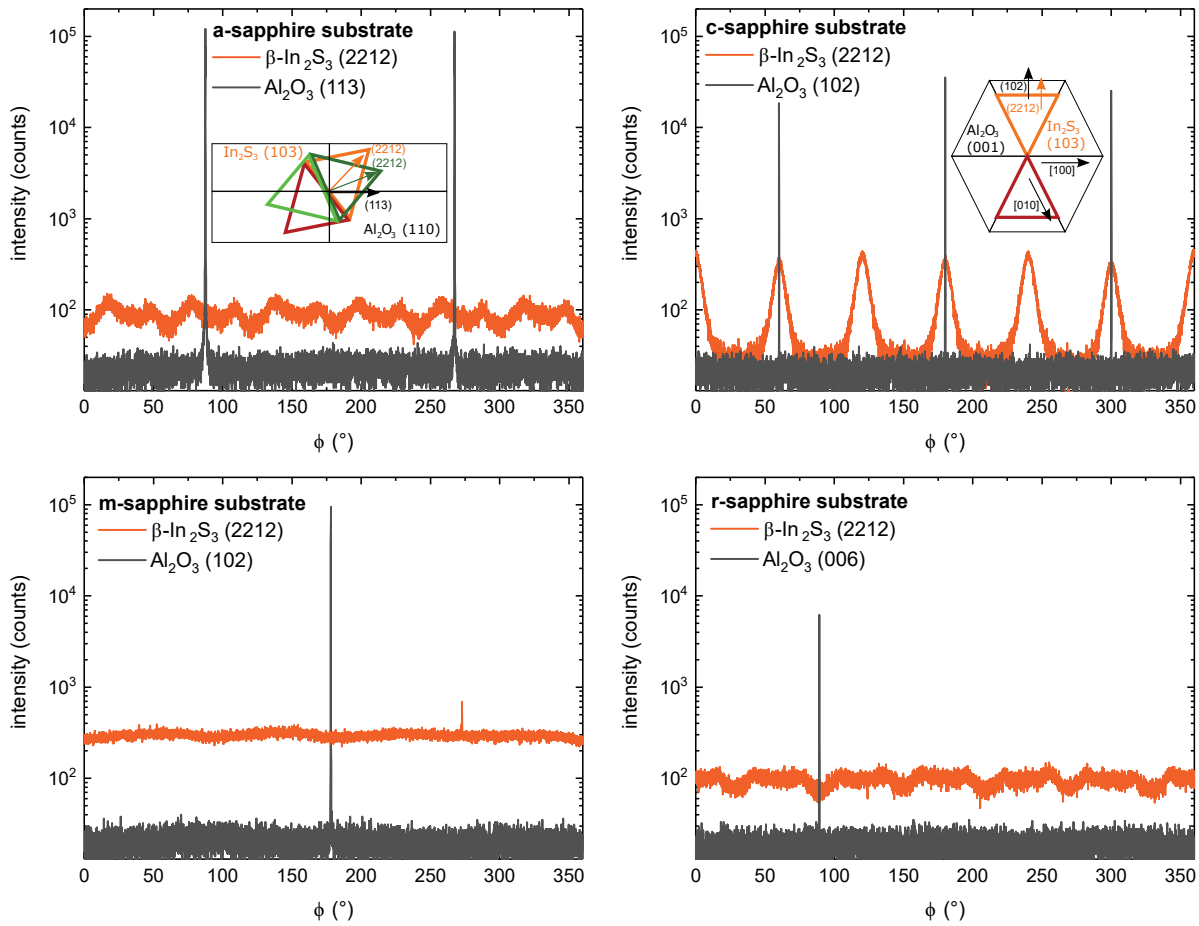

Figure 2.5: X-ray diffraction 2φ-scans of In_2S_3 thin films grown on sapphire substrates as labeled.

The metastable rhombohedral α-modification of the ultrawide bandgap semiconductor Ga_2O_3 is a promising power device material with unique properties. As it features the largest bandgap among the polymorphs of Ga_2O_3 of about 5.3 eV [1], it is also expected to exceed the already large predicted electric breakdown field of the thermodynamically stable monoclinic β-modification of about 8 MV/cm [1]. Although no large size single crystal wafers can be grown from the melt in contrast to β-Ga_2O_3, cost-effective isostructural α-Al_2O_3 substrates (sapphire) are widely available. The identical crystal symmetry of α-Ga_2O_3 and α-Al_2O_3 further allows for alloying between these two binary materials without any miscibility gap and enables a large energy range for bandgap engineering from 5.3 eV to about 8.8 eV ($E_g(\alpha\text{-}Al_2O_3)$) [3–5]. This renders this phase promising for α-$(Al_xGa_{1-x})_2O_3$ heterostructure devices such as high-electron mobility transistors (HEMTs) similar to the AlGaN/GaN system, but with unprecedentedly high expected breakdown voltages. However, for the high-quality pseudomorphic growth of such α-$(Al_xGa_{1-x})_2O_3$ heterostructures and the design of devices, precise knowledge of the elastic constants and relaxation mechanisms of the material is required. Unlike α-Al_2O_3, for which the elastic constants as entries of the stress-strain tensor C_{ij} are well known in theory and confirmed by experiment, mostly only theoretical values are available in literature for α-Ga_2O_3 [6]. Based on our stress-strain theory as developed in Ref. [7], several theoretical values of C_{ij} and the validity of a linear inter-

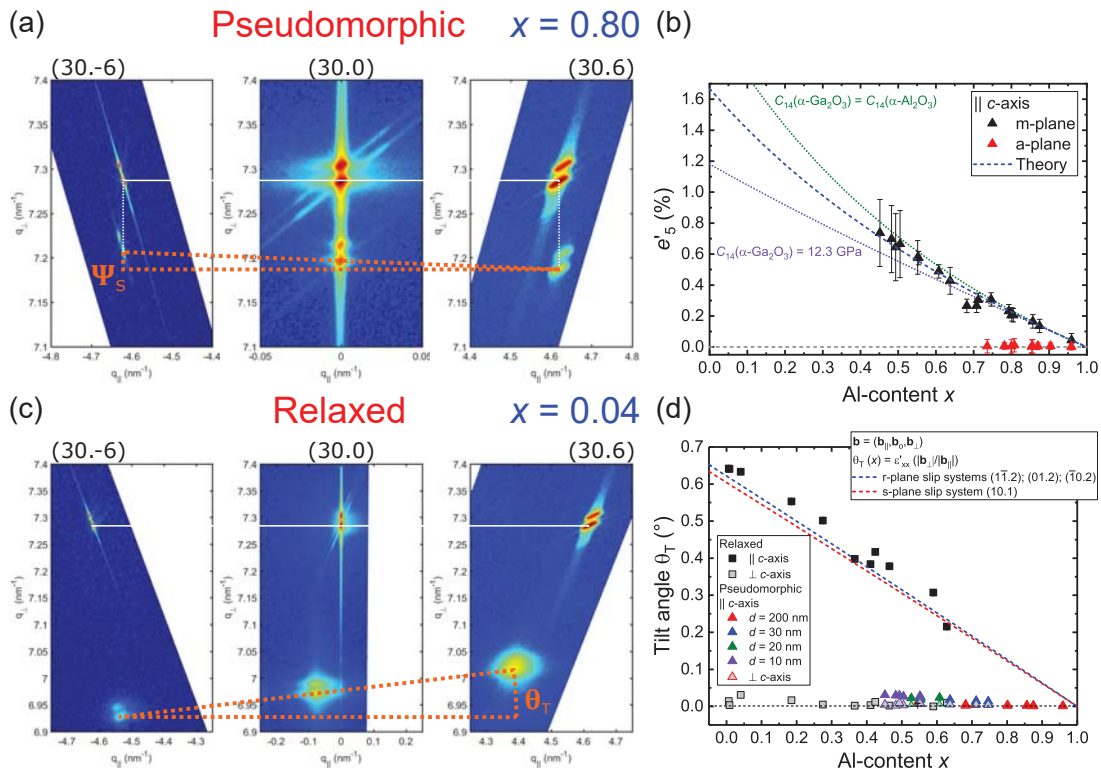

Figure 2.6: (a) Typical RSM measurements of asymmetric $(30.\bar{6})$ and (30.6) as well as symmetric (30.0) reflections of a pseudomorphic α-$(Al_{0.80}Ga_{0.20})_2O_3$ thin film on m-plane sapphire. Intense reflections in the upper part of the RSMs are always substrate reflections with distinct $K_{\alpha1}/K_{\alpha2}$ splitting with less intense thin film reflections below. A lattice shear is evident by the non-identical position of the reflections in the $q_\perp$ coordinate. The corresponding shear angle of the lattice Ψ_S is indicated. (b) Shear strain $e'_5 = \tan\Psi_S$ as function of x for pseudomorphic α-$(Al_xGa_{1-x})_2O_3$ on m-plane and a-plane sapphire as determined from RSM measurements. An excellent agreement with the theoretically expected e'_5 for m-plane growth given by the blue dashed curve corresponding to eq. 2.1 is found. (c) Typical RSM measurements of asymmetric $(30.\bar{6})$ and (30.6) as well as symmetric (30.0) reflections of a relaxed α-$(Al_{0.04}Ga_{0.96})_2O_3$ thin film on m-plane sapphire. In contrast to pseudomorphic films, no lattice shear, but a global lattice tilt along the c-axis direction with a corresponding tilt angle θ_T can be observed. (d) Tilt angle θ_T as function of x for α-$(Al_xGa_{1-x})_2O_3$ layers on m-plane sapphire. The dashed curves are theoretically expected lattice tilts of fully relaxed layers considering the total tilt and edge components $\mathbf{b}_\perp$ and $\mathbf{b}_\parallel$, respectively, of the Burger's vectors of possible r-plane or s-plane slip systems responsible for strain relaxation in c-axis direction

polation between the values of α-Ga_2O_3 and α-Al_2O_3 for $C_{ij}(x)$ for the alloy system could already be confirmed by analyzing epitaxial strain in pseudomorphic α-$(Al_xGa_{1-x})_2O_3$ thin films on the pyramidal r- and r'-planes of sapphire [8, 9]. Interestingly, in contrast to true hexagonal systems such as GaN, the threefold pseudohexagonal rhombohedral $R\bar{3}c$ symmetry of the corundum structure entails that r- and r'-planes are not crystallographically equivalent and that a non-vanishing C_{14} component of the stress-strain tensor is expected. This also corresponds to an inequivalence of the epitaxial strains and relaxation processes for pseudomorphic layers on the prismatic m-plane and a-plane of sapphire. As a consequence of the non-vanishing C_{14} component, a shear strain e'_5 and a corresponding lattice shear in c-axis direction are only expected for pseudomorphic

m-plane α-$(Al_xGa_{1-x})_2O_3$ heterostructures. Especially the m-plane has been reported as promising for device applications since the α-phase can be stabilized more easily [5] and up to three times higher electron mobilities were observed for m-plane α-Ga_2O_3 compared to other growth planes [10]. Knowledge about the critical elastic constants and relaxation mechanisms for the prismatic planes is therefore crucial. Unfortunately, r- and r'-planes are rather insensitive to variations in C_{14}, such that its theoretical value could not have been confirmed yet in our previous studies [8, 9]. Relaxation mechanisms and differences of the prismatic m- and a-planes are so far unknown as well.

We therefore analyzed the epitaxial strains and relaxation processes for α-$(Al_xGa_{1-x})_2O_3$ thin films deposited by combinatorial PLD on m-plane and a-plane sapphire substrates in the whole composition range of the alloy $0 \leq x \leq 1$. Pseudomorphic growth on m-plane sapphire with high crystalline quality has been achieved for $x \gtrsim 0.45$ verified by sharp reflections in reciprocal space map (RSM) measurements which are accompanied by intense Laue fringes up to high orders for low epilayer thicknesses (not shown). Fig. 2.6 (a) shows RSM measurements of asymmetric $(30.\bar{6})$ and (30.6) as well as symmetric (30.0) reflections of an exemplary pseudomorphic 200 nm thick α-$(Al_{0.80}Ga_{0.20})_2O_3$ layer on m-plane sapphire. As expected, a pronounced shear strain is evidenced by a shift of the position of the asymmetric reflections in the $q_\perp$ coordinate of the reciprocal space compared to the symmetric (30.0) reflection in the same azimuth. This corresponds to a lattice shear in real space in c-axis direction by the shear angle Ψ_S as indicated in the figure. No shear strain can be observed for the asymmetric $(4\bar{2}.0)$ and (22.0) reflections and the symmetric (30.0) reflections in the same azimuth with the a-axis in the plane of incidence of the X-ray beam, i.e. no lattice shear in a-axis direction. Similarly, no reflections of pseudomorphic a-plane α-$(Al_xGa_{1-x})_2O_3$ showed any sign of shear strain. This is in perfect agreement with stress-strain theory and proves the inequivalence of m- and a-plane regarding shear strain. Lattice constants as well as the shear strain were determined for the pseudomorphic layers from the RSM measurements and compared to the theoretically calculated values as function of Al-content for which all elastic constants $C_{ij}(x)$ were linearly interpolated between the values of α-Ga_2O_3 and α-Al_2O_3. The strained lattice constants are in excellent agreement with theory (not shown) and no significant difference has been found between m-plane and a-plane epilayers due to the insensitivity of the responsible strain e'_3 on C_{14}. The shear strain $e'_5 = \tan \Psi_S$ as shown in Fig. 2.6 (b) as function of x, however, reveals a significant difference and vanishes for a-plane growth as expected. The evolution of e'_5 can be reproduced with high accuracy by the theoretically expected e'_5 [7]:

$$e'_5 = 2\varepsilon'_{xz} = \frac{C_{14}\left[C_{13}\, e'_1 + (C_{11} + C_{12})\, e'_2\right]}{C_{11}C_{44} - C_{14}^2} \tag{2.1}$$

where e'_1 and e'_2 are the known fully-strained in-plane values of the epitaxial strain. Since e'_5 is directly proportional to C_{14}, this allowed an accurate fit of the experimental data for $C_{14}(\alpha\text{-}Ga_2O_3)$ and delivered $C_{14}(\alpha\text{-}Ga_2O_3) = (15.8 \pm 1.7)$ GPa, verifying the theoretically predicted value of $C_{14}(\alpha\text{-}Ga_2O_3) = 17.3$ GPa [6].

In contrast to the pseudomorphic samples, fully relaxed layers beyond the critical thickness on m-plane sapphire exhibit a significant global lattice tilt in c-axis direction as can be clearly observed from the shift of the symmetric (30.0) reflection from $q_\parallel = 0$ and

the corresponding shift of the asymmetric reflections in RSMs as exemplarily shown in Fig.2.6 (c). Such lattice tilt is caused by a non-vanishing net tilt component of the Burger's vectors belonging to the slip systems responsible for the strain relaxation. Strain relaxation in *c*-axis direction corresponding to a non-vanishing edge component of the Burger's vectors in that direction can only be mediated by pyramidal slip systems, i.e. r- or s-slip planes and associated Burger's vectors, for the prismatic growth planes. The non-vanishing net tilt component of the Burger's vectors of all possible r- or s-plane slip systems is now caused by the three-fold symmetry of the crystal. For true hexagonal systems, the six equivalent r- or s-planes cause a pairwise compensation of the tilt components of the Burger's vectors, which is not the case for the rhombohedral symmetry, where only three equivalent r- or s-planes exist. This results in a net tilt component for the relaxation of m-plane epilayers. For a-plane epilayers, only two r- or s-planes can contribute to strain relaxation, causing the tilt components of the Burger's vectors to compensate pairwise and no global lattice tilt is observed. By analyzing the possible slip planes, the total strain released and the magnitudes of the tilt and edge components of the possible Burger's vectors, the expected tilt angle of the lattice can be calculated as function of *x*. In comparison to the experimentally obtained tilt angles, as shown in Fig. 2.6 (d) as function of *x*, the responsible slip systems can be identified. Here, all three possible (01.2), $(1\bar{1}.2)$ and $(\bar{1}0.2)$ r-slip planes or only the (10.1) s-slip plane and their associated Burger's vectors have been found to reproduce the experimentally observed tilt angles with good agreement, see blue or red dashed line in Fig. 2.6 (d).

In conclusion, we were able to deposit α-$(Al_xGa_{1-x})_2O_3$ thin films with high crystalline quality on prismatic planes of sapphire in the whole composition range. RSM measurements and theoretical modeling of the determined epitaxial strains for pseudomorphic layers allowed the verification of theoretically calculated entries of the elastic tensor for the alloy system. Especially the value of the critical C_{14} component responsible for shear strain in m-plane epilayers could be confirmed for the first time. RSM measurements on relaxed layers showed a global lattice tilt for m-plane epilayers, not observed on the a-plane. A theoretical modeling of the tilt angle as function of *x* further allowed for the identification of possible slip systems responsible for strain relaxation. These findings could find application in future heterostructure devices based on α-$(Al_xGa_{1-x})_2O_3$. The detailed study can be found in Ref. [11].

[1] Shinohara and Fujita, Jpn. J. Appl. Phys. **47**, 7311 (2008)
[2] Higashiwaki *et al.*, Semicond. Sci. Technol. **31**, 034001 (2019)
[3] Fujita *et al.*, Jpn. J. Appl. Phys. **55**, 1202A3 (2016)
[4] Dang *et al.*, Apl. Phys. Lett. **113**, 062102 (2018)
[5] Jinno*et al.*, Sci. Adv. **7**, eabd5891 (2021)
[6] Furthmüller and Bechstedt, Phys. Rev. B **93**, 115204 (2016)
[7] Grundmann, J. Appl. Phys. **124**, 185302 (2018)
[8] Grundmann and Lorenz, APL Materials **8**, 021108 (2020)
[9] Grundmann and Lorenz, Physica Status Solidi B **258**, 2100104 (2021)
[10] Akaiwa *et al.*, Phys. Status Solidi A **217**, 1900632 (2020)
[11] Kneiß *et al.*, J. Mater. Res. **36**, 4816-4831 (2021)

2.7 κ-$(Al_xGa_{1-x})_2O_3$ on ZnO Back Contacts: Highly Rectifying κ-Ga_2O_3 Diodes by a Vertical Device Layout

Ga_2O_3 received tremendously increasing research interest as wide bandgap semiconductor in recent decades. The lions share of the research is focused on the thermodynamically stable monoclinic β-modification which exhibits a large bandgap of about 4.6 eV and a large predicted electric breakdown field of about 8 MV/cm [1] rendering it a promising material for power device applications. The possibility of homoepitaxy on large size single crystal wafers grown from the melt further triggered these research efforts. Lately, interest sparked for the metastable phases of Ga_2O_3, one of those being the orthorhombic κ-modification. It is the only known phase of Ga_2O_3 expected to exhibit a large spontaneous electrical polarization of about 23 μC/cm^2 along its c-axis [2]. This can be utilized to localize a 2DEG at heterointerfaces due to polarization discontinuities, e.g. at the interfaces of κ-Ga_2O_3/κ-$(Al_xGa_{1-x})_2O_3$, κ-Ga_2O_3/κ-$(In_xGa_{1-x})_2O_3$ or κ-$(In_xGa_{1-x})_2O_3$/κ-$(Al_xGa_{1-x})_2O_3$ heterostructures. 2DEGs are attractive as active layer in high-electron mobility field-effect transistors (HEMTs) due to high carrier densities and mobilities, but can also be utilized for quantum well infrared photodetectors (QWIPs), where the ground state of the QWs can be populated this way without extrinsic dopants. The alloy systems κ-$(Al_xGa_{1-x})_2O_3$ and κ-$(In_xGa_{1-x})_2O_3$ can be stabilized for a broad range of alloy compositions employing e.g. pulsed laser deposition (PLD) [3–6]. The incorporation of Al increases the bandgap of κ-Ga_2O_3 and In incorporation decreases it, allowing a wide range of up to 2.5 eV for bandgap engineering [3–6]. Additionally, by determining the band offsets in heterostructures, we found that the full range of bandgap variation is also available as conduction band offsets [7], allowing for a large tunable wavelength range for QWIPs from far IR to the visible spectral range. High-quality κ-Ga_2O_3/κ-$(Al_xGa_{1-x})_2O_3$ QW superlattice (SL) heterostructures have also been reported previously [8].

Nevertheless, large remaining issues are the conductivity and contacting of κ-phase thin films. When deposited on insulating substrates, lateral currents at the measurement limit of our setups in the order of 10^{-13} A can only be detected. Available literature on doped κ-Ga_2O_3 thin films report only low conductivities as well with resistivities in the order of 1 Ωcm [9]. Rectifying contacts or diode structures as prerequisite for QWIPs or HEMTs are lacking completely in literature. We suspect this to be due to the growth of κ-phase layers in three nanocrystalline rotational domains. The high density domain boundaries could pose barriers for lateral current transport effectively suppressing lateral conductivity. However, these domains typically grow in a columnar fashion with one domain possibly extending across the whole thin film in growth direction. Vertical current transport should therefore be possible and only needs to be enabled by a sufficient sample structure. These issues will be tackled in the next two sections utilizing a sample structure where the κ-phase layer is deposited on highly conductive Al-doped ZnO back contact layers. First, the growth of κ-$(Al_xGa_{1-x})_2O_3$ on these templates will be evaluated in the first section, while the second section deals with the proof of the current anisotropy employing these structures and the realization of first highly rectifying diode structures based on Schottky or p-type contacts.

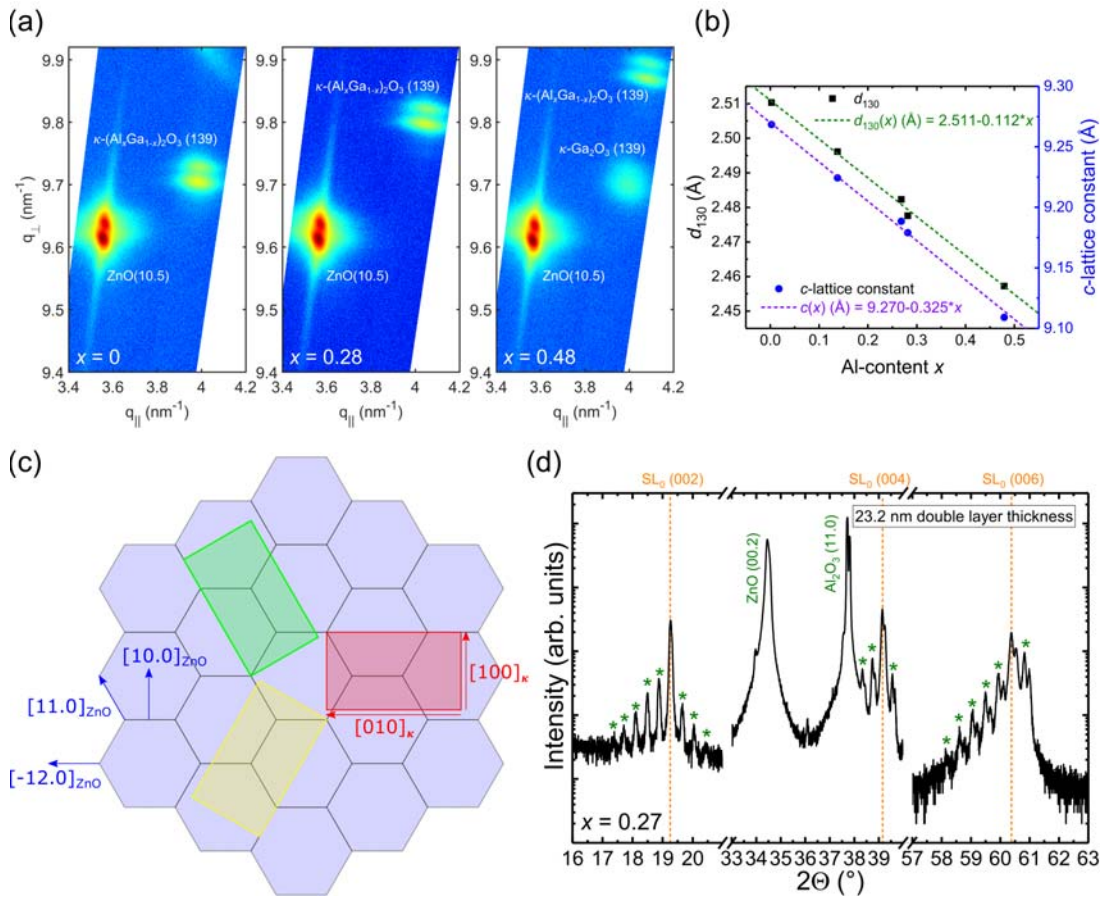

Figure 2.7: (a) Typical RSMs around the asymmetric (139) reflection of κ-$(Al_xGa_{1-x})_2O_3$ layers on ZnO/Al-doped ZnO growth templates on a-plane sapphire with different Al-content x as indicated. The position of the asymmetric (10.5) reflection of the growth template is denoted as well. The κ-Ga_2O_3 (139) reflection for $x = 0.48$ is caused by a binary κ-Ga_2O_3 layer necessary for the stabilization of the κ-phase for $x \geq 0.4$. (b) Out-of-plane c-lattice constant and in-plane d_{130} lattice plane distance of the κ-$(Al_xGa_{1-x})_2O_3$ layers extracted from the RSMs as function of x. Dashed lines correspond to the denoted linear relations following Vegard's law. (c) Possible configurations of the orthorhombic unit cell of the κ-$(Al_xGa_{1-x})_2O_3$ layers for the three rotational domains on the ZnO (00.1) surface as determined from XRD ϕ scans. (d) Typical XRD 2θ-ω scan of a 15 layer pair κ-$(Al_{0.27}Ga_{0.73})_2O_3$/$\kappa$-$Ga_2O_3$ SL heterostructure on an Al-doped ZnO growth template on a-plane sapphire. SL_0 denotes the zero order reflections of the SL structure, while green asterisks denote sharp SL fringes that occur up to high orders

2.7.1 Growth of High Quality κ-$(Al_xGa_{1-x})_2O_3$ Layers and Superlattice Heterostructures on ZnO Templates

M. Kneiß, P. Storm, A. Hassa, D. Splith, H. von Wenckstern, M. Lorenz, M. Grundmann

κ-$(Al_xGa_{1-x})_2O_3$ layers with different Al-contents were grown by tin-assisted PLD on a thin film template structure consisting of unintentionally doped ≈ 400 nm thick ZnO on ≈ 200 nm thick heavily Al-doped ZnO also deposited by PLD on a-plane sapphire substrates. SnO_2 containing $(Al,Ga)_2O_3$ targets are necessary to stabilize the κ-phase with tin acting as surfactant without being incorporated significantly in the bulk of the layer [10]. ZnO was the material of choice for the template, since it crystallizes in

a hexagonal wurtzite crystal structure, can be grown with high quality by PLD and degenerate n-type doping can be achieved employing Al or Ga as dopants. Further, a hexagonal (00.1) surface, as expected epitaxial orientation of ZnO on a-plane sapphire, is typically required for κ-phase growth with high crystalline quality. A ZnO target with 1 wt.% Al_2O_3 was selected for the Al-doped ZnO layer resulting in a highly conductive back contact ($\rho \approx 10^{-5}\,\Omega$m, $n \approx 6 \times 10^{19}\,\mathrm{cm}^{-3}$, $\mu \approx 50\,\mathrm{cm}^2\,(\mathrm{Vs})^{-1}$).
Fig. 2.7 (a) shows reciprocal space map (RSM) measurements of the asymmetrical (139) reflections of three selected κ-$(Al_xGa_{1-x})_2O_3$ layers with different Al-contents on the ZnO(00.1) growth templates. Typical (001) oriented growth in the κ-modification was observed for all investigated Al-contents in the range of $0 \leq x \leq 0.48$. A low broadening of the reflections almost independent of Al-content confirms the high crystalline quality of the layers. A shift of the (139) reflections to higher $q_{\|}$ as well as $q_{\perp}$ with increasing x is in agreement with the expected decrease of in- and out-of-plane lattice constants upon incorporation of Al. The out-of-plane c-lattice constant as well as the in-plane d_{139} lattice plane distance as determined from the RSMs are shown in Fig. 2.7 (b) as function of x. A linear decrease in agreement with Vegard's law can be observed in both cases. The linear relations are close to those reported for κ-$(Al_xGa_{1-x})_2O_3$ layers on c-plane sapphire substrates [5, 6]. XRD ϕ scans were employed to determine the epitaxial relationships with the ZnO templates. Epitaxial growth in three orthorhombic rotational domains was confirmed similar to most other substrates. The possible configurations of the three rotational domains on the (00.1) ZnO surface are depicted schematically in Fig. 2.7 (c). The in- and out-of-plane epitaxial relationships can be deduced as κ-Ga_2O_3 $\langle 100\rangle \parallel \langle 10.0\rangle$ ZnO, κ-Ga_2O_3 $\langle 010\rangle \parallel \langle \bar{1}2.0\rangle$ ZnO, and κ-Ga_2O_3 [001] $\parallel$ [00.1] ZnO. Interestingly, this corresponds to a rotation of the unit cells of the rotational domains by 30° compared to the configuration on c-plane sapphire minimizing the lattice mismatch. Further atomic force microscopy measurements confirmed smooth surface morphologies for all Al-contents with only slightly enhanced surface roughness compared to the growth on c-plane sapphire caused by the initial ZnO roughness (not shown).

Finally, to also prove the possibility to grow high quality heterostructures on these ZnO templates for QWIP applications, 15 layer pair κ-$(Al_xGa_{1-x})_2O_3$/κ-Ga_2O_3 SL heterostructures were deposited on Al-doped ZnO templates on a-plane sapphire. Fig. 2.7 (d) shows a typical XRD 2θ-ω scan of a SL heterostructure with $x = 0.27$ and nominal 3 nm κ-Ga_2O_3 QW thickness and 20 nm κ-$(Al_xGa_{1-x})_2O_3$ barrier thickness per layer pair. Apart from the zero order reflections of the SL structure denoted SL_0, sharp SL fringes up to high orders can be observed marked with green asterisks. This confirms an excellent crystalline quality and coherent growth of the SL structure as well as very smooth interfaces similar to SL structures on c-plane sapphire in literature [8]. The double layer thickness of 23 nm estimated from the separation of the SL fringes is also in excellent agreement with the design.

These findings confirm that κ-$(Al_xGa_{1-x})_2O_3$ layers and SL heterostructures on ZnO back contact layer templates exhibit similar crystalline quality and surface morphology as those grown on c-plane sapphire substrates making them promising for the use in κ-phase device applications. The complete study has been published in Ref. [11].

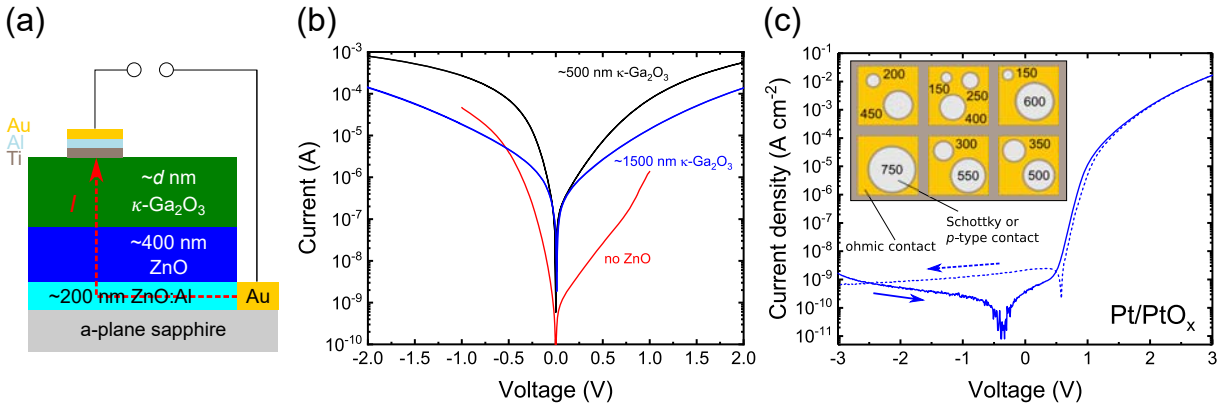

Figure 2.8: (a) Schematic cross sectional vertical device structure with nominal ohmic Ti/Al/Au contact layer stacks on top of the active κ-Ga_2O_3 layer contacted in front-back geometry. The red arrow denotes a possible current path from a DC-sputtered gold contact at the corner of the sample to the nominally ohmic contact on top of the structure. (b) *IV* characteristics of nominally ohmic contacts in front back geometry for two samples with different κ-Ga_2O_3 thickness in comparison to a sample without unintentionally doped ZnO layer. (c) Highly rectifying *jV* characteristic of one of the best reactively sputtered Pt/PtO_x Schottky contacts measured in front-front geometry. Blue arrows denote the direction of the voltage sweep. The utilized lateral contact layout was structured on top of the κ-Ga_2O_3 layer as repeating sequence of the schematic pattern in the inset

2.7.2 Realization of Highly Rectifying κ-Ga_2O_3 Schottky Barrier Diodes and *pn* Heterojunctions by Overcoming the Conductivity Anisotropy

M. Kneiß, D. Splith, P. Schlupp, A. Hassa, H. von Wenckstern, M. Lorenz, M. Grundmann

Binary κ-Ga_2O_3 layers on ZnO back contacts as investigated above were now utilized to fabricate vertical device structures. We employed two different contact configurations, a front-back and a front-front contact layout. The front-back layout is schematically depicted in Fig. 2.8 (a). Here, the back contact layer is directly contacted by a sputtered gold layer at the corner of the sample. On top of the κ-Ga_2O_3 layer, the investigated contacts are deposited and patterned by photolithography. In this case, an annealed Ti/Al/Au layer stack is depicted that should serve as nominally ohmic contact proven to exhibit linear current-voltage (*IV*) characteristics in the case of β-Ga_2O_3. In the front-front configuration, two patterned contacts on top of the κ-Ga_2O_3 layer are utilized instead of the gold contact. Both of these configurations enable the current to flow in a vertical direction without charge carriers being forced to cross domain boundaries. The lateral distance is covered by current flow through the Al-doped back contact layer as indicated by the current path depicted as red arrow in Fig. 2.8 (a). A conductivity anisotropy caused by the domain boundaries should express itself now in a greatly increased current density j in this configuration. As evident in the *IV*-characteristic of the nominally ohmic contacts in Fig. 2.8 (b) for two different κ-Ga_2O_3 layer thicknesses, this is indeed the case. While current flow in lateral contact configurations for layers directly deposited on c-plane sapphire is severely suppressed to $j \lesssim 10^{-9}$ A cm^{-2}, for the vertical device layout, we obtain current densities exceeding 0.1 A cm^{-2} at 2 V

bias. An unintentionally doped ZnO layer was found to be necessary as otherwise rectifying characteristics are obtained possibly caused by a barrier developing at the κ-Ga_2O_3/ZnO:Al interface due to unfavorable band alignment, see red curve in Fig. 2.8 (b) corresponding to a structure without ZnO layer. The unintentionally doped ZnO layer is suggested to equilibrate the conduction bands [12] and reduce the barrier. A complete elimination of the barrier might not have been achieved as evident from the nonlinear *IV* characteristics of the ohmic contacts.

Rectifying contacts as prerequisite for device applications were realized either by depositing Pt or Pd via reactive DC-sputtering to form Pt/PtO_x or Pd/PdO_x Schottky contacts (SCs), respectively, to obtain Schottky barrier diodes (SBDs) or by depositing p-type NiO or $ZnCo_2O_4$ by PLD to obtain *pn*-heterojunction diodes. For the measurement of *jV* characteristics, the front-front configuration was utilized in contact patterns as depicted in the inset of Fig. 2.8 (c), where the circular rectifying contacts are surrounded by the nominally ohmic contact layer stack employed as second contact. Highly rectifying *jV* characteristics were obtained for diode ensembles of every type of contact with up to seven orders of magnitude current rectification ratio on average at ±3 V bias without a significant amount of defective devices even in ensembles containing up to 87 contacts. This also confirms the expected *n*-type nature of the κ-Ga_2O_3 layers. An exemplary diode characteristic of one of the best Pt/PtO_x SCs is depicted in Fig. 2.8 (c). Low reverse current densities in the order of $10^{-9}\,\mathrm{A\,cm^{-2}}$ are similar to comparable β-Ga_2O_3 based diode structures [13]. The forward current density is still limited to about $10^{-2}\,\mathrm{A\,cm^{-2}}$ possibly caused by the barrier at the back contact as evident from the non-ohmic forward characteristic at voltages where the series resistance should dominate. This might be improved by a different choice of the back contact material in the future. The room-temperature *jV* characteristics of the diodes were modeled to extract the ideality factor η and additionally the effective Schottky barrier height $\phi_\mathrm{B}^\mathrm{eff}$ in case of the SBDs. Values of η as low as 1.3 as well as an homogeneous barrier height of $\phi_\mathrm{B}^\mathrm{hom} \approx 1.44\,\mathrm{eV}$ estimated from $\phi_\mathrm{B}^\mathrm{eff}$ vs. η plots (not shown) for the Pt/PtO_x SBD ensembles further confirmed similar properties as comparable β-Ga_2O_3 based diodes [13]. Temperature-dependent *jV*-measurements and modeling of selected Pt/PtO_x SBDs (not shown) finally revealed a mean barrier height of the Gaussian distributed laterally inhomogeneous barrier height of $\phi_\mathrm{B}^\mathrm{m} \approx 2.1\,\mathrm{eV}$ on average and a broadening of the distribution of about 200 meV, both similar to β-Ga_2O_3 based devices as well.

In conclusion, utilizing a vertical device layout with back contact layer, a suspected strong conductivity anisotropy in κ-Ga_2O_3 layers caused by rotational domain boundaries could be proven. The enabled current flow through κ-Ga_3O_3 by these device structures was then successfully utilized to fabricate and characterize worldwide first highly rectifying diode structures based on κ-Ga_2O_3. Furthermore, these diodes show similar quality as diodes based on monoclinic Ga_2O_3 corroborating the large potential of this phase for heterostructure device applications such as HEMTs or QWIPs. The complete study can be found in Ref. [14].

[1] Higashiwaki *et al.*, Semicond. Sci. Technol. **31**, 034001 (2019)
[2] Maccioni and Fiorentini, Appl. Phys. Express **9**, 041102 (2016)
[3] Kneiß *et al.*, APL Materials **7**, 022516 (2019)
[4] Hassa *et al.*, APL Materials **7**, 022525 (2019)
[5] Storm *et al.*, APL Materials **7**, 111110 (2019)

[6] Hassa *et al.*, APL Materials **8**, 021103 (2020)
[7] Schultz, Kneiß *et al.*, ACS Appl. Mater. Interfaces **12**, 8879 (2020)
[8] Kneiß *et al.*, APL Materials **8**, 051112 (2020)
[9] Parisini *et al.*, APL Materials **7**, 031114 (2019)
[10] Kneiß *et al.*, APL Materials **7**, 022516 (2019)
[11] Kneiß *et al.*, Phys. Status Solidi B **258**, 2000359 (2021)
[12] Splith *et al.*, Phys. Status Solidi A **211**, 40-47 (2014)
[13] Müller *et al.*, Semicond. Sci. Technol. **32**, 065013 (2017)
[14] Kneiß *et al.*, J. Appl. Phys. **130**, 084502 (2021)

2.8 Band alignment of Al_2O_3 on α-$(Al_xGa_{1-x})_2O_3$

H. von Wenckstern, X. Xia*, N.S. Al-Mamun†, C. Fares*, A. Haque†, F. Ren‡, A. Hassa, M. Grundmann, S.J. Pearton‡

*Department of Chemical Engineering, University of Florida
†Department of Mechanical Engineering, The Pennsylvania State University
‡Department of Materials Science and Engineering, University of Florida

The band offsets between Al_2O_3 and α-$(Al_xGa_{1-x})_2O_3$ was investigated by X-ray photoelectron spectroscopy (XPS) as function of the alloy composition x[1]. A ternary α-$(Al_xGa_{1-x})_2O_3$ thin film was grown heteroepitaxially on a two-inch in diameter a-plane sapphire substrate by continuous composition spread pulsed laser deposition (CCS-PLD) at a growth temperature of about 640°C[3]. CCS-PLD allows the composition of ternary or multinary systems to be varied systematically in lateral direction [2]. The α-$(Al_xGa_{1-x})_2O_3$ thin film covers an alloy range from $0.13 \leq x \leq 0.84$ and does not show phase separation[3]. For selected compositions of $x = 0.26, 0.42, 0.58,$ and 0.74 Al_2O_3 was grown on top of α-$(Al_xGa_{1-x})_2O_3$ by atomic layer deposition at 200°C using trimethylaluminum as precursors and an inductively coupled O_2 plasma at 300 W[1]. Two different Al_2O_3 layer thicknesses of 200 nm and 1.5 nm were grown for measuring bandgaps by reflection electron energy loss spectroscopy[4] and core levels for the determination of valence band offsets by Kraut's method[5], respectively. Structural properties were examined by cross-sectional transmission electron microscopy (TEM), the chemical composition was determined by energy dispersive X-ray spectroscopy. The TEM investigations reveal a polycrystalline nature for Al compositions investigated. The grain size decreases with increasing Al-content. The valence band offset of Al_2O_3 calculated for the different compositions of α-$(Al_xGa_{1-x})_2O_3$ are: 0.13 eV ($x = 0.26$ and $x = 0.42$), −0.07 eV ($x = 0.56$) and −0.17 ($x = 0.74$). In order to deduce the conduction band offset, the bandgap of α-$(Al_xGa_{1-x})_2O_3$ was determined by XPS[4] for each composition and yield values of 5.8 eV, 6.1 eV, 6.4 eV and 7.0 eV for $x = 0.26, 0.42, 0.58,$ and 0.74. Using a bandgap for Al_2O_3 of 6.9 eV, the conduction band offsets are 0.97 eV ($x = 0.26$), 0.67 eV ($x = 0.46$), 0.57 eV ($x = 0.58$) and 0.07 eV ($x = 0.74$). A schematic of the band diagrams is shown in Figure 2.9. The valence band offsets are small for the entire composition range and not sufficient for the confinement of holes at the Al_2O_3/α-$(Al_xGa_{1-x})_2O_3$ interface. For $x < 0.6$ the conduction band offset is sufficient

for effective electron confinement. The band alignment is straddling type I (staggered type II) for $x < 0.5$ ($x > 0.5$).

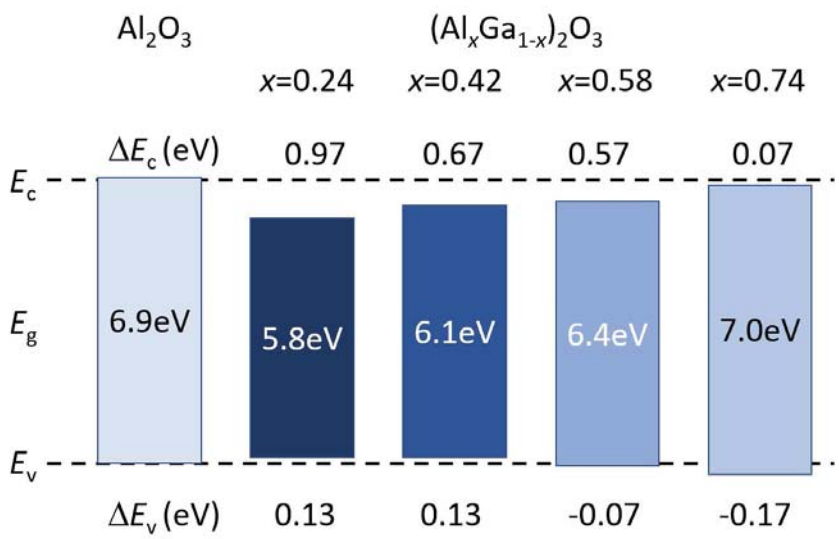

Figure 2.9: Band diagrams for Al_2O_3/α-$(Al_xGa_{1-x})_2O_3$ heterostructures.

[1] X. Xia, N. S. Al-Mamun, C. Fares, A. Haque, F. Ren, A. Hassa, H. von Wenckstern, M. Grundmann, S.J. Pearton, ECS J. Solid State Sci. Techn. **11**, 025006:1-8 (2022).
[2] H. von Wenckstern, M. Kneiß, A. Hassa, P. Storm, D. Splith, M. Grundmann, Phys. Status Solidi B **257**, 1900626 (2020).
[3] A. Hassa, P. Storm, M. Kneiß, D. Splith, H. von Wenckstern, M. Lorenz, and M. Grundmann, Phys. Status Solidi B **258**, 2000394 (2021).
[4] C. Fares, M. Kneiß, H. von Wenckstern, M. Tadjer, F. Ren, E. Lambers, M. Grundmann, and S. J. Pearton, ECS J. Sol State Sci. Technol. **8Q**, P351 (2019)
[5] E. A. Kraut, R. W. Grant, J. R. Waldrop, and S. P. Kowalczyk, Phys. Rev. Lett. **44**, 1620 (1980).

2.9 Fermi level controlled point defect balance in ion irradiated indium oxide

H. von Wenckstern*, J. Borgersen*, K.M. Johansen*, L. Vines*, M. Grundmann, A. Kuznetsov*

*Department of Physics, University of Oslo, Norway

Ion irradiation of In_2O_3 was used to study the Fermi level controlled charge state of Frenkel defects introduced in this transparent conducting oxide [1]. The investigated samples include nominally undoped, Sn donor-doped and Mg acceptor-doped thin films grown by pulsed laser deposition on c-plane sapphire substrates. The samples were irradiated at 50 K by 3 MeV Si^+ ions and the electrical resistivity was measured in-situ with ion beam shut as function of the accumulated dose D. The Fermi level positions were calculated using the carrier density at 50 K of as-grown samples and as

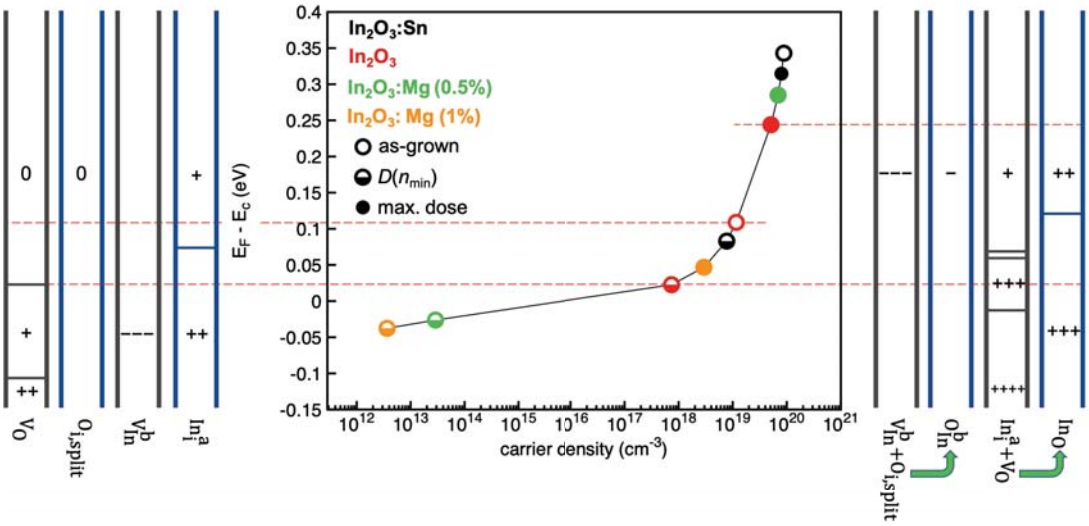

Figure 2.10: Fermi level energy relative to the conduction band minimum E_c determined for indium oxide samples as labelled at 50K for the as-grown state, the dose resulting in maximum resistivity and minimum carrier density n_{min} and maximum accumulated dose 10^{17} cm^{-2} (centre panel). Accumulated doses up to $D(n_{min})$ introduce Frenkel pairs and corresponding charge transition levels of intrinsic point defects, predicted by Chatratin *et al.*[3], are shown in the left panel. For the maximum accumulated dose secondary defects can form and corresponding charge transition levels, predicted by Chatratin *et al.*[3], are shown in the right panel. Red dashed lines are a guide to the eye. Green arrows indicate defect reactions resulting in the experimentally observed changes of the Fermi energy

function of accumulated dose. The total number of Frenkel pairs was calculated using the SRIM code[2]. For nominally undoped and Sn-doped samples the carrier density initially decreases, reaches a minimum for $D(n_{min})$, which increases with increasing Sn-doping level and initial carrier density, respectively, and increases again with further increasing accumulated dose. For Mg-acceptor doped samples, the initial resistivity is beyond the measurement limit. For $D > 10^{14}$ cm^2 it becomes measureable and decreases monotonically for higher D enabling calculation of the carrier density[1].

The dose-dependent variation in electron densisty and Fermi energy can be understood assuming that for $D \leq D(n_{min})$ primary defects (Frenkel pairs) are introduced in the In_2O_3 lattice. For $D > D(n_{min})$ the defect density is sufficiently high for defect reactions to occur such that secondary defects form. Then, changes of the Fermi energy within these two regmies can be understood considering charge transition levels (CTL) of primary and secondary defects predicted by theory[3]. Figure 2.10 summarizes the Fermi energy of all investigated sample for the as-grown state, $D(n_{min})$ and D_{max} as well as calculated CTLs of primary and secondary defects in the vicinity of the conduction band minimum E_c. We explain the experimental findings examplarily for nominally undoped In_2O_3. Initially, the thin film has degenerate electron concentration and the Fermi energy is more than 100 meV above E_c. The subsequent irradiation steps introduce Frenkel pairs (left panel of fig.2.10). Interstitial oxygen in split position ($O_{i,split}$) and the indium vacancy (V^b_{In}) on b-site do not have a CTL in the vicinity of E_c and hence a fixed charge state of 0 and −3, respectively. The oxygen vacancy (V_O) and interstial indium on a-position (In^a_{In}) have a 0/+ and a +/++ CTL, respectively, within the Fermi

energy range of interest. This implies, that the creation of a Frenkel pair in the cation and anion sublattice creates an overall charge of −2 (+1 due to the donor In^b_{In} and −3 due to the acceptor V^b_{In}). Hence, the carrier density and the Fermi energy decrease intially. It will cross the +/++ CTL of In^a_{In} and from now on a net charge of only −1 is introduced during irradiation. As soon as the Fermi energy equals the 0/+ CTL of V_O no addtional net charge is introduced and the Fermi energy is pinned. This corresponds to $D = D(n_{\min})$. Increasing the accumulated dose further leads to the formation of secondary defects (right panel of fig.2.10), since, due to the large density of Frenkel pairs, defect reaction may occur. The defect pair $V^b_{In} + O_{i,split}$ and the antisite defect O^b_{In} have a single charge state of −3 and −1, respectively, and hence the formation of O^b_{In} from $V^b_{In} + O_{i,split}$ releases two electrons into the conduction band and the Fermi energy and carrier density increase. The defect pair $In^a_{In} + V_O$ has a +/+++ CTL and for the antisite InO a ++/+++ CTL was predicted. If E_F lies above the +/+++ CTL of $In^a_{In} + V_O$ the formation of the antisite from the $In^a_{In} + V_O$ defect pair will additionally introduce electrons into the conduction band. Hence the Fermi energy and carrier concentration increase further. The variations observed for the other samples can be explained similarily.

In conclusion, in-situ characterization of electric transport properties as function of accumulated irradiation dose is a valuable methodology for benchmarking predictions on defects and their charge transition levels in semiconductors.

[1] J. Borgersen, K. M. Johansen, L. Vines, H. von Wenckstern, M. Grundmann, A. Kuznetsov, J. Appl. Phys. **130**, 085703:1-6 (2021).
[2] J. F. Ziegler, J. P. Biersack, and U. Littmark, The Stopping and Range of Ions in Solids (Pergamon Press, New York, 1985).
[3] I. Chatratin, F. P. Sabino, P. Reunchan, S. Limpijumnong, J. B. Varley, C. G. Van de Walle, and A. Janotti, Phys. Rev. Mater. **3**, 074604 (2019).

2.10 Ultrawide Bandgap Rhombohedral (001) Zn_2GeO_4 Epitaxial Thin Films

S. Luo, L. Trefflich, T. Höche*, R. Hildebrandt, E. Krüger, M. Lorenz, H. von Wenckstern, M. Grundmann

*Fraunhofer Institute for Microstructure of Materials and Systems (IMWS), Halle

Rhombohedral spinel Zn_2GeO_4 is a promising ultrawide bandgap semiconductor material. To date, there was no work reported on the epitaxial thin films of Zn_2GeO_4. Here we report the epitaxial growth of high-quality Zn_2GeO_4 thin films with [001] crystallographic orientation on c-plane sapphire substrates using pulsed laser deposition. The in-plane orientation relationships are [110] Zn_2GeO_4// [11.0] Al_2O_3 and [1-10] Zn_2GeO_4// [1-1.0] Al_2O_3. The epitaxial thin films with 380~700 nm thickness show a surface RMS roughness of less than 3 nm and exhibit a full width at half maximum (FWHM) of rocking curve of about 0.40°. The evaluated direct optical bandgap of films from UV-visible transmission spectra is about 4.92 eV. The steady-state photoluminescence spectra of films under 266 nm laser excitation at room temperature exhibit a broad defect-related blue emission band at 2.62 eV with a FWHM of 0.55 eV. This work

advances the fundamental studies on ultrawide bandgap Zn_2GeO_4 epitaxial thin films for potential device application.

Rhombohedral spinel Zn_2GeO_4 with the space group $R\bar{3}$ (No. 148), is a promising ultrawide bandgap semiconductor material with a bandgap greater than 4.5 eV, has attracted abundant of researches on its optical, dielectric, and photocatalytic properties in the past two decades. Polycrystalline Mn-doped Zn_2GeO_4 phosphor thin films present good performance in green-emitting electroluminescent device,[1–3] while the persistent luminescent Mn-doped Zn_2GeO_4 nanoparticles show a great potential in bioluminescence application.[4, 5] The Zn_2GeO_4 nanowires exhibit excellent performance in deep-UV photodetector.[6–10] Zn_2GeO_4 nanorods and nanoribbons show effectively photocatalytic activity in degradation of organics, hydrogen generation, and conversion of carbon dioxide to fuels.[10–13] Furthermore, Zn_2GeO_4 bulk ceramics exhibit good microwave dielectric properties as a promising candidate material for millimeter-wave application.[14] However, there is a lack of experimental investigation of epitaxial Zn_2GeO_4 thin films for fundamental research in view of potential device application. To be best of our knowledge, to date epitaxial thin films of rhombohedral Zn_2GeO_4 have not been reported. In order to carry out fundamental study on physical and chemical properties of the material for developing the practical device application, the heteroepitaxial growth of Zn_2GeO_4 thin films takes priority.

Heteroepitaxial growth of ultrawide bandgap Zn_2GeO_4 thin films on commercial sapphire (α-Al_2O_3 single crystal) substrates is crucial for studying their optical and electrical properties in view of device applications in optoelectronics and power electronics. Sapphire has a trigonal (rhombohedral) unit cell (space group $R\bar{3}c$, No. 167), but is generally treated as a hexagonal crystal structure (a= 4.754 Å, c= 12.982 Å, γ= 120°).[15] Considering the symmetry similarity between hexagonal (00.1) α-Al_2O_3 plane and rhombohedral (001) Zn_2GeO_4 plane (a=b= 14.284 Å, γ= 120°),[16] together with a small lattice mismatch of about 0.2 % along the a and b axis between one (001) Zn_2GeO_4 unit cell and three (00.1) α-Al_2O_3 unit cells, a heteroepitaxial interface may form between (001) Zn_2GeO_4 and (00.1) α-Al_2O_3 crystal planes through a domain matching epitaxy mechanism.[17] Here we report the heteroepitaxial growth of rhombohedral (001)-oriented Zn_2GeO_4 thin films on (00.1)-oriented α-Al_2O_3 single crystal (c-sapphire) substrates by pulsed laser deposition (PLD).

The rhombohedral Zn_2GeO_4 is a the thermodynamically stable phase under ambient conditions. A major challenge in epitaxial growth of rhombohedral Zn_2GeO_4 thin films by vapor deposition probably lies in the large difference in vapor pressure at high temperatures between Zn and Ge. The metallic Zn has a melting point of about 420 °C and a boiling point of about 907 °C, while the theoretical vapor pressure values of Zn are about 84, 336 and 1060 mbar at 700, 800 and 900 °C, respectively.[18] Whereas the melting points of metallic Ge and compound GeO_2 are around 938 °C and 1115 °C, respectively. In PLD process, the laser ablated species from target consist of Zn, Ge, Zn-O, Ge-O, and perhaps Zn-Ge-O. Among them, Zn-O easily decomposes in the gas phase upon collisions owing to the small bond energy of about 1.61 eV for ZnO.[19, 20] This, therefore, leads to severe loss of Zn during the film deposition. Adding extra Zn into the target is an effective way to compensate the severe loss of Zn in heteroepitaxial growth of zinc spinel oxide thin films by PLD.[20]

In this work, a homogeneous bulk target for PLD was fabricated through a two-step sintering process: a pressed pellet of mixture of 25 wt. % GeO_2 (purity 99.999 %,

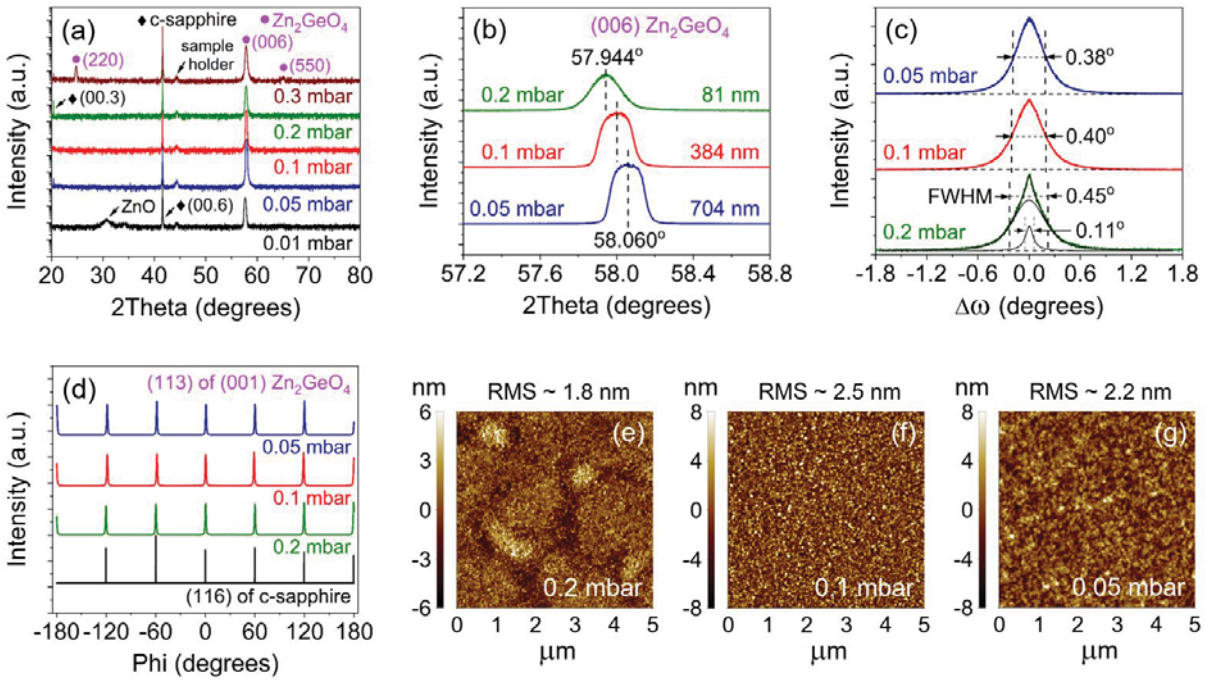

Figure 2.11: (a) XRD patterns of thin films deposited at 800 °C under different O_2 pressures. **(b)** Selected (006) peaks of XRD, and **(c)** rocking curves of (006) peak of the thin films deposited at different O_2 pressures of 0.05, 0.1 and 0.2 mbar. **(d)** Phi scans of (113) and (116) for the (001)-oriented thin films and the *c*-sapphire substrates, respectively. AFM surface morphologies of the films deposited at different O_2 pressures of **(e)** 0.2 mbar, **(f)** 0.1 mbar, and **(g)** 0.05 mbar.

ChemPUR) and 75 wt. % ZnO (purity 99.99 %, Alfa Aesar) raw powders was firstly sintered at 1100°C for 12 hours, the resulting pellet was crushed and grinded into fine powders for the sintering at 1300°C for 12 hours to obtain the PLD target. The atomic ratio of Zn: Ge is approximately 4:1 for the target, which is much greater than the stoichiometric ratio of 2:1 for Zn_2GeO_4. The extra Zn in target is to compensate the severe loss of volatile Zn during the thin-film growth at high temperatures. A 248 nm KrF excimer laser was used for PLD with a 5 Hz repetition of laser pulses. The laser fluence on target surface is about 5 J/cm^2, the deposition time is 1 hour (18000 pulses) and the setting temperature is about 800 °C for the film growth. The O_2 partial pressure was changed from 0.01 to 0.3 mbar to study the effect of O_2 pressure on microstructure and optical properties of the thin films.

Figure 2.11(a) shows the XRD patterns of the films deposited at different O_2 pressures of 0.01, 0.05, 0.1, 0.2 and 0.3 mbar. The 2θ-ω scans were aligned with calibration using (00.6) α-Al_2O_3 reflection at 41.700° (c=12.980 Å). It is clearly observed that the films deposited at 0.05, 0.1 and 0.2 mbar O_2 pressure exhibit only one peak corresponding to (006) reflection of rhombohedral spinel Zn_2GeO_4, suggesting that a moderate O_2 pressure range from 0.05 to 0.2 mbar is suitable for the growth of phase-pure (001)-oriented Zn_2GeO_4 thin films. The thickness of films is determined by generalized ellipsometry approach using a B-spline anisotropic fitting mode. The evaluated film thickness is about 81, 384 and 704 nm for the films deposited at 0.05, 0.1 and 0.2 mbar O_2 pressure, respectively. Apparently, the higher O_2 pressure significantly decreases the deposition rate of (001)-oriented Zn_2GeO_4 thin films, and thus leads to the remarkably thinner

film. In addition, the thickness of film deposited at 0.2 mbar is also measured by x-ray reflectivity (XRR), and evaluated to be about 79 nm, which is in very good agreement with the thickness value measured by ellipsometry. Figure 2.11(b) shows the selected (006) reflexes of XRD patterns of the films deposited at 0.05, 0.1 and 0.2 mbar O_2 pressure. A slight shift to smaller angles for the (006) peak is observed as O_2 pressure increases while film thickness decreases. The calculated *c*-lattice constant of the 81 nm and 704 nm thick films deposited at 0.2 and 0.05 mbar, according to the 2θ values of 57.944° and 58.060° for the (006) Zn_2GeO_4 reflection, is approximately 9.542 Å and 9.524 Å, respectively. These results are in line with the experimental value range from 9.507 Å (powder) to 9.547 Å (single crystal),[16, 21] indicating no significant strain present in the films. It was found that a higher O_2 pressure could effectively decrease the loss of Zn in high-temperature growth of zinc spinel oxide thin films by PLD,[22] while the interstitial Zn preferentially forms due to the open structure of rhombohedral Zn_2GeO_4 when excess Zn exists.[23, 24] The slightly increased *c*-lattice constant of films with increasing O_2 pressure, may be resulted from the possible introduction of interstitial Zn into the crystal lattice of films as excess Zn species exist in the plasma ablated from the Zn-rich target.

Figure 2.11(c) shows the rocking curve of (006) peak of the films deposited at different O_2 pressures of 0.05, 0.1 and 0.2 mbar. The fitting result of rocking curve of the film deposited at 0.2 mbar, indicates an obviously two-layered structure of the thin film,[25–27] consisting of a strained bottom layer with a full width at half maximum (FWHM) of about 0.11° and a strain-relaxed top layer with a FWHM of about 0.45°. While the FWHM of rocking curve of (006) Zn_2GeO_4 peak is about 0.40° and 0.38° for the films deposited at 0.1 and 0.05 mbar, respectively, suggesting a good crystalline quality of the films. The phi scan was performed to determine the in-plane orientation relationship between rhombohedral (001)-oriented Zn_2GeO_4 thin films and *c*-sapphire substrates. As shown in Figure 2.11(d), six peaks with 60-degree intervals of the Zn_2GeO_4 thin films are aligned with respect to the six peaks of the *c*-sapphire substrate, confirming an in-plane epitaxial matching between the (001) crystal plane of Zn_2GeO_4 thin films and the (00.1) crystal plane of *c*-sapphire substrate. The in-plane orientation relationships are identified to be [100] Zn_2GeO_4// [10.0] Al_2O_3 and [110] Zn_2GeO_4// [11.0] Al_2O_3. The AFM surface morphologies of epitaxial (001) Zn_2GeO_4 thin films deposited at different O_2 pressures are shown in Figure 2.11(e-f). Even though the difference in film thickness is huge, the surface roughness is similar for the films. The RMS roughness of the 81 nm, 384 nm and 704 nm thick epitaxial thin films is about 1.8 nm, 2.5 nm and 2.2 nm, respectively, indicating a smooth surface for the high-quality epitaxial thin films.

Figure 2.12 illustrates the atomic-scale schemes of (001) Zn_2GeO_4 and (00.1) α-Al_2O_3 (*c*-sapphire) crystal planes for in-plane atomic lattice matching. Considering the formation of chemical bonds between Zn and Ge atoms of (001) Zn_2GeO_4 plane and O atoms of (00.1) α-Al_2O_3 plane, the maximum distance between nearest O atoms on (00.1) α-Al_2O_3 plane is about 0.286 nm, which is about 12~16 % smaller than the minimum Zn-Ge (0.320 and 0.328 nm) and Ge-Ge (0.331 nm) distances on the (001) Zn_2GeO_4 plane. In the case of the present study, an apparent compressive strain forms in the initial bottom part of the layer of (001)-oriented Zn_2GeO_4 epitaxial thin film due to the large lattice mismatch greater than 10 %. The strain gradually relaxes with increasing film thickness over a critical point, and a top relaxed layer consequently forms above the critical thickness with a large number of lattice defects. This is in good agreement

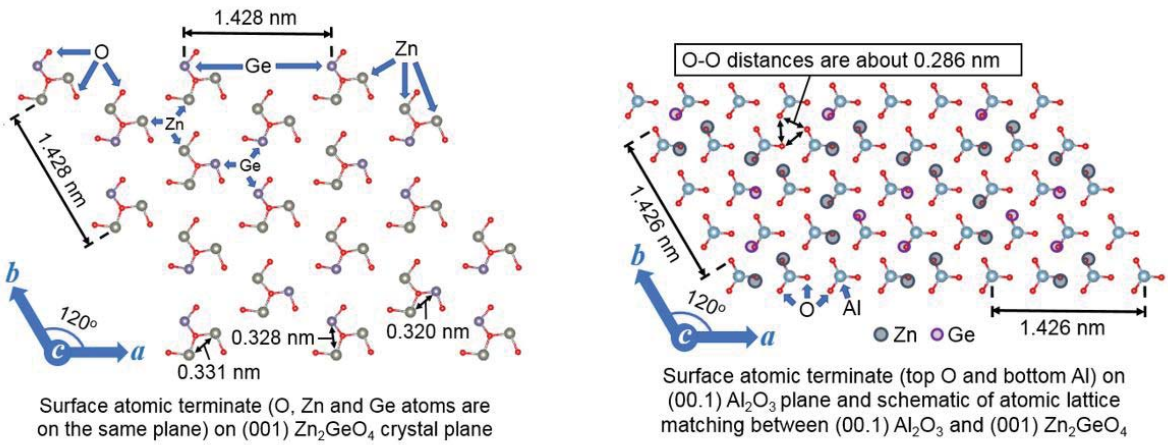

Figure 2.12: Schematic of atomic scale in-plane lattice matching relationship between (001) Zn_2GeO_4 and (00.1) α-Al_2O_3 crystal planes. Crystallographic data of crystal planes and surface atomic terminations of rhombohedral (001) Zn_2GeO_4 and hexagonal (00.1) α-Al_2O_3 are from Cambridge Structure Database (CSD).[15, 16] Atomic-scale structures are visualized using VESTA software.[28]

with the fitting result of rocking curve of the 81 nm thick epitaxial thin film deposited at 0.2 mbar O_2 pressure. A similar process was observed in the heteroepitaxial growth of hexagonal (00.1) $CuFeO_2$ thin films on *c*-sapphire substrates by PLD.[26]

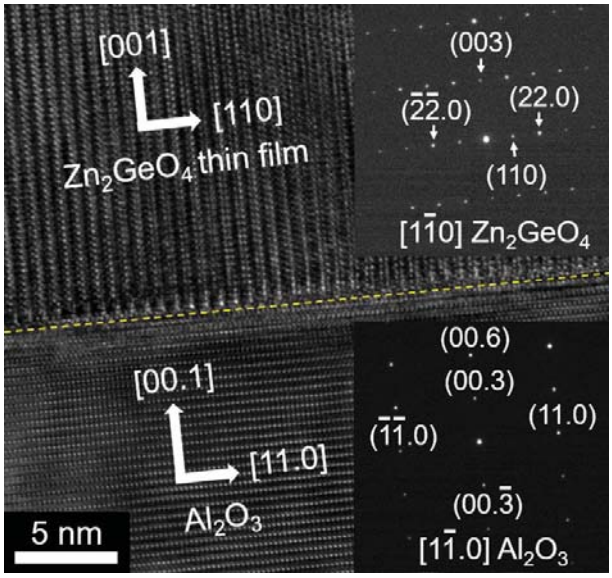

Figure 2.13: Cross-sectional HRTEM image around interface of the (001) Zn_2GeO_4 epitaxial thin film with inserted SAED patterns of the film and substrate.

The cross-sectional HRTEM image around interface between the film and the substrate, and the SAED patterns of epitaxial thin film and c-sapphire substrate are shown in Figure 2.13. The interface appears sharp, and there are no signs of secondary phases. The SAED patterns confirm that the orientation matching relationships are out-of-plane [001]Zn_2GeO_4||[00.1]Al_2O_3, and in-plane [110] Zn_2GeO_4||[11.0] Al_2O_3 and [1-10]

Zn_2GeO_4||[1-1.0] Al_2O_3.

Raman spectroscopy was carried out at room temperature under a 325 nm laser excitation to further confirm the rhombohedral spinel Zn_2GeO_4 phase of the films. From the Raman spectra shown in Figure 2.14(a), two peaks at 802 and 776 cm^{-1} are clearly observed corresponding to $A_g^{(2)}$ and $E_g^{(4)}$ modes of rhombohedral Zn_2GeO_4, respectively. This result is consistent with the experimental values of 802 and 777 cm^{-1} for Zn_2GeO_4 microrods.[29, 30] In addition, two other theoretical weak modes of rhombohedral Zn_2GeO_4, the $Ag^{(1)}$ and $E_g^{(3)}$ at about 745 and 752 cm^{-1},[29, 30] just overlap the 748 cm^{-1} mode of *c*-sapphire substrate. Furthermore, the peak of *c*-sapphire around 570 cm^{-1} is not broadening and its relative intensity does not apparently increases for the different samples, indicating no ZnO impurity detected in the films.[31] Raman analysis result verifies the pure-phase rhombohedral Zn_2GeO_4 epitaxial thin films. Figure 2.14(b) presents the room-temperature UV-visible transmission spectra of epitaxial (001) Zn_2GeO_4 thin films grown on one-sided polished *c*-sapphire substrates. The optical absorption of Zn_2GeO_4 is in the range from 250 nm to 270 nm, while the absorption band of around 270~380 nm is attributed to the band-to-band transition of defect energy levels.[32] From the Tauc plots shown as the inset in Figure 2.14(b), the evaluated direct optical bandgap of the epitaxial thin films is about 4.92 eV, which is greater than the experimental values of around 4.5~4.7 eV at room temperature for Zn_2GeO_4 nanorods, nanoribbons, and nanowires.[11, 12, 33] This bandgap value of 4.92 eV is even larger than the experimental value of 4.76 eV at low temperature of 4 K for Zn_2GeO_4 microwires by measurement of photoluminescence emission (PLE).[34] A recent DFT calculation by using the HSE06 hybrid functional with a mixing factor of 0.25 and 0.33 for stoichiometric Zn_2GeO_4 predicts bandgap values of 4.62 and 5.2 eV, respectively.[34] A mixing factor of 0.25 for HSE functional generally underestimates bandgap values of wide bandgap materials.[35] Whereas a larger mixing factor of 0.40 was tested to evaluate ZnO and produced better results.[36] The experimental bandgap value of 4.92 eV for epitaxial (001) Zn_2GeO_4 thin films should be closer to the theoretical bandgap value of Zn_2GeO_4, which may be similar or even greater than the predicted value of 5.2 eV.

Some literature reported room-temperature steady-state photoluminescence (PL) emission spectra of Zn_2GeO_4 materials under 325 nm laser excitation, but we could not observe any apparent PL signal from the Zn_2GeO_4 epitaxial thin film under excitation using a 325 nm laser. Figure 2.14(c) shows the room-temperature steady-state PL emission spectra of the epitaxial thin films under 266 nm (4.67 eV) laser excitation. A broad blue emission band is observed at around 2.62 eV (473 nm) with a FWHM of about 0.55 eV (100 nm). Apparently, it is a defect-related emission band. Figures 2.14(d-f) shows the room-temperature time-resolved PL spectra of the epitaxial thin films with different thicknesses. All three decay curves can be well fitted to double-exponential curves represented by the following bi-exponential decay function:

$$I(t) = I_{offset} + \alpha_1 e^{-\frac{t}{\tau_1}} + \alpha_2 e^{-\frac{t}{\tau_2}} \tag{2.2}$$

where I_{offset} is a constant; α_1 and α_2 are the relative weight factors; τ_1 and τ_2 are the time constants of fast and slow decay processes, respectively; t is decay time, and $I(t)$ is the luminescent intensity at t time. Then the average decay time τ is calculated by the following equation:

$$\tau = \alpha_1\tau_1 + \alpha_2\tau_2 \tag{2.3}$$

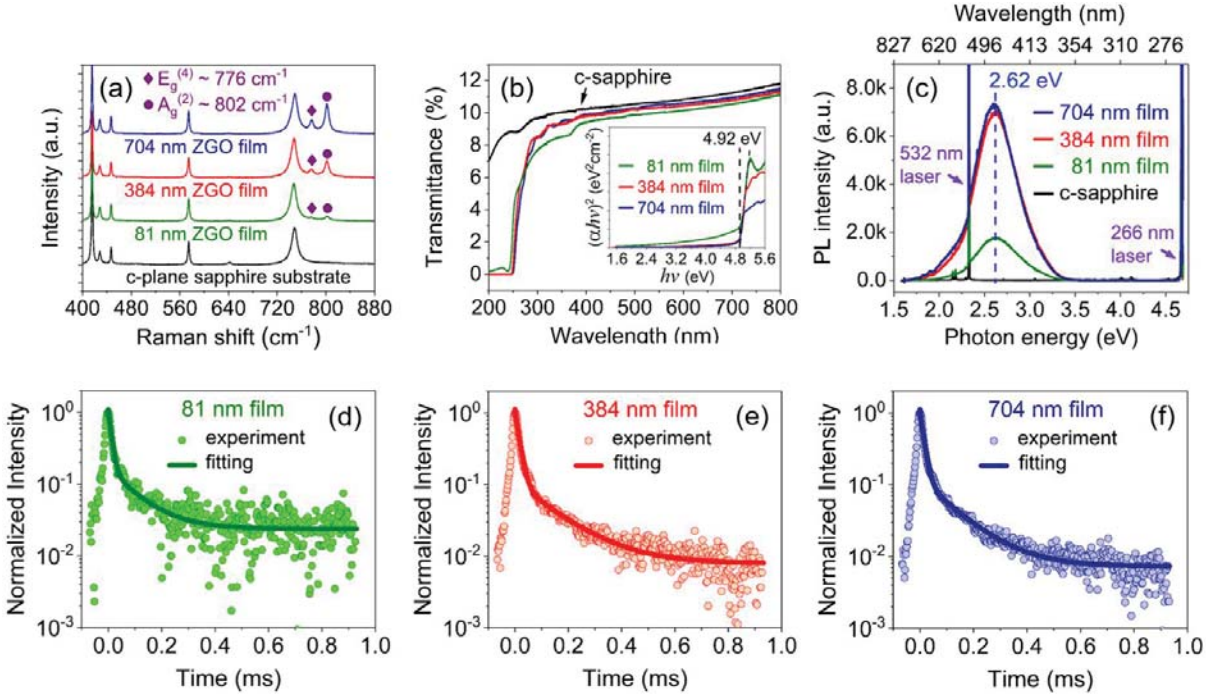

Figure 2.14: (a) Raman spectra of epitaxial (001) Zn_2GeO_4 thin films grown on *c*-sapphire substrates. **(b)** UV-visible transmission spectra of the epitaxial thin films, with an inset of Tauc plots from the transmission spectra. **(c)** Room-temperature steady-state photoluminescence (PL) spectra of the epitaxial thin films. Room-temperature time-resolved PL spectra with double-exponential curve fitting for the epitaxial thin films with different thicknesses of **(d)** 81 nm, **(e)** 384 nm, and **(f)** 704 nm.

The fitting parameters and average decay times for the three PL decay curves are shown in Table 2.1. The decay curves of films with different thicknesses show similar fitting parameters and average decay times of around 20~30 μs, suggesting a similar kinetic mechanism that the blue luminescence originates from donor-acceptor recombination process. It is well-known that rhombohedral Zn_2GeO_4 is a native defect phosphor, in which the native oxygen vacancies (plus perhaps zinc interstitials) and cationic (germanium and zinc) vacancies are related to the donors and acceptors, respectively. A similar blue band PL emission at around 2.6 eV by UV light excitation at 5.10 eV and 4.13 eV was suggested to be related to the introduction of interstitial Zn into the crystal Zn_2GeO_4 phase in the nanocrystallized $15Li_2O$–$15ZnO$–$70GeO_2$ glass.[37] The interstitial Zn was speculated to markedly affect the PL of Zn_2GeO_4 nanorods due to the lack of oxygen vacancies.[24] In the case of this study, the blue band emission peak does not apparently shift for the films deposited at different O_2 pressures, which directly correlate to the formation and concentration of oxygen vacancies in the oxide films. On the other hand, the interstitial Zn probably formed in the epitaxial thin films as previously discussed. Therefore, we speculate that the observed blue emission in (001) Zn_2GeO_4 epitaxial thin films is probably related to zinc interstitials and possible germanium vacancies, the latter may be resulted from evaporative loss at high temperature.

In summary, this study demonstrates the heteroepitaxial growth of pure-phase and high-quality rhombohedral (001) Zn_2GeO_4 thin films on *c*-sapphire substrates by PLD. The in-plane orientation relationships are identified to be in-plane [110] Zn_2GeO_4//

Table 2.1: The fitting parameters and average decay times for the epitaxial (001) Zn_2GeO_4 thin films with different thicknesses.

Film thickness	I_{offset}	α_1	τ_1 (μs)	α_2	τ_2 (μs)	τ (μs)
104 nm	0.024	0.93	11	0.13	103	23.6
450 nm	0.008	1.01	14	0.10	143	28.4
789 nm	0.007	0.99	13	0.11	122	26.3

[11.0] Al_2O_3 and [1-10] Zn_2GeO_4// [1-1.0] Al_2O_3. The FWHM of rocking curve of 380~700 nm thick films is about 0.40°. The direct optical bandgap of thin films evaluated at room temperature is about 4.92 eV. The room-temperature PL spectra of epitaxial thin films exhibit a broad defect-related blue emission band at 2.62 eV. The epitaxial thin films, deposited at different O_2 pressures and with different thicknesses, exhibit similar bi-exponential decay curves with a short lifetime of about ten microseconds and a long lifetime of about hundred microseconds. The blue luminescence may relate to the possible interstitial Zn existed in the films. This work is opening a way to the epitaxial thin films of rhombohedral Zn_2GeO_4 for fundamental research in view of potential device applications.

The authors gratefully thank Mrs. Monika Hahn and Mrs. Ulrike Teschner for the preparation of PLD target and the UV-visible transmission measurement of thin films, respectively. And authors gratefully acknowledges financial support from a funding Grant (no. 459722738) awarded by DFG, Germany.

[1] J. S. Lewis, and P. H. Holloway. J. Electrochem. Soc. **147**, 3148-3150 (2000).
[2] J. P. Bender, J. F. Wager, J. Kissick, B. L. Clark, and D. A. Keszler. J. Lumin. **99**, 311-324 (2002).
[3] L. C. Williams, D. Norton, J. Budai, and P. H. Holloway. J. Electrochem. Soc. **151**, H188-H191 (2004).
[4] K. Huang, X. Dou, Y. Zhang, X. Gao, J. Lin, J. Qu, Y. Li, P. Huang, and G. Han. Adv. Funct. Mater. **31**, 2009920 (2021).
[5] J. Li, X. Huang, X. Zhao, L-J. Chen, and X-P. Yan. Angew. Chem. Int. Ed. **60**, 2398-2405 (2021).
[6] C. Yan, N. Singh, and P. S. Lee. Appl. Phys. Lett. **96**, 053108 (2010).
[7] C. Li, Y. Bando, M. Liao, Y. Koide, and D. Golberg. Appl. Phys. Lett. **97**, 161102 (2010).
[8] X. Zhou, Q. Zhang, L. Gan, X. Li, H. Li, Y. Zhang, D. Golberg, and T. Zhai. Adv. Funct. Mater. **26**, 704-714 (2016).
[9] J. Wang, C. Yan, M-F. Lin, K. Tsukagoshi, and P. S. Lee. J. Mater. Chem. C. **3**, 596-600 (2015).
[10] C-H. Liao, C-W. Huang, J.-Y. Chen, C-H. Chiu, T. Tsai, K-C. Lu, M-Y. Lu, and W-W. Wu. J. Phys. Chem. C. **118**, 8194-8199 (2014).
[11] J. Huang, X. Wang, Y. Hou, X. Chen, L. Wu, and X. Fu. Environ. Sci. Technol. **42**, 7387-7391 (2008).
[12] Q. Liu, Y. Zhou, J. Kou, X. Chen, Z. Tian, J. Gao, S. Yan, and Z. Zou. J. Am. Chem. Soc. **132**, 14385-14387 (2010).
[13] J. Liang, J. Xu, Q. Gu, Y. Zhou, C. Huang, H. Lin, and X. Wang. J. Mater. Chem. A, **1**, 7798-7805 (2013).

[14] S. Wu, and Q. Ma. J. Alloys Comp. **567**, 40-46 (2013).
[15] E. N. Maslen, V. A. Streltsov, N. R. Streltsova, N. Ishizawa, and Y. Satow. Acta Cryst. **B49**, 973-980 (1993).
[16] A. Oribe, K. Tanaka, H. Morikawa, F. Marumo. Report of the Research Laboratory of Engineering Materials, Tokyo Institute of Technology 12, 7-12 (1987).
[17] J. Narayan, and B. C. Larson. J. Appl. Phys. **93**, 278-285 (2003).
[18] C. B. Alcock, V. P. Itkin, and M. K. Horrigan. Can. Metall. Q. **23**, 309 (1984).
[19] D. E. Clemmer, N. F. Dalleska, and P. B. Armentrout. J. Chem. Phys. **95**, 7263 (1991).
[20] S. Luo, G. F. Harrington, K.-T. Wu, and T. Lippert. Phys. Status Solidi RRL **14**, 2000270 (2020).
[21] S-W. Yang, F. Peng, W-T. Li, Q-W. Hu, X-Z. Yan, L. Lei, X-D. Li, and D-W. He. Chin. Phys. B **25**, 076101 (2016).
[22] Y. E. Lee, D. P. Norton, C. Park, and C. M. Rouleau. J. Appl. Phys. **89**, 1653-1656 (2001).
[23] Z. Liu, X. Jing, and L. Wang. J. Electrochem. Soc. **154**, H500-H506 (2007).
[24] S. Wu, Z. Wang, X. Ouyang, and Z. Lin. Nanoscale, **5**, 12335-12341 (2013).
[25] T. Joshi, T. R. Senty, R. Trappen, J. Zhou, S. Chen, P. Ferrari, P. Borisov, X. Song, M. B. Holcomb, A. D. Bristow, A. L. Cabrera, and D. Lederman. J. Appl. Phys. **117**, 013908 (2015).
[26] S. Luo, A. Fluri, S. Zhang, X. Liu, M. DÃ¶beli, G. F. Harrington, R. Tu, D. Pergolesi, T. Ishihara, and T. Lippert. J. Appl. Phys. **127**, 065301 (2020).
[27] T-B. Hur, Y-H. Hwang, H-K. Kim, and H-L. Park. J. Appl. Phys. **96**, 1740-1742 (2004).
[28] K. Momma, and F. Izumi. J. Appl. Cryst. **44**, 1272-1276 (2011).
[29] P. Hidalgo, A. Lopez, B. Mendez, and J. Piqueras. Acta Mater. **104**, 84-90 (2016).
[30] J. Dolado, P. Hidalgo, and B. Méndez. Phys. Status Solidi A **215**, 1800270 (2018).
[31] K. A. Alim, V. A. Fonoberov, M. Shamsa, and A. A. Balandin. J. Appl. Phys. **97**, 124313 (2005).
[32] F. Chi, X. Wei, B. Jiang, Y. Chen, C. Duan, and M. Yin. Dalton Trans. **47**, 1303-1311 (2018).
[33] L-C. Tien, F-M. Yang, S-C. Huang, Z-X. Fan, and R-S. Chen. J. Appl. Phys. **124**, 174503 (2018).
[34] J. Dolado, R. Martínez-Casado, P. Hidalgo, R. Gutierrez, A. Dianat, G. Cuniberti, F. Domínguez-Adame, E. Díaz, and B. Méndez. Acta Mater. **196**, 626-634 (2020).
[35] A. J. Garza, and G. E. Scuseria. J. Phys. Chem. Lett. **7**, 4165-4170 (2016).
[36] S. J. Clark, J. Robertson, S. Lany, and A. Zunger. Phys. Rev. B **81**, 115311 (2010).
[37] Y. Takahashi, M. Ando, K. Iwasaki, H. Masai, and T. Fujiwara. Appl. Phys. Lett. **97**, 071906 (2010).

2.11 Advances in Pulsed Laser Deposition of Copper Iodide-based Thin Film Heterostructures

P. Storm, M. Bar, S. Selle*, M. Grundmann, M. Lorenz

*Fraunhofer-Institut für Mikrostruktur von Werkstoffen und Systemen (IMWS), Halle

Within the DFG-funded Research Group FOR 2857, we are dealing in project P01 with pulsed laser deposition (PLD) of CuI-based thin film heterostructures. Due to the long-term experience with PLD and the given lab infrastructure [1], we could establish the CuI film growth in a satisfying fashion surprisingly fast [2], see also our previous Semiconductor Physics Group report 2020. A unique advantage of the film growth by PLD is the high flexibility to explore doping by simply mixing the dopant into the PLD source target. Figure 2.15 shows a selection of CuI-based PLD targets with various dopant elements as indicated. The targets were prepared and used in the current funding period of FOR 2857.

Figure 2.15: Selection of one-inch diameter CuI-based PLD targets doped with the following elements or compounds: top row from left: CuO, CuTe, CuSe, Zn, MgI_2; bottom row: Sn, SnI_4, CuS, CuO, RbI. Most of the targets are elliptically segmented with different outer ("A:" on target box) and inner ("I:") phase to allow a control of the dopant concentration in the grown film by the radial laser focus position on the target, as presented for example in [3]. Targets prepared by P. Storm and M. Hahn, photo by M. Lorenz.

Oxygen (like all oxychalcogenides) is expected to act as an acceptor in CuI [4], and the unintentional incorporation of oxygen from the atmosphere into CuI could influence the electrical properties in particular for the CuI films without top capping layer. However, there is still some discussion if for example also adsorption of water enhances the electrical conductivity of CuI. We performed investigations on the time-dependent electrical behavior of PLD grown CuI in dependence on growth parameters of the Al_2O_3 capping layer and of the CuI film itself [4].

Figure 2.16 (a) shows the remarkable impact of growth parameters of the in-situ Al_2O_3 capping layers on the resistivity of PLD CuI thin films [4]. Growing the capping in oxygen (blue) increases the acceptor concentration by orders of magnitude in relation to growth in nitrogen (green), which is most probably due to the diffusion of excess oxygen from the capping into the CuI film. The CuI film without any capping layer (red) shows an immediate and even stronger decrease of conductivity. Figure 2.16 (b) shows the long-term diffusion dynamic of oxygen through the Al_2O_3 capping layer with an oscillation period of about one day. These surprising oscillations are most probably induced by the minor day-night temperature variations in our unregulated lab environment [4].

As PLD has nearly no limitation concerning the source target material [1], Figure 2.17 (a) demonstrates single crystalline CuI films, i.e. with only one rotation domain, grown in-situ on $SrF_2(111)$ substrates with a NaBr template layer with good lattice match. Due to the high water solubility of NaBr, free-standing μm-thin CuI with high

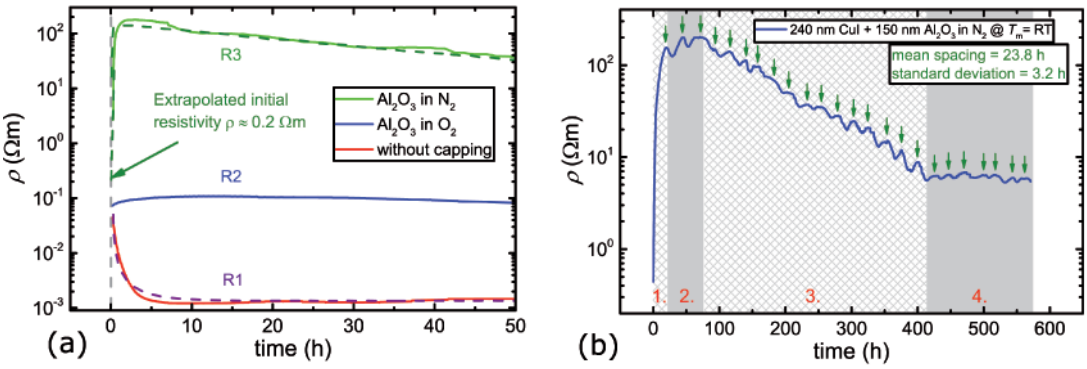

Figure 2.16: (a) Impact of growth atmosphere during the Al_2O_3 capping deposition on the time evolution of resistivity of 120 nm CuI thin films as indicated. Dashed lines represent the simulated behavior [4]. Measurements were done in air at 50°C in darkness. (b) Long-term degradation of resistivity of an $Al_2O_3(N_2)$ / CuI heterostructure in an unregulated lab environment, i.e. at given room temperature. Green arrows point to the oscillation maxima with a period of about 24 hours. The diffusion regimes 1 to 4 (indicated by gray-levels) are explained in [4]. Figure is taken from [4].

crystalline quality could easily be prepared that way, see Figure 2.17 (b) and Refs. [5] and [6].

In summary, considerable progress could be obtained in CuI film growth by PLD, as summarized by the points below. A main technical advantage of the CuI PLD growth is that no extra source of the highly corrosive iodine vapour is required.

- Optimized PLD process: (a) epitaxial growth with enhanced crystallinity for increasing growth temperature Tg, (b) smooth film surfaces (rrms < 1 nm) for decreasing Tg, (c) tunable electrical properties of p ≈ 5×10^{16} cm^{-3} with a hole mobility of μ = 20 cm^2/Vs up to p ≈ 10^{19} cm^{-3} with μ = 8 cm^2/Vs [2]. (d) In-situ capping for stable carrier density [2].

- Origin of free carriers and p-doping of PLD CuI further clarified: (e) conductivity in Cu-rich PLD CuI is due to oxygen doping [4], (f) p-doping demonstrated with CuI:Se [3]. Also, the whole mixing range from CuI via Cu(BrI) to CuBr was presented, as reported in another contribution.

- Suppression of rotational domains, volume crystals and epitaxial lift-off: (g) single crystalline, free-standing CuI realized with NaBr template layers [5], (h) epitaxial lift-off successfully demonstrated [6], (i) preliminary limits for volume crystals were determined [5] and [6].

[1] M. Lorenz, Wiley-VCH Verlag GmbH & Co. KGaA (2019), doi:10.1002/3527600434.eap810
[2] P. Storm, M. S. Bar, G. Benndorf, S. Selle, C. Yang, H. von Wenckstern, M. Grundmann, M. Lorenz, APL Mater. **8**, 091115 (2020); see also Aili McConnon, AIP Scilight 391103-1 (2020)
[3] P. Storm, M. S. Bar, S. Selle, H. von Wenckstern, M. Grundmann, M. Lorenz, Phys. Status Solidi RRL 2021, 2100214 (2021)

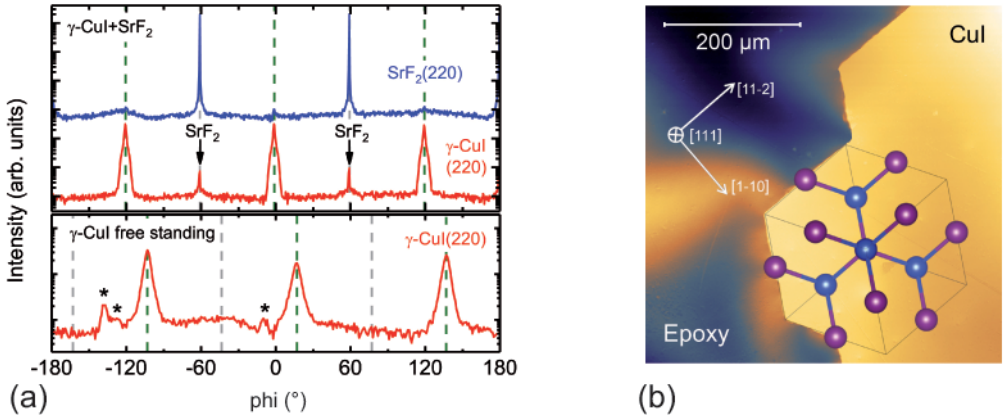

Figure 2.17: (a) XRD-φ-scans of (top) CuI / NaBr films on SrF_2(111) and (bottom) 2 μm thin, free-standing CuI glued to glass with epoxy resin. Artifacts originating from broken off crystals during separation from the substrate are marked with asteriks. (b) Laser scanning microscope top view of the edge of a free standing 2 μm CuI film (lift-off from CuI/NaBr/SrF_2) with representation of the (111) out-of-plane oriented unit cell of copper iodide. Figures are taken from [5].

[4] P. Storm, S. Gierth, S. Selle, M. S. Bar, H. von Wenckstern, M. Grundmann, M. Lorenz, APL Mater. **9**, 051101 (2021)
[5] P. Storm, K. Karimova, M. S. Bar, S. Selle, H. von Wenckstern, M. Grundmann, M. Lorenz, ACS Applied Materials & Interfaces (2022), accepted for publication
[6] P. Storm, S. Selle, H. von Wenckstern, M. Grundmann, M. Lorenz, Journal of Materials Chemistry C, Communication, (2022), accepted for publication

2.12 Optical Properties of CuI

Wide-bandgap semiconductors show promising properties regarding higher operation voltages, frequencies and temperatures for devices, while additionally their transparency enables further applications. While many wide-bandgap n-type materials are available nowadays, suitable intrinsic p-type materials are still missing. A possible p-type candidate is CuI [1]. Its intrinsic p-type conductivity in conjunction with its high hole mobility and transparency in the visible spectral range and a high exciton binding energy make CuI a promising material for future optoelectronic applications.

2.12.1 Dynamics of exciton-polariton emission

E. Krüger, M.S. Bar, S. Blaurock*, L. Trefflich, R. Hildebrandt, A. Müller, O. Herrfurth†, G. Benndorf, H.von. Wenckstern, H. Krautscheid*, M. Grundmann, C. Sturm

*Institut für Anorganische Chemie, Universität Leipzig, Johannisallee 29, 04103 Leipzig
†now at: Active Fiber Systems GmbH, Ernst-Ruska-Ring 17, 07745 Jena

We investigated static and dynamic aspects of recombination of exciton-polaritons in CuI as a function of temperature in the range of (10 – 250) K [2]. For this purpose,

CuI single crystals were grown in autoclaves filled with copper iodide-acetonitrile solution saturated at room temperature and penta-2,3-dione in a 10:1 ratio. A typical photoluminescence (PL) spectrum is shown in Fig. 2.18(a). The emission lines between 3.055 eV and 3.12 eV, previously incorrectly assigned to the transverse and longitudinal excitons[3, 4], can be attributed to the coupling of the Γ_5 singlet and $\Gamma_{3,4}$ triplet exciton states to the photons. The calculated dispersion of the corresponding bulk polariton branches (see inset in Fig. 2.18(a)) agrees very well with our experimental data. The observed emission peaks at lower energies between 2.98 eV and 3.05 eV at 10 K have been attributed to bound excitons. In particular, the emission in the energy range of the C-E lines (cf. Fig. 2.18(a)) is considered to be due to recombination of excitons bound to flat neutral acceptors. The activation energy of the electrically active flat acceptors measured on similar single crystals was determined from tempearture-dependent van der Pauw measurements to be E =108 meV. Assuming that the acceptors contribute to the free carrier density as well as to the previously mentioned emission peaks of the bound excitons, we roughly estimate the Haynes rule factor, which describes the ratio of the binding energy of the exciton to the impurity E_B to the binding energy of the hole to the impurity, to a value of 0.08-0.17. Furthermore, the decay times of the bound excitons were found to follow the $E_B^{3/2}$ rule[5] (see Fig. 2.18(b)), indicating that recombination is dominated mainly by radiative recombination processes.

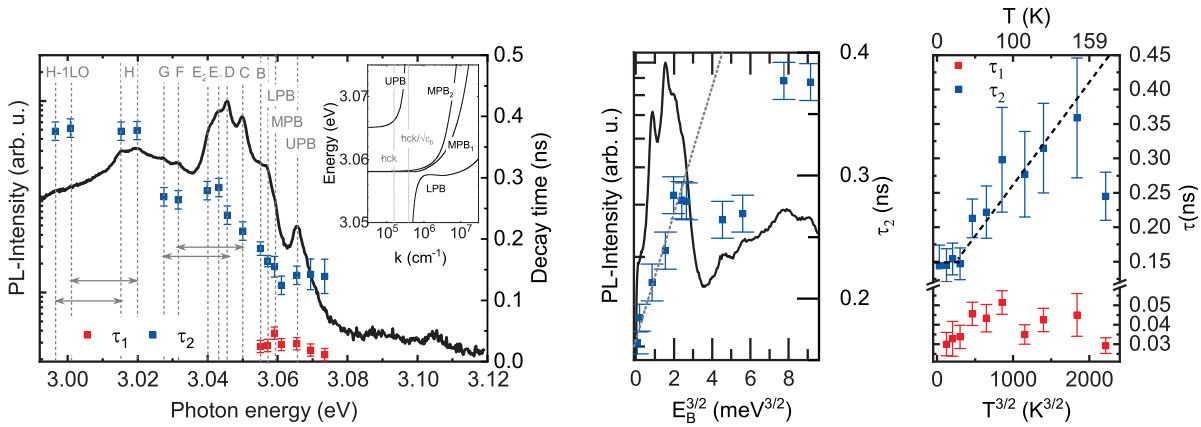

Figure 2.18: (a) Typical time-integrated micro-PL spectra ($D_{\text{exc}} \approx 6$ nJ/cm^2) of a CuI single crystal at 10 K obtained from a streak camera image. The energy positions of the free exciton-polariton and bound exciton transitions, labeled with (LPB, MPB, UPB) and (C-H), respectively are indicated by vertical dashed lines. Gray horizontal arrows visualize the LO-phonon energy of approximately 19 meV. Red and blue symbols represent the different decay time components τ_1 and τ_2 obtained for the corresponding transitions. The inset shows the calculated polariton-dispersion curves (without damping). Dotted vertical lines visualize the photon dispersion in vacuum (hck) and in CuI ($hck/\sqrt{\varepsilon_B}$) respectively. (b) Decay times of bound exciton transitions in dependence on $E_B^{3/2}$. The gray dashed line highlight the observed proportionality for the transitions C-E$_{1,2}$. (c) Fast and slow decay components τ_1 and τ_2 of the UPB emission as a function of temperature. The gray dashed line serves as an eye guide to highlight the $\tau_2 \propto T^{3/2}$ proportionality for temperatures below 160 K. Adapted from Ref. [2]

As the lattice temperature increases, the emission profile shifts to lower energies due to bandgap renormalization processes. Typically, changes in bandgap energy can be attributed to the electron-phonon interaction and thermal lattice expansion via the

deformation potential. Although the latter contribution can be neglected for many materials, it leads to nonphysical results in the case of CuI. Therefore, we consider the bulk thermal expansion and the electron-phonon interaction individually, obtaining an effective phonon energy of about 20 meV, which agrees well with the experimental values for the LO phonon energy determined by Raman spectroscopy. However, we note that effective temperature determining the thermal polariton distribiution along the UPB may exceed the crystal temperature after an optical excitation. The corresponding temperature evolution can be described by a simple exponential cooling with a cooling constant of approximately 20 ps, which was determined based on line-shape analysis of the high-energy tail of the transient UPB emission. Moreover, the observed polariton temperature was found to exceed the nominal lattice temperature even 100 ps after optical excitation. We explain this overheating by the depletion of the polariton population in the radiation region with wavevectors $k_{\|} \leq k_{\mathrm{vac}}$, which prevents complete thermalization of the entire polariton population.

For the recombination of free polaritons and bound states we find a different transient behavior: the decay of the free polariton emission shows a non-monoexponential decay, which can be described by a sum of two exponential decays, while the transient behavior of the bound exciton emission can be well described by a monoexponential decay. The corresponding decay times τ_1 and τ_2 are shown in Fig. 2.18 (a). We assign the fast decay component with decay times τ_1 between 10 ps and 40 ps observed for the free polariton emission peaks to the trapping of polaritons be defects due to their strong excitonic like character. The slow decay component with decay times τ_2 in the range of (145 – 165) ps at 10 K is assumed to represent the intrinsic radiative decay of the free polaritons. Due to a significant overlap of the LPB and MPB emission peaks at elevated temperatures, we focused on the decay dynamics of the UPB emission as a function of temperature (see Fig. 2.18 (c)). We find that the slow decay component τ_2 increases with increasing temperatures up to approximately 350 ps at 160 K, following $\tau_2 \propto T^{3/2}$ as expected for the radiative decay of free excitons in bulk material [6]. Such increase can be explained by the conservation of the in-plane wave vector component $k_{\|}$ at the crystal surface, since polariton states at higher k-vectors, which are populated at higher temperatures, cannot be transmitted through the crystal surface. For temperatures above 160 K the decay time start to decrease again, probably due to an increasing impact of non-radiative recombination channels. Finally, we note that the decay time remains constant at temperatures below 45 K revealing an unchanged polariton distribution at low temperatures, which is in good agreement with the fact that no thermal equilibrium of the polarriton distribution is not achieved in this case. In contrast to τ_2, the fast decay time τ_1 is almost independent on the temperature, such that we attribute this decay channel to non-radiative decay process, as e.g. trapping by defects. This interpretation is also supported by the fact that the obtained PL rise times of bound exciton emission are around 30 ps and thus comparable to τ_1. Based on this interpretation we estimate the defect density in the investigated CuI crystal to a value in the order of $2 \times 10^{17}\,\mathrm{cm}^{-3}$, which is in reasonable agreement with measured hole density at room temperature.

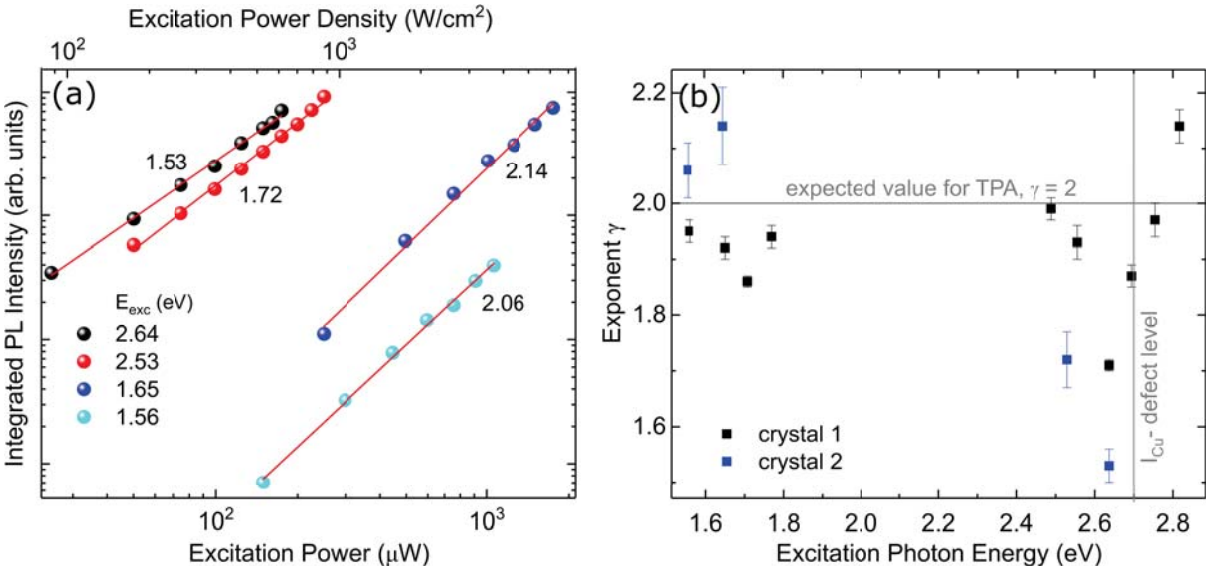

Figure 2.19: (a) Integrated PL intensity as a function of the excitation power for different excitation energies E_{exc} (coloured circles). The values of the slopes resulting of the linear fit are indicated. (b) Exponent γ versus the excitation photon energy for two crystals (coloured squares).

2.12.2 Two-photon absorption induced Photoluminescence

A. Müller, L. Trefflich, E. Krüger, S. Blaurock *, H. Krautscheid *, M. Grundmann, C. Sturm

*Universtät Leipzig, Institute of Inorganic Chemistry, Johannisallee 29, 04103 Leipzig.

We have investigated the emission spectra by means of two photon absorption (TPA). The integrated PL intensity as a function of the excitation power E_{exc} is shown in Fig. 2.19a for selected energies of the excitation. We observed for all excitation energies an excitation power dependent power law, namely $I \propto P^{\gamma(E_{\mathrm{exc}})}$. The determined exponent γ as a function of the excitation energy is shown in Fig. 2.19b for two crystals. For small excitation energies, i.e., $E < 2$ eV the magnitude of the exponent γ of about 2 is obtained, which is expected for an excitation via a virtual state [12]. However, for an excitation energy of about $E = 2.64$ eV the exponent γ exhibit a minimum of about 1.5, which can be attributed to an excitation via a real state within the band gap. This is support by density functional theory calculation performed by Koyasu *et al.* [13]. According to their calculations, an anti-site defect at 2.7 eV is expected. We want to note, they had to use an off-center model [13–16] by reducing the symmetry from P-43m to P1 to permit the movement of the substituted iodine ion. By using this off-center model, the calculated defect generation energy is about 1 eV, implying that the I_{Cu}-off center model is a plausible explanation for the observations in our current studies.

We also investigated the impact of the self absorption on the emission spectrum. In Fig. 2.20(a) the PL spectrum by single photon absorption (SPA), i.e., by using an excitation energy above the band gap energy, as well as by TPA for a CuI bulk single crystal measured at 300 K is shown. We observe a red-shifted of the TPA-PL spectrum with respect to the SPA-PL spectrum. As the penetration depth of the exciting laser

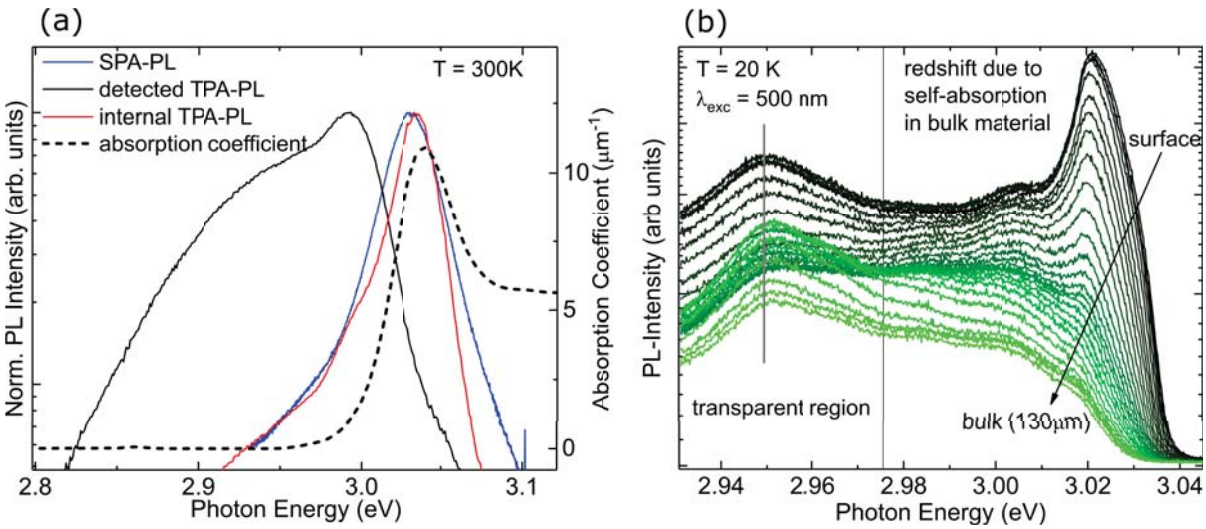

Figure 2.20: (a) SPA- and TPA-PL spectra (solid lines) measured at 300 K and the absorption coefficient. (b) TPA-PL spectra for different depth of the focal point measured at 20 K, respectively.

in the case of the SPA-PL is about 100 nm, the generated electron-hole-pairs are very close to the surface and the emitted photons can easily escape out of the crystal. In contrast to that, CuI is transparent in the case of the TPA-PL, which means that the excitation and thus the generation of the photons takes place in the entire crystal. Due to the absorption coefficient of CuI, most of the high energy photons with $E > 3.1$ eV will be absorbed before they can reach the surface, which can explain the observed the red shift in the case of the TPA-PL. For a further investigation, we perform TPA-PL at different focal points within the sample. Figure 2.20b and c shows the TPA-PL spectra for different focal point depths at 20 K, respectively. A red shift of the near band gap emission is clearly visible. For $T = 20$ K, the PL spectrum exhibit an additional peak at 2.95 eV. In contrast to the peak at an energy of about 3.02 eV, the energy of this peak is independent on the focal point. This can be attributed to the fact that the absorption coefficient in this energy range is almost zero and supports the assumption that that the observed red shift is a consequence of self absorption.

In order to describe the measured spectra $PL_{detected}$, we applied an approach which takes into account the internal TPA-PL (PL_{int}) at the focal point, the absorption coefficient α, the propagation of emitted photons within the crystal, multiple (j) internal reflections at the interfaces and a carrier density shape $n(z) \propto 1/w(z)^4$ caused by the irradiance of a Gaussian beam in two dimensions [17, 18]. Within this model, we assume that the PL is generated in a certain depth z' within the crystal. The photons will then travel to the front and to the back interface and will be reflected at the front and backside with a probability r_f and r_b, respectively. The corresponding emitted PL is

then given by [17]

$$PL_{detected}(E) = PL_{direct}(E) + PL_{filtered}(E) \tag{2.4a}$$

$$PL_{direct}(E) = \int_0^L PL_{int}(E) \cdot n(z)^2 \cdot (1 - r_f) \cdot \exp\left(-\alpha(E) \cdot z\right)\, dz \tag{2.4b}$$

$$PL_{filtered}(E) = \int_0^L \sum_{j=1} PL_{int}(E) \cdot n(z)^2 \cdot (1 - r_f) \cdot (A_j + B_j)\, dz \tag{2.4c}$$

with

$$A_j = r_f^j \cdot r_b^j \cdot \exp\left[-\alpha(E) \cdot (2jL + z)\right] \tag{2.5a}$$

$$B_j = r_f^{j-1} \cdot r_b^j \cdot \exp\left[-\alpha(E) \cdot ((2j-1)L + (L - z))\right] . \tag{2.5b}$$

PL_{direct} and $PL_{filtered}$ represents the PL which escapes directly out of the crystal and is detected after multiple internal reflections, respectively. By means of this approach the internal PL was determined, which is quite similar to those obtained from SPA-PL.

2.12.3 Exiton mediated resonant Raman scattering

R. Hildebrandt, E. Krüger, S. Blaurock*, H. Krautscheid*, C. Sturm, M. Grundmann

*Institut für Anorganische Chemie, Universität Leipzig, Johannisallee 29, 04103 Leipzig

By Raman scattering, nondestructive characterization of CuI for various structural and electric properties is enabled via optical scattering. This process involves electronic transitions and is strongly enhanced at resonance conditions. This is the case for a 325 nm excitation, i.e., with an energy close to the conduction-band-split-off-valence-band exciton. Here the laser energy is about 100 meV above the exciton ground state and this way the exciton mediates as outgoing resonance via the emission of multiple LO phonons, the so-called overtones [20] (cascade model). For (111) oriented zinc blende crystals, the cross polarization reveals a photo luminescence (PL) signal from the exciton ground state ($n = 1$) and its first excited state ($n = 2$). Takinfg a closer look reveal at the high energy of the n-th LO overtones, side modes are located at about 3 meV and 6 meV. Those are possibly related to one additional phonon scattering processes with acoustic phonons. All these processes are depicted in Fig. 2.21.

[1] M. Grundmann, et al.: Physica Status Solidi A **210**, 1671 (2013).
[2] E. Krüger, et al.: APL Materials **9**, 121102 (2021). doi:10.1063/5.0066176
[3] J. Serrano, et al.: Phys. Rev. B **65**, 125110 (2001). doi:10.1103/PhysRevB.65.125110
[4] M. Wille, et al.: Appl. Phys. Lett. **111**, 031105 (2017). doi:10.1063/1.4990524
[5] E. Rashba, G. E. Gurgenishvili: Soviet Physics - Solid State **4**, 759 (1962).
[6] Claus F. Klingshirn: *Semiconductor optics*, Springer Science & Business Media (2012).
[7] D. Chen, et al.: Crystal Growth & Design **10**, 2057 (2010).
[8] J. A. Christians, et al.: Journal of the American Chemical Society **136**, 758 (2014).
[9] F.-L. Schein, et al.: Applied Physics Letters **102**, 092109 (2013).
[10] C. Yang, et al.: Nature Scientific Reports **6**, 21937 (2016).

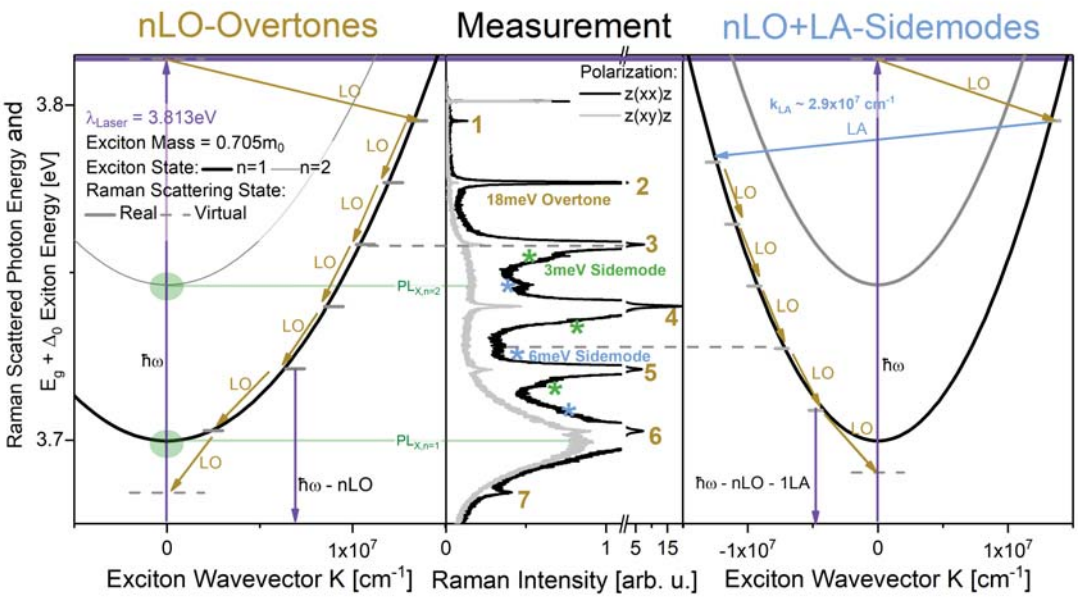

Figure 2.21: (a) Resonant Raman spectra (middle panel) of CuI for Bulk crystal 11K excited with a 325 nm. The observed nLO-Overtones (middle, orange numbers) are result of multiple relaxation of excitonic states with LO phonons (left). In the cross polarization (dark green line in the middle) the PL signal of recombining excitons of the ground state ($n = 1$) and the first excited state ($n = 2$) can be observed. Weak side modes (green and light blue asterisk in middle) observed about 3 meV and 6 meV above each nLO overtone are related to one additional scattering of LA or TA phonons with wavevector conservation (left, only for LA shown).

[11] S. Nikitine: Philosophical Magazine **4**, 1 (1959).
[12] S. L. Chen et al.: Applied Physics B **108**, 919 (2012).
[13] S. Koyasu et al.: Journal of Applied Physics **125**, 115101 (2019).
[14] G. Brunet et al.: Solid State Communications **53**, 607 (1985).
[15] R. T. Williams et al.: Physical Review B **33**, 7232 (1986).
[16] H. N. Hersh: Physical Review **148**, 928 (1966).
[17] K. Schötz et al.: Journal of Material Chemistry C **8**, 2289 (2020).
[18] M. Wiehe et al.: IEEE Transactions on Nuclear Science **68**, 220 (2021).
[19] Z. Vardeny *et al.* Phys. Rev. B **18**, 8 (1978). DOI: 10.1103/PhysRevB.18.4487
[20] R.C. Leite *et al.* Phys. Rev. Lett. **22**, 15 (1969). DOI: 10.1103/PhysRevLett.22.780

2.13 Dielectric function of $CuBr_xI_{1-x}$ alloy thin films

E. Krüger, M. Seifert*, M.S. Bar, S. Merker†, H.von. Wenckstern, H. Krautscheid†, S. Botti*, M. Grundmann, C. Sturm

*Institut für Festkörpertheorie und Optik, Friedrich-Schiller-Universität Jena, Fröbelstieg 1, 07743 Jena
†Institut für Anorganische Chemie, Universität Leipzig, Johannisallee 29, 04103 Leipzig

The demand for transparent materials for optoelectronic applications has increased significantly in recent years[1]. In particular, copper halides and especially copper

iodide (CuI) have recently become the focus of research as wide bandgap p-type semiconductors [2–4]. Although the application potential of CuI has recently been demonstrated in e.g. transparent p-n heterojunctions and thin-film transistors, the excessive hole densities are detrimental to active device applications[2]. However, substitution of iodine with bromine is expected to enable tunable carrier density in thin films of $CuBr_xI_{1-x}$ alloys [6]. Since the optical response of the alloy system has not been studied in detail so far, we have investigated the dielectric function of the $CuBr_xI_{1-x}$ alloy and the origin of the underlying electronic transitions by combining experimental and computational methods.

Fig. 2.22(a) shows the dielectric function of the $CuBr_xI_{1-x}$ alloy for $0 \leq x \leq 1$. As mentioned previously the thin films are almost fully transparent in the visible spectral range. The lowest energy transition labeled with E_0 was attributed to excitonic transitions at the fundamental bandgap at the Γ-point. The next transition $E_0 + \Delta_0$ was assigned also to transitions at the Γ-point but involving the split-off valence band. The high energy transitions between 4.5 eV and 6.5 eV are labeled with E_1 and E_0' in accordance to previous publications [4, 5]. Although, the E_0' resonance in CuI and CuBr was assigned in the past to transitions at the Γ-point between the split-off components of the top VB and second conduction band [5], we could show based on the DFT bandstructure calculations that the corresponding transitions occur also in the vicinity of the L-point similar to the E_1 transition.

We note that the E_0 transition does not exhibit monotonic behavior as a function of the alloy composition. The corresponding nonlinear contribution to the energy shift can be described by the quadratic term $bx(1-x)$ where b represents the bowing parameter (see Fig.2.22 (b)). At room temperature, the estimated bowing parameter is determined to be 0.49 eV, which is in reasonable agreement with our DFT calculations for an ordered $CuBr_xI_{1-x}$ alloy yielding a value of b=0.58 eV. We note that the observed discrepancies between the experimental and calculated values are due to the impact of the temperature on the band gap energy, which in turn leads to an increase of the bowing with decreasing temperature.

In order to investigate the effect of the p-d-hybridization of the valence band maximum (VBM) in detail the spin-orbit splitting was determined as a function of the alloy composition. Fig.2.22 (c) shows the almost linear decrease of the spin-orbit splitting Δ_0 with increasing Br-content, which can be explained by a lower one-electron spin-orbit splitting of the bromine in comparison to iodine[5]. However, the absolute values of Δ_0 are significantly lower as expected due to strong p-d-hybridization of the VBM. We show that the contribution of the copper d-orbitals decreases from $\alpha \approx 0.52$ to $\alpha \approx 0.36$ with increasing Br-content, which is in excellent agreement with our DFT calculations.

[1] M. Morales-Masis, et al.: Adv. Electron Mater. **3** (2017).
[2] P. Storm, et al.: APL Materials **8**, 1600529 (2020). doi:10.1002/aelm.201600529
[3] A. Liu, et al.: Adv. Sci. **8**, 2100546 (2021). doi:10.1002/advs.202100546
[4] E. Krüger et al.: Appl. Phys. Lett **113**, 172102 (2018). doi:10.1063/1.5051963
[5] M. Cardona: Phys. Rev. **129**, 69 (1963). doi:10.1103/PhysRev.129.69
[6] N. Yamada, et al.: Adv. Funct. Mater. **30**, 2003096 (2020).

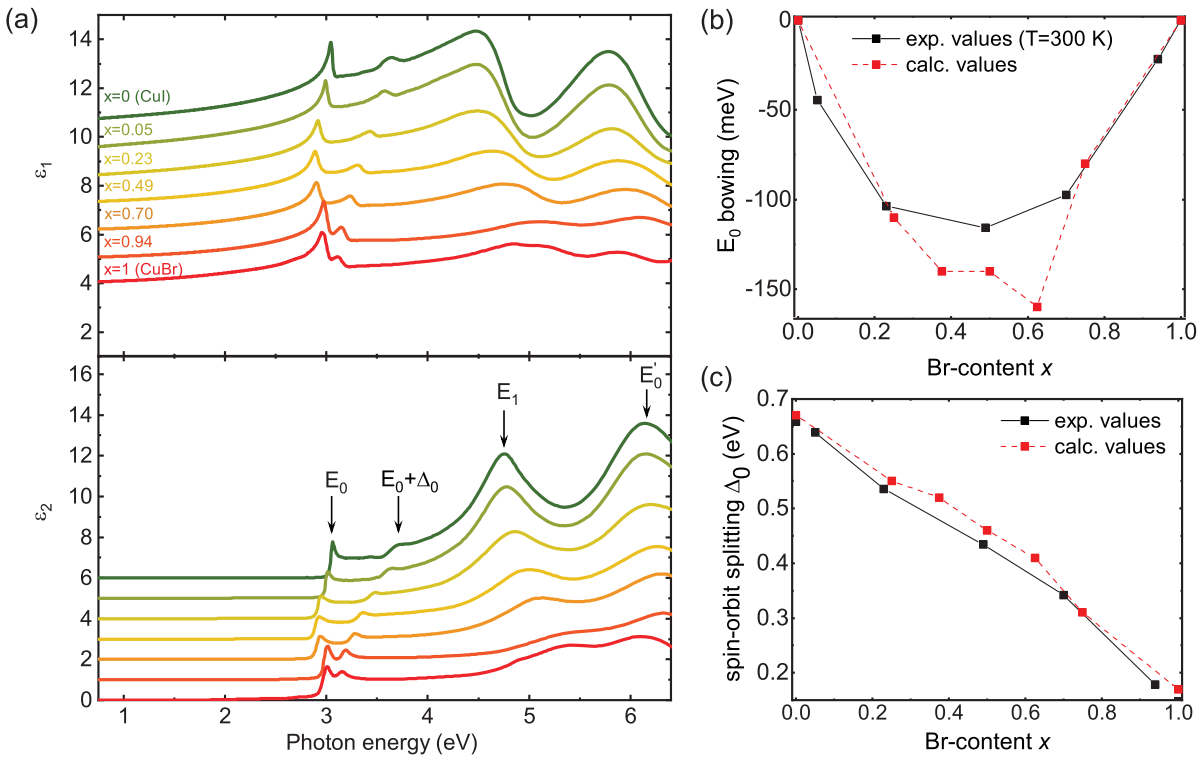

Figure 2.22: (a) Spectra of the real (ε_1) and imaginary (ε_2) part of the dielectric function of $CuBr_xI_{1-x}$ alloy thin films depending on the alloy composition. The observed resonances labeled with E_0, $E_0 + \Delta_0$, E_1 and E_0' are highlighted by vertical arrows. For better clarity, the spectra are shifted vertically against each other. (b) Quadratic bowing contribution of the E_0 energy shift as a function of the alloy composition. The black symbols represent the experimentally obtained transition peak energies, while the red symbols represent the calculated values for ordered $CuBr_xI_{1-x}$ alloy. (c) Spin-orbit splitting at the Γ-point Δ_0 in dependence on the Br-content. The black and red symbols again represent the experimental and calculated values, respectively.

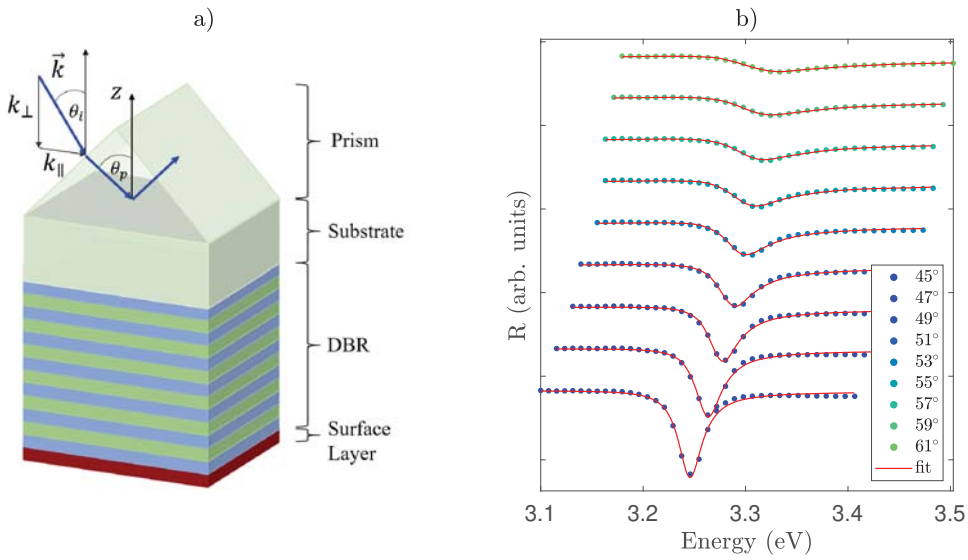

Figure 2.23: Kretschmann configuration and prims excitation of BSWP in a) and reflectivity spectra with red lines corresponding to the fit of a Fano-type resonance.

2.14 Bloch surface wave polaritons at temperatures up to 430 K

S. Henn, C. Sturm, M. Grundmann

Light traveling inside a material comprises a mixture of an electromagnetic wave as well as a polarization wave, that can exchange quantised energy ($\hbar\omega$) with other systems, e.g. the vacuum radiation field and these energy quanta are called polaritons [1]. Prominent examples of these are exciton-polaritons, where the photon interacts with the elctron-hole pairs of a semiconductor, e.g. inside a microcavity [2], displaying a wide variety of interesting physical phenomena, like low-theshold lasing and Bose-Einstein condensation [3]. Another platform for the formation of exciton-polaritons is a distributed Bragg reflector (DBR) with a truncated surface layer. This surface layer supports an evanescent wave propagating along the interface, the so-called Bloch surface wave (BSW) [4]. Its dispersion can be modeled by a simple (2×2) transfer matrices and lies in the stop band of the DBR. While this surface wave is lossless, a rough surface or interface leads to scattering processes, rendering its propagation length finite [5], which can, however, reach up to 100 µm.

By depositing a semiconducting ZnO surface layer on the reflector, these modes can be coupled to excitons, forming a Bloch surface wave polariton (BSWP). This holds several advantages compared to exciton-polaritons in conventional planar microcavities: a reduced complexitiy of production (small number of layers) and direct access to the mode-supporting layer for the deposition of further structures, e.g. interferometers, gratings, which is useful for application purposes. Additionally, the Bloch-polariton has no ground state, i.e. $k \neq 0$ and inherits the low-loss-natur of BSW, promising large propagation lengths.

The coupling between an exciton and a photon splits the two individual dispersions into an upper and lower polariton branch (UPB, LPB) in the vicinity of the crossing point, called the strong-coupling regime. In structures with a ZnO surface layer it was

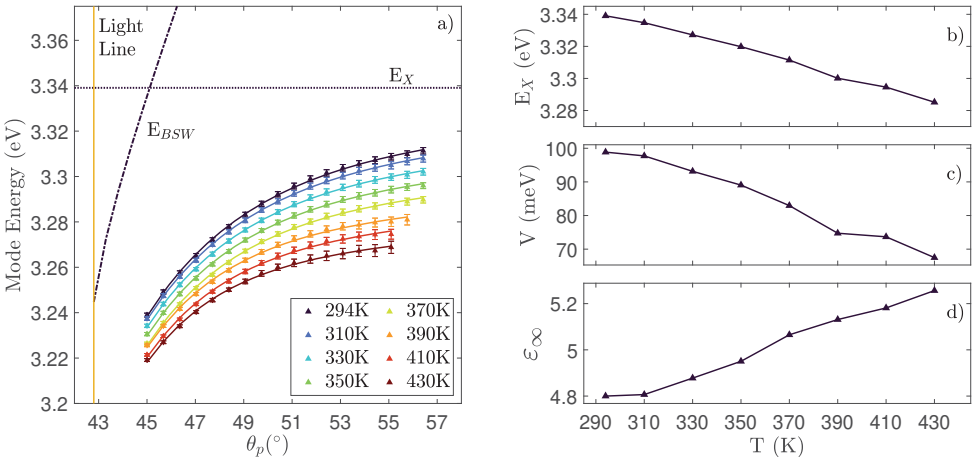

Figure 2.24: Temperature dependent BSWP dispersion in a) with the exciton energy (dotted), bare BSW dispersion (dashed-dotted) and light line (vertical line). The temperature evolution of the fit parameters, i.e. E_X, V, ε_∞, is given in b).

possible to observe BSWP for temperatures of up to 430 K [6]. However, the absorption for energies above the band gap renders the UPB non-observable [7]. The experimental values were obtained from measuring the TE-polarized reflectivity in a Kretschmann configuration [5] and mode energies were extracted from modelling Fano-type resonances [8], which can be seen in figure 2.23. The temperature evolution of the mode dispersion as well as the fit parameters, i.e. the coupling strength V, the flat exciton energy E_X and the dielectric background of the bare BSW mode ε_∞, is given in figure 2.24. These findings are in agreement with the temperature evolution of the exciton energy and broadening, which is redshifted and broadened for increasing temperatures, respectively. The coupling strength ranges decreases from 100 meV to 70 meV for temperatures between 290 – 430 K. This coupling strength exceeds the broadening of the mode and therefore confirms the strong-coupling regime. The stable formation of BSWP at such high temperatures can be exploited for on-chip polariton devices operating above room temperature.

[1] C. Klingshirn: Semiconductor Optics 4th Ed. (Springer-Verlag, Berlin Heidelberg, 2012) doi:10.1007/978-3-642-28362-8
[2] R. Schmidt-Grund *et al.*, Appl. Phys. B **93**, 331-337 (2008). doi:10.1007/s00340-008-3160-x
[3] J. Klaers *et al.*, Nature **468**, 545-548 (2010) doi:10.1038/nature09567
[4] P. Yeh *et al.*, Appl. Phys. Lett. **32**, 104 (1978); doi:10.1063/1.89953
[5] H. Raether: Surface Plasmons on Smooth and Rough Surfaces and on Gratings 1st Ed. (Springer-Verlag Berlin Heidelberg, 1988) doi:10.1007/BFb0048317
[6] S. Henn *et al.*, New J. Phys. **23**09031 (2021) doi:10.1088/1367-2630/ac2452
[7] C. Sturm *et al.*, New J. Phys. **11** 073044 (2009) doi:10.1088/1367-2630/11/7/073044
[8] I. Soboleva *et al.*, Phys. Rev. Lett. **108**, 123901 (2012) doi:10.1103/PhysRevLett.108.123901

2.15 Singular optic axes in bulk materials

M. Grundmann, C. Sturm

In 1902, Voigt pointed out, that in orthorhombic crystals each of the two optic axis splits into two singular optic axes as soon as the absorption sets in. [1] In contrast to an optic axis, along a singular optic axis either a left-handed or right-handed circular polarized wave can propagate without changing its properties. The presence of singular optic axes are not limited to orthorhombic crystal only and appear in general for crystals having an orthorhombic crystal symmetry or lower. [2, 3]

The wave eqution for homogeneous waves in crystals without optical activity is given by $\mathbf{M}E = 0$ with

$$\boldsymbol{M} = \boldsymbol{R}^{-1}\,\boldsymbol{\epsilon}\,\boldsymbol{R} - n^2 \,.\begin{pmatrix} 1 & 0 & 0 \\ 0 & 1 & 0 \\ 0 & 0 & 0 \end{pmatrix}, \tag{2.6}$$

Here, n represents the complex-valued refractive index, $\boldsymbol{\epsilon}$ the tensor of the dielectric function and $\boldsymbol{R} = \boldsymbol{R}_z(\phi)\boldsymbol{R}_y(\theta)$ the rotation matrix, which transfer the dielectric tensor defined in the framework of the crystal into the system in which the wave propagates along the z' direction. R_i is the rotation matrix around the i-th axis. The eigenvalues, i.e., the complex-valued refractive index, can be then found by $\det \boldsymbol{M} = 0$. In the case of the singular optic axes, both eigenvalues are degenerated. If we assume a symmetric dielectric tensor, the solution for a degeneration of the complex-valued refractive index can be written by [4]

$$\left(\sum_{j=0}^{j=4} g'_j\,\kappa^j\,x^j\right)\left(\sum_{j=0}^{j=4} g'_j\,\kappa^{-j}\,x^j\right) = 0 \tag{2.7}$$

with $\kappa = 1/(i\tan\theta/2)$ and $x = \exp i\phi$. The coefficients g_i are given by

$$g_0 = -(\epsilon_{xz} + i\epsilon_{yz})^2 + (\epsilon_{xx} + 2i\epsilon_{xy} - \epsilon_{yy})\epsilon_{zz} \tag{2.8a}$$
$$g_1 = 4(i\epsilon_{yy}\epsilon_{xz} - \epsilon_{xx}\epsilon_{yz} + \epsilon_{xy}(\epsilon_{xz} - i\epsilon_{yz})) \tag{2.8b}$$
$$g_2 = 2(\epsilon_{xz}^2 + \epsilon_{yz}^2 - 2\epsilon_{xy}^2 + 2\epsilon_{xx}\epsilon_{yy} - (\epsilon_{xx} + \epsilon_{yy})\epsilon_{zz}) \tag{2.8c}$$
$$g_3 = -4(-i\epsilon_{yy}\epsilon_{xz} - \epsilon_{xx}\epsilon_{yz} + \epsilon_{xy}(\epsilon_{xz} + i\epsilon_{yz})) \tag{2.8d}$$
$$g_4 = -(\epsilon_{xz} - i\epsilon_{yz})^2 + (\epsilon_{xx} - 2i\epsilon_{xy} - \epsilon_{yy})\epsilon_{zz}\,. \tag{2.8e}$$

Interestingly, the roots of the first and second brackets of Eq. 2.7 represents the solution for a left-handed or rather right-handed circular polarized wave and thus proves that the eigenmodes of the singular optic axis cannot be elliptical polarized. Furthermore, each bracket in Eq. 2.7 represents a quartic polynomial and so eight directions in total exists, where the complex-valued refractive index is degenerated. However, if (ϕ, θ) is a solution of the first bracket in Eq. 2.7, then $(\pi + \phi, \pi - \theta)$ is a solution of the second bracket. Thus, two opposite directions with opposite polarization forming an singular optic axis. Therefore, four singular optic axes can exist in maximum.

[1] W. Voigt: Ann. Phys. **314**, 367 (1902).

[2] M.V. Berry and M.R. Dennis: Proc. R. Soc. London A **459**, 1261 (2003) doi:10.1098/rspa.2003.1155.
[3] C. Sturm and M. Grundmann: Phys. Rev. A **93**, 053839 (2016) doi:10.1103/PhysRevA.93.053839.
[4] M. Grundmann and C. Sturm: Phys. Rev. A **103**, 053510 (2021) doi:10.1103/PhysRevA.103.053510.

3

Funding, Organizational Duties, External Cooperations

3.1 Funding

Flexible analoge und digitale Grundschaltungen in amorphen Metalloxiden
Prof. Dr. M. Grundmann
DFG GR 1011/31-2, within SPP *High Frequency Flexible Bendable Electronics for Wireless Communication Systems (FFLexCom)*

Raman-Streuung in anisotropen Kristallen
Prof. Dr. M. Grundmann
DFG GR 1011/33-1

Wurtzitische Zink-basierte Oxynitride als vielversprechende photovoltaische Absorber: Epitaxie, Bandstruktur-Anpassung und Heterostrukturen
Dr. C. Yang
DFG YA 511/1-1

Zink-Magnesium Oxinitride
Prof. Dr. M. Grundmann
GR 1011/36-1 (DFG – ANR, cooperative project)

Bauelemente mit vertikalem Kompositionsgradient
Prof. Dr. M. Grundmann
DFG GR 1011/42-1

Zwischenband-Solarzellen auf Basis Übergangsmetall-substitutierter Indium-thiospinelle
PD Dr. H. von Wenckstern
DFG WE 4620/3-1

Remanentes Schalten von Bloch-Polaritonen
Dr. C. Sturm
DFG STU 647/2-1

Koordinationsfonds
Prof. Dr. M. Grundmann
DFG GR 1011/41-1 within FOR 2857 *Kuperiodid als multifunktionaler Halbleiter*

Mikrostruktur-basierte Optimierung des Wachstums dünner CuI-Filme
Prof. Dr. M. Lorenz
DFG LO 790/7-1, P01 within FOR 2857 *Kupferiodid als multifunktionaler Halbleiter*

Amorphe Kupferiodid-Dünnfilme und Kupferiodid-basierte Legierungshalbleiter
Prof. Dr. M. Grundmann
DFG GR 1011/40-1, P03 within FOR 2857 *Kupferiodid als multifunktionaler Halbleiter*

Amorphe Kupferiodid-Dünnfilme und Kupferiodid-basierte Legierungshalbleiter
Dr. C. Yang
DFG YA 511/2-1, P03 within FOR 2857 *Kupferiodid als multifunktionaler Halbleiter*

Elektrische Eigenschaften von CuI Dünnfilmen und Volumenkristallen und Herstellung von CuI-basierten Bauelementen
PD Dr. H. von Wenckstern
DFG WE 4620/5-1, P05 within FOR 2857 *Kupferiodid als multifunktionaler Halbleiter*

Optische Eigenschaften von Kupferiodid, dotierten Kupferiodid und Kupferiodid-basierten Legierungshalbleitern
Dr. C. Sturm
DFG STU 647/3-1, P06 within FOR 2857 *Kupferiodid als multifunktionaler Halbleiter*

Ultrakompaktes Spektrometer – UltraSPEC2
Prof. Dr. M. Grundmann
VIP+, BMBF 03VP08180

Growth and fundamentals of oxides for electronic applications – GraFOx II
Prof. Dr. M. Grundmann, PD Dr. H. von Wenckstern
Leibniz Gemeinschaft W40/2019

3.2 Organizational Duties

M. Grundmann

- Vice Dean of the Faculty of Physics and Earth Sciences
- Director of the Felix Bloch Institute for Solid State Physics
- Sprecher der Graduiertenschule ”Leipzig School of Natural Sciences - Building with Molecules and Nano-objects” (BuildMoNa), http://www.buildmona.de/
- Sprecher der Forschungsgruppe FOR 2857 "Copper Iodide as Multifunctional Semiconductor", https://research.uni-leipzig.de/for2857/
- Sprecher der Fächerübergreifenden Arbeitsgemeinschaft Halbleiterforschung Leipzig (FAHL), https://home.uni-leipzig.de/fahl/
- Sprecher des Freundeskreis der Fakultät für Physik und Geowissenschaften
- Member Editorial Board: Physica Status Solidi (a), (b), RRL, MDPI nanomaterials, Phys. Rev. Research
- Member International Advisory Board: Advanced Electronic Materials
- Project Reviewer: diverse

- Referee: Applied Physics Letters, Electronics Letters, Journal of Applied Physics, Nature, Physica E, Physical Review B, Physical Review Letters, Physica Status Solidi, Advanced Materials, u.a.

M. Kneiß

- Referee: Applied Physics Express, Applied Physics Letters, ACS Applied Electronic Materials, CrystEngComm, Journal of Electronic Materials, Journal of Materials Research, Physica Status Solidi A

M. Lorenz

- Member Editorial Board: Journal of Physics D: Applied Physics (IOP, Bristol, U.K.), Journal Materials (MDPI, Basel, Switzerland)
- Project Reviewer: Deutsche Forschungsgemeinschaft, Alexander von Humboldt - Stiftung
- Referee: ACS Applied Nano Materials, Advanced Materials, Advanced Electronic Materials, Applied Physics Letters (APL), coatings (MDPI), Dalton Transactions, fibers (MDPI), Journal of Crystal Growth, Journal of Physics D: Applied Physics, Journal of Alloys and Compounds (JALCOM), Journal of Applied Physics (JAP), Journal of Magnetism and Magnetic Materials (JMMM), materials (MDPI), nanomaterials (MDPI), small (Wiley VCH), Thin Solid Films

D. Splith

- Referee: Applied Physics Express, Physica Status Solidi A, IEEE Transactions on Electron Devices

C. Sturm

- Referee: ACS Nano, Appl. phys. Lett., Applied Optics, Alexander von Humboldt Stiftung, Journal of applied Physics, J. Phys. Chem. Lett., Phys. Rev. B, Phys. Status Solidi RRL, Sci. Rep.

H. von Wenckstern

- Project Reviewer: Deutsche Forschungsgemeinschaft, National Science Centre Poland
- Associate Editor: Journal of Electronic Materials
- Referee: ACS Materials and Interfaces, Advanced Functional Materials, Annalen der Physik, Applied Physical Letters, APL Materials, Electronic Device Letters, Journal of Applied Physics, Material Science in Semiconductor Processing, Physica Status Solidi, Scientific Reports, Solid State Electronics, Superlattices and Microstructures, Thin Solid Films, u.a.

3.3 External Cooperations

Academic

- Leibniz-Institut für Oberflächenmodifizierung e. V., Leipzig, Germany
  Prof. Dr. A. Anders, Prof. Dr. S. Mayr, Dr. C. Bundesmann, Dr. A. Lotnyk

- Universität Leipzig, Fakultät für Chemie und Mineralogie, Germany
  Prof. Dr. H. Krautscheid, Prof. Dr. R. Denecke, Prof. Dr. O. Oeckler, Dr. V. Gottschalch, Dr. S. Blaurock
- Universität Halle-Wittenberg, Germany
  Prof. Dr. I. Mertig, Prof. Dr. R. Scheer
- Fraunhofer-Institut für Mikrostruktur von Werkstoffen und Systemen IMWS, Halle (Saale), Germany
  Prof. Dr. T. Höche, Dr. C. Patzig, Dr. S. Selle
- Forschungszentrum Dresden-Rossendorf, Germany
  Dr. S. Zhou
- Humboldt-Universität zu Berlin, Germany
  Prof. Dr. N. Koch
- Leibniz-Institut für Festkörperelektronik – Paul Drude (PDI), Berlin, Germany
  Dr. O. Bierwagen
- Universität Magdeburg, Germany
  Porf. Dr. A. Dadgar, Dr. J. Bläsing
- Universität Jena, Germany
  Prof. Dr. C. Ronning, Prof. Dr. S. Botti
- Technische Universität Ilmenau, Germany
  Prof. Dr. S. Krischok, Dr. R. Schmidt-Grund
- Johannes Gutenberg-Universität Mainz, Department Chemie, Germany
  Prof. Dr. S.R. Waldvogel
- Hochschule Mittweida, Laserinstitut, Germany
  Prof. Dr. A. Horn, T. Pflug, M. Olbrich
- University of Canterbury, Christchurch, New Zealand
  Prof. Dr. M. Allen
- Centre de Recherche sur l'Hétéro-Epitaxie et ses Applications (CNRS-CRHEA), Valbonne, France
  Dr. J. Zúñiga-Pérez, Dr. Guy Feuillet
- Western Michigan University, USA
  Prof. Dr. S. M. Durbin
- The Ohio State University, USA
  Prof. Dr. L. Brillson
- Arizona State University, USA
  Prof. F. Ren
- University of Florida, USA
  Prof. S. Pearton
- Katholieke Universiteit Leuven, Belgium
  Dr. V. Lazenka, Prof. Dr. K. Temst
- University of Oslo, Norway
  Prof. Dr. L. Vines

- ELI Beamlines - International Laser Research Centre, Dolní Brežany, Czech Republic
  Prof. J. Andreasson, Dr. S. Richter, Dr. S. Espinoza, Dr. M. Rebarz

Industry

- Freiberger Compound Materials GmbH, Freiberg, Germany
  Dr. G. Leibiger
- First Sensor AG, Berlin, Germany
  Dr. M. Schillgalies
- Optics Balzers Jena GmbH, Jena, Germany
  Dr. A. Rahm
- SaxonQ GmbH, Leipzig, Germany

4

Publications

Journals

J. Borgersen, K.M. Johansen, L. Vines, H. von Wenckstern, M. Grundmann, A.Yu. Kuznetsov: *Fermi level controlled point defect balance in ion irradiated indium oxide*, J. Appl. Phys. **130**(8), 085703:1-6 (2021)
doi:10.1063/5.0062135

V. Gottschalch, G. Benndorf, S. Selle, E. Krüger, S. Blaurock, M. Kneiß, M. Bar, C. Sturm, S. Merker, T. Höche, M. Grundmann, H. Krautscheid: *Epitaxial growth of rhombohedral β- and cubic γ-CuI*, J. Cryst. Growth **570**, 126218 (2021)
doi:10.1016/j.jcrysgro.2021.126218

M. Grundmann, T. Stralka, M. Lorenz, S. Selle, C. Patzig, T. Höche: *Plastic strain relaxation and alloy instability in epitaxial corundum-phase $(Al,Ga)_2O_3$ thin films on r-plane Al_2O-3*, Mater. Adv. **2**(13), 4316-4322 (2021)
doi:10.1039/D1MA00204J

M. Grundmann, C. Sturm: *Angular position of singular optic axes for arbitrary dielectric tensors*, Phys. Rev. A **103**(5), 053510:1-6 (2021)
doi:10.1103/PhysRevA.103.053510

M. Grundmann, M. Lorenz: *Azimuthal anisotropy of rhombohedral (corundum-phase) heterostructures*, Phys. Status Solidi B **258**(7), 202100104:1-5 (2021)
doi:10.1002/pssb.202100104

A. Hassa, M. Grundmann, H. von Wenckstern: *Progression of Group-III Sesquioxides: Epitaxy, Solubility and Desorption*, J. Phys. D: Appl. Phys. **54**(22), 223001:1-15 (2021)
doi:10.1088/1361-6463/abd4a4

A. Hassa, P. Storm, M. Kneiß, D. Splith, H. von Wenckstern, M. Lorenz, M. Grundmann: *Correction to: Structural and elastic properties of a-$(Al_xGa_{1-x})_2O_3$ thin films on (11.0) Al_2O_3 substrates for the entire composition range*, Phys. Status Solidi B **258**(2), 2000632 (1 page) (2021)
doi:10.1002/pssb.202000632

A. Hassa, P. Storm, M. Kneiß, D. Splith, H. von Wenckstern, M. Lorenz, M. Grundmann: *Structural and elastic properties of a-$(Al_xGa_{1-x})_2O_3$ thin films on (11.0) Al_2O_3 substrates for*

the entire composition range, Phys. Status Solidi B **258**(2), 2000394:1-10 (2021)
doi:10.1002/pssb.202000394

S. Henn, M. Grundmann, C. Sturm: *Strong coupling of Bloch surface waves and excitons in ZnO up to 430 K*, New J. Phys. **23**, 093031:1-10 (2021)
doi:10.1088/1367-2630/ac2452

O. Herrfurth, E. Krüger, S. Blaurock, H. Krautscheid, M. Grundmann: *Hot-phonon effects in photo-excited wide-bandgap semiconductors*, J. Phys.: Condens. Matter 33(20), 205701:1-9 (2021)
doi:10.1088/1361-648X/abf19b

O. Herrfurth, S. Richter, M. Rebarz, S. Espinoza, J. Zúñiga-Pérez, C. Deparis, J. Leveillee, A. Schleife, M. Grundmann, J. Andreasson, R. Schmidt-Grund: *Transient birefringence and dichroism in ZnO studied with fs-time-resolved spectroscopic ellipsometry*, Phys. Rev. Res. **3**(1), 013246:1-12 (2021)
doi:10.1103/PhysRevResearch.3.013246

R. Hildebrandt, C. Sturm, M. Grundmann, M. Wieneke, A. Dadgar: *Raman tensor determination of transparent uniaxial crystals and their thin ?lms - a-plane GaN as exemplary case*, Appl. Phys. Lett. **119**(12), 121109:1-5 (2021)
doi:10.1063/5.0060198

P. John, M. Al Khalfioui, C. Deparis, A. Welk, C. Lichtensteiger, R. Bachelet, G. Saint-Girons, M. Hugues, M. Grundmann, J. Zúñiga-Pérez: *Epitaxial Zn_3N_2 thin films by molecular beam epitaxy: Structural, electrical and optical properties*, J. Appl. Phys. **130**(6), 065104:1-11 (2021)
doi:10.1063/5.0057307

M. Kneiß, D. Splith, P. Schlupp, A. Hassa, H. von Wenckstern, M. Lorenz, M. Grundmann: *Realization of Highly Rectifying Schottky Barrier Diodes and pn Heterojunctions on κ-Ga_2O_3 by Overcoming the Conductivity Anisotropy*, J. Appl. Phys. **130**(8), 084502:1-14 (2021)
doi:10.1063/5.0056630

M. Kneiß, D. Splith, H. von Wenckstern, M. Lorenz, T. Schultz, N. Koch, M. Grundmann: *Strain States and Relaxation for α-$(Al_xGa_{1-x})-2O-3$ Thin Films on Prismatic Planes of α-$Al-2O-3$ in the Full Composition Range: Fundamental Difference of a- and m-Epitaxial Planes in the Manifestation of Shear Strain and Lattice Tilt*, J. Mat. Res. **36**(23), 4816-4831 (2021)
doi:10.1557/s43578-021-00375-3

M. Kneiß, P. Storm, A. Hassa, D. Splith, H. von Wenckstern, M. Lorenz, M. Grundmann: *Epitaxial Growth of κ-$(Al-xGa_{1-x})_2O_3$ Layers and Superlattice Heterostructures up to x=0.48 on Highly Conductive Al-doped ZnO Thin Film Templates by Pulsed Laser Deposition*, Phys. Status Solidi B **258**(2), 202000359:1-10 (2021)
doi:10.1002/pssb.202000359

E. Krüger, M.S. Bar, S. Blaurock, L. Trefflich, R. Hildebrandt, A. Müller, O. Herrfurth, G. Benndorf, H. von Wenckstern, H. Krautscheid, M. Grundmann, C. Sturm: *Dynamics of exciton-polariton emission in CuI*, APL Mater. **9**(12), 121102:1-12 (2021)
doi:10.1063/5.0066176

O. Lahr, M. Steudel, H. von Wenckstern, M. Grundmann: *Mechanical Stress Stability of Amorphous Zinc Tin Oxide Thin-Film Transistors*, Front. Electron. **2**, 797308:1-7 (2021)
doi:10.3389/felec.2021.797308

A. Reinhardt, H. von Wenckstern, M. Grundmann: *All-amorphous Junction Field-Effect Transistors Based on High-Mobility Zinc Oxynitride*, Adv. Electron. Mater. **7**(4), 2000883:1-6 (2021)
doi:10.1002/aelm.202000883

D. Splith, S. Müller, H. von Wenckstern, M. Grundmann: *Numerical modeling of Schottky barrier diode characteristics*, Phys. Status Solidi A **218**(12), 202100121:1-13 (2021)
doi:10.1002/pssa.202100121

P. Storm, S. Gierth, S. Selle, M.S. Bar, H. von Wenckstern, M. Grundmann, M. Lorenz: *Evidence for oxygen being a dominant shallow acceptor in p-type CuI*, APL Mater. **9**(5), 051101:1-9 (2021)
doi:10.1063/5.0047723

P. Storm, M.S. Bar, S. Selle, H. von Wenckstern, M. Grundmann, M. Lorenz: *P-Type Doping and Alloying of CuI Thin Films with Selenium*, Phys. Status Solidi RRL **15**(8), 202100214:1-6 (2021)
doi:10.1002/pssr.202100214

J.E.N. Swallow, R.G. Palgrave, P.A.E. Murgatroyd, A. Regoutz, M. Lorenz, A. Hassa, M. Grundmann, H. von Wenckstern, J.B. Varley, T.D. Veal: *Indium Gallium Oxide Alloys: Electronic Structure, Optical Gap, Surface Space Charge, and Chemical Trends within Common-Cation Semiconductors*, ACS Appl. Mater. Interfaces **13**(2), 2807-2819 (2021)
doi:10.1021/acsami.0c16021

A. Welk, A. Reinhardt, O. Herrfurth, T. Schultz, H. von Wenckstern, N. Koch, M. Grundmann: *Tuning material properties of amorphous zinc oxynitride thin films by magnesium cationic substitution*, APL Mater. **9**(2), 021120:1-8 (2021)
doi:10.1063/5.0035147

X. Xia, C. Fares, F. Ren, A. Hassa, H. von Wenckstern, M. Grundmann, S.J. Pearton: *Al Composition Dependence of Band Offsets for SiO_2 on α-$(Al_xGa_{1-x})_2O_3$*, ECS J. Solid State Sci. Techn. **10**(11), 113007:1-8 (2021)
doi:10.1149/2162-8777/ac39a8

W. Yu, G. Benndorf, Y. Jiang, K. Jiang, C. Yang, M. Lorenz, M. Grundmann: *Control of optical absorption and emission of sputtered copper iodide thin films*, Phys. Status Solidi RRL **15**(1), 2000431:1-5 (2021)
doi:10.1002/pssr.202000431

Publications without peer review

M. Grundmann: *Report Halbleiterphysik/Semiconductor Physics 2020*, Universität Leipzig (2021)

Books

M. Grundmann: *The Physics of Semiconductors, An Introduction including Nanophysics and Applications, 4th edition*, (Springer Nature, Cham, 2021), ISBN 978-3-030-51568-3 doi:10.1007/978-3-030-51569-0

Talks

M. Grundmann: *Halbleiter mit großer Bandlücke*, Berliner Physikalisches Kolloquium, Magnus-Haus, Berlin, Germany, July 2021 (invited)

E. Krüger, A. Müller, G. Benndorf, S. Blaurock, H. Krautscheid, M. Grundmann, C. Sturm: *Time-resolved luminescence of CuI microwires*, 13th Annual BuildMoNa Conference (online), Leipzig, Germany, March 2021

E. Krüger, M. Bar, S. Merker, M. Seifert, D. Splith, L. Trefflich, P. Bischoff, H. von Wenckstern, H. Krautscheid, S. Botti, M. Grundmann, C. Sturm: *Dielectric function of $CuBr_xI_{1-x}$ alloy thin films grown by pulsed laser deposition*, 11th Workshop Ellipsometry, Steyr, Austria, September 2021

O. Lahr, H. von Wenckstern, M. Grundmann: *Metal Oxide Based Field-effect Transistors: From Design Basics to Microelectronic Applications*, University of Helsinki Guest Lecture: Instrumentation of Particles, Helsinki, Finland, March 2021 (online)

O. Lahr, H. von Wenckstern, M. Grundmann: *A Sustainable Approach to Amorphous Oxide Semiconductor Based Electronics*, PhD Fortbildungsseminar, Leibniz-Institut für Kristallzüchtung (IKZ) Berlin, Leipzig, Germany, December 2021

R. Osskovski, O. Arteaga, and C. Sturm: textitHow to analyze optically active media, 11th Workshop Ellipsometry, Steyr, Austria, September 2021 (invited tutorial)

T. Stralka, C. Yang, H. von Wenckstern, M. Grundmann: *Dynamic AFM on CuI thin films*, Annual BuildMoNa Conference 2021, Leipzig, Germany, March 2021

T. Stralka, H. von Wenckstern, M. Grundmann: *Multistack AFM for localised current*, For2857 Annual Meeting and Status Seminar, Dresden, Germany, September 2021

C. Sturm, K. Hingerl, V. Zviagin, R. Schmidt-Grund, T. G. Mayerhöfer, M. Grundmann: *Optical properties of low symmetry materials and their determination by spectroscopic ellipsometry*, E-MRS (online), Strasbourg, France, June 2021 (invited)

L. Trefflich, C. Sturm, M. Grundmann: *Optimization of the optical properties of thin film superlattices by combining ellipsometry with statistical methods*, 11th Workshop Ellipsometry, Steyr, Austria, September 2021

Posters

K. Dorywalski, C. Sturm, M. Grundmann: *Combination of a global-search method with model selection criteria for the ellipsometric data evaluation of DLC coatings*, 11th Workshop Ellipsometry, Steyr, Austria, September 2021

S. Henn, M. Grundmann, C. Sturm: *Strong coupling of Bloch Surface Waves to excitons in ZnO*, 13th Annual BuildMoNa Conference (online), Leipzig, Germany, March 2021

S. Henn, M. Grundmann, C. Sturm: *Strong coupling of Bloch Surface Waves and excitons in ZnO up to* 430 K, DPG-Tagung der Sektion Kondensierte Materie (SKM) (online), Bad Honnef, Germany, October 2021

T. Stralka, F. Schöppach, M. Bar, H. von Wenckstern, M. Grundmann: *Multistack AFM on CuI thin films*, DPG Konference, September 2021 (online)

C. Sturm, L. Trefflich, M. Grundmann: *Uncertainty and correlation estimation by means of global-search algorithm*, 11th Workshop Ellipsometry, Steyr, Austria, September 2021

5

Graduations

Doctorate

- Stefan Hohenberger
  Magnetoelectric Coupling in $BaTiO_3$-$BiFeO_3$ Multilayers: Growth Optimization and Characterization
  January 2021
- Anna Hassa
  Epitaxy and Physical Properties of Group-III Sesquioxide Alloys
  June 2021
- Lukas Trefflich
  Carbon nanodots as active medium for planar microcavities
  September 2021

Master

- Cai Zichao
  Bloch surface wave polaritons in ZnO-based 1D periodic multilayer structures
  June 2021
- Max Steudel
  Charakterisierung flexibeler Halbleiterbauelemente basierend auf Zink-Zinn-Oxid
  September 2021
- Jasper Petschat
  Simulation of the Influence of Cosmic Radiation at Mean Sea Level on the Electrical Behavior of "Fully-Depleted Silicon-on-Insulator" MOSFETs
  October 2021

Bachelor

- Wen Wu Lee
  Cul-based thin films prepared by developed iodization method
  January 2021
- Ruey Jinq Ong
  Optimization of In_2O_3-based Field Effect Transistor devices
  September 2021

- Jorrit Bredow
  Influence of sputter parameters on amorphization and electrical conductivity in reactive magnetron sputtered Cu-Sn-I alloy thin films
  November 2021

6

Guests

- Fangjuan Geng
  University of Jinan, Jinan, PR China
  China Scholarship Council: Agreement for Study Abroad for CSC Sponsored Chinese Citizens
  September 2019 – August 2021
- Jingjing Yu
  Ningbo Institute of Materials Technology & Engineering (NIMTE), Ningbo, PR China
  China Scholarship Council
  August 2020 – August 2023

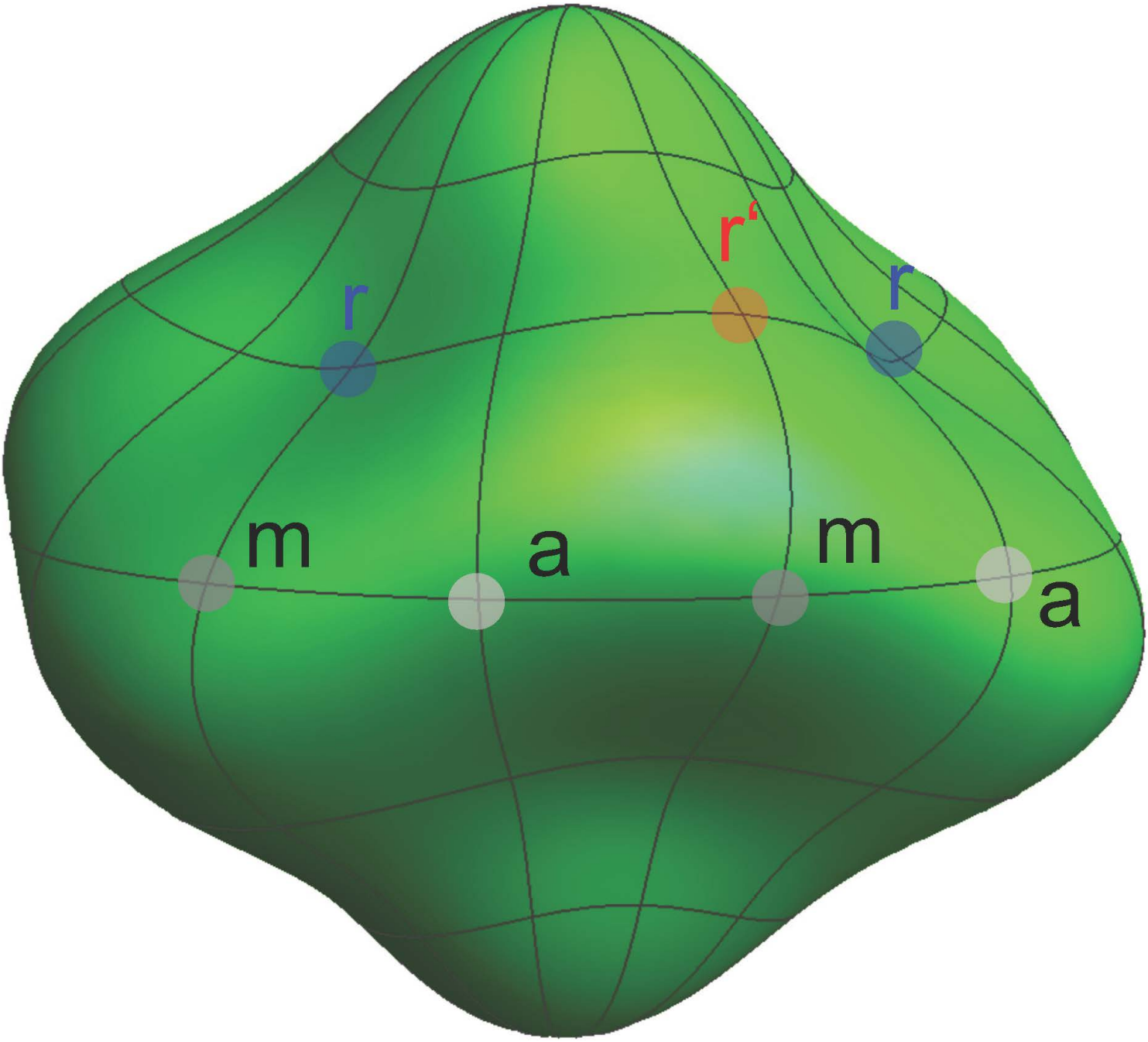
r
r'
r
m
a
m
a